University of Alberta

Design and Testing of a Prototype Thermophotovoltaic System

by

Christopher Jason Astle ©

A thesis submitted to the Faculty of Graduate Studies and Research in partial fulfillment of the requirements for the degree of Master of Science

Department of Mechanical Engineering

Edmonton, Alberta

Spring 2004

Your file Votre référence
ISBN: 0-612-96446-9
Our file Notre référence
ISBN: 0-612-96446-9

"So much to say,
say what you mean,
mean what you think,
think anything"

Cat Stevens

"The most exciting phrase to hear in science,
the one that heralds new discoveries,
is not 'Eureka!' (I found it), but 'That's funny ...' "

Isaac Asimov (1920 - 1992)

"I believe that a scientist looking at nonscientific problems
is just as dumb as the next guy."

Richard Feynman (1918 - 1988)

Abstract

The objective of this study is to increase knowledge of thermophotovoltaic power generation in a commercial-type application. Since thermophotovoltaic research has largely been concentrated on the advancement of individual components, with relatively little attention to integration of these components in a system, it is essential to gather system data if commercial applications of this technology are to be realized.

An experimental study measuring the performance of the major system components; the burner, emitter, spectral filtering elements, and the thermophotovoltaic cells, under differing energy input rates was performed. Short circuit current production was found to have a power-type dependence on emitter temperature, highlighting the requirement of increased emitter temperatures to enhance system efficiency. Power densities ranging from $0.07W/cm^2$ to $0.13W/cm^2$ were measured at burner firing rates from 6kW to 9kW. Overall fuel to electric conversion efficiency was found to increase linearly from 1.2% at 6kW to 1.5% at 9kW.

Acknowledgements

First and foremost I would like to thank my wife Lori for her unconditional love and support. Without you I would not be the man I am today.

I am also grateful for my son Daniel Gary, and the perspective I am granted by merely observing him.

I thank my parents Don and Eunice Astle, for gently nudging me in the right direction and always being there when I need them. I am a very lucky son.

My grandparents, Gary and Tillie Clapp also deserve thanks, for the support and comfort they have provided since I was a young farmyard scientist.

I am indebted to Dan, Margaret and Ian Villner, for the pleasant distraction and good company that has become Sunday dinner.

I am grateful for the help and friendship of Gary Kovacik of the Alberta Research Council, and the support he provided during the course of this study.

Advice, assistance and support were also obtained from Allan Chambers, Robert Bioletti, Ian Potter and Pieter van Nierop of the Alberta Research Council.

I thank my supervisor Dr. Ted Heidrick for his guidance and assistance over the course of this degree.

I also appreciate the time taken by my committee members; Dr. J.D. Dale, Dr. P.C. Flynn, and Dr. W. Xu, in examining this thesis and helping me bring to a close this chapter of my education.

Financial support for this thesis was provided by the Natural Sciences and Engineering Research Council of Canada (NSERC).

TABLE OF CONTENTS

Table of Figures

List of Symbols, Nomenclature, and Abbreviations

A_{cell}	= active area of one 72-cell GaSb circuit [cm^2]
As	= Arsenic
Blackbody	= An idealized radiator of electromagnetic radiation
C_p	= specific heat value [kJ/(kg K)]
Co	= Cobalt
CO	= Carbon Monoxide
DC	= direct current
E_g	= Bandgap Energy – energy gap between the valence band and the conduction band of the semi-conductor
Emitter	= component in a thermophotovoltaic system that emits electromagnetic radiation to be converted into electricity by the thermophotovoltaic cells
EV	= electron volt, unit of energy [eV]
$\dot{E}_{water\ out}$	= cooling water energy removal rate [kW]
FF	= Fill Factor - ratio of the maximum power of a cell to the product of the cell's open circuit voltage and short circuit current
Ga	= Gallium
Ge	= Germanium
I	= Amps [A]
i'_{grey}	= total intensity of a grey body
I_{max}	= current at maximum power point [A]
In	= Indium
IR	= infrared radiation
I_{sc}	= short circuit current [A]
$I_{sc\ LEG}$	= short circuit current of each leg of the parallel circuit [A]
$I_{sc\ MIN}$	= minimum individual short circuit current value of all the series connected cells [A]
IV Curve	= current versus voltage curve

LHV	= lower heating value [kJ/kmol]
$\dot{m}$	= mass flow rate [kg/s]
MgO	= Magnesium Oxide
n	= number of legs in the parallel circuit
ncell	= number of individual cells contained in the series circuit
Ni	= Nickel
NREL	= National Renewable Energy Laboratory
P_{cool}	= energy removal rate of optical enclosure cooling system [kW]
P_{fuel}	= fuel energy rate [kW]
Photovoltaic cell	= device that directly converts electromagnetic radiation to electricity
P_{max}	= maximum power point [W]
ppm	= parts per million
PV	= photovoltaic
QEext	= Quantum efficiency
$R_{resistor}$	= value of resistor wired across TPV cell [Ω]
Sb	= Antimony
Si	= Silicon
SiC	= Silicon Carbide
STP	= Standard temperature and pressure
T	= surface temperature [°C / K]
ΔT	= temperature difference [°C / K]
TPV	= Thermophotovoltaic
US	= United States of America
V	= volts [V]
V_{max}	= voltage at maximum power point [V]
V_{oc}	= open circuit voltage [V]
$V_{oc\,CELL}$	= open-circuit voltages of individual cells in the series circuit [V]
$V_{oc\,LEG}$	= open-circuit voltage of each leg of the parallel circuit [V]
$V_{resistor}$	= measured voltage across resistor [V]

ε = grey body emissivity

$\eta_{fuel-electric}$ = fuel to electric conversion efficiency [%]

$\lambda_{\max}$ = wavelength of maximum emissive power for a given temperature [μm]

ρ_{power} = power density [W/cm^2]

σ = Stefan-Boltzmann constant = 5.67x10^{-8} W/m^{2}K^4

1. INTRODUCTION

1.1 Dependence of Modern Society on Electricity

Society has become increasingly dependent upon electrical power, and with this increased dependence comes enhanced vulnerability to the disruption of its supply. Much of what we depend on in everyday life is powered by electricity. Microprocessors are used to control systems that vary in size from entire telephone networks to residential forced-air heating units, and consequences ranging from slight inconvenience to life-threatening situations are possible if these devices are denied power. With electrically powered devices being increasing integrated into the framework of industrialized societies, the stability and security of the supply of electricity is becoming more and more important.

1.2 Recent Electrical Power Failures

Recent events have highlighted the dependence of the North American population on electrical power. One such event is the Quebec Ice Storm of 1998, which at its peak, affected over 3 million people in Eastern Ontario and Southern Quebec and left approximately 65,000 people without power for nearly a month [1]. This power outage had a particularly large impact because it occurred in winter. Since Canadian winters are cold, and many forced-air heating units depend on electricity to operate, many homes affected by this outage were left cold and dark.

Another power outage occurred on August 14, 2003, the largest in North America's history, affecting over 50 million people in an area that spread from New York, New York, to Toronto, Ontario, in the north and Detroit, Michigan, in the west [2]. In this instance people were not left cold, but the exact opposite since air conditioning units were one of the many devices that ceased to function during the outage.

1.3 Distributed/Remote Power Generation

Distributed power generation removes the dependence on large, interconnected grids for power delivery and instead generates power close to where it is used. Increased use of this concept would reduce the massive impact caused when a major power plant goes off-line, as well as decrease line losses that exist in large power grids. Distributed/remote power generation is already used in geographically remote locations, to provide electrical power for applications including secluded cabins, military bases, and industrial stations.

The need for dependable, low maintenance, remote power generation is increasing. This is due, in part, to oil and gas companies having to move further and further into undeveloped areas in order to exploit natural resources. As well, large-scale pipelines are being increasingly introduced into the transmission systems of these industries, requiring power for tasks such as remote monitoring and corrosion protection. Many off-grid oil and gas sites currently use thermoelectric generators for this purpose. Thermophotovoltaic technology can aggressively compete with thermoelectric generators for this market segment, offering potential advantages including higher efficiency, smaller footprint and greater expandability. The oil and gas industry and its willingness to pay a premium for dependable, maintenance-free remote power is an ideal entry market.

Other technology utilized for remote power generation includes gasoline or diesel-fuelled engine generators, hydroelectric devices, turbine generators, and solar cells. Fuel cells are also emerging as a potential source of distributed/remote power generation, but their development and introduction into the commercial marketplace has been slower than expected.

1.4 Alternative Sources of Electrical Power Generation

Alternative energy development in areas such as solar, wind and tidal power hold promise, but have power potentials that depend on the surroundings. Possible remedies to this situation include employing large and expensive energy storage devices, over-sizing generation output, or both. A simpler solution would be to utilize a technology that has the ability to generate electricity at maximum capacity, in any situation.

1.5 Thermophotovoltaic Technology

Thermophotovoltaics produce electrical power in a method similar to solar cells (photovoltaic cells) but with subtle differences. The wavelengths used in thermophotovoltaic (TPV) power production are longer than those utilized by solar cells, and therefore can be produced by temperatures lower than those present on the sun. This enables photons produced by a combustion-heated emitter to be converted directly into electricity. The ability to control the emission source and, consequently, to produce power at any time of day and in any weather condition, is an advantage that TPV has over solar energy and most other alternative energy processes.

The fact that TPV cells can be placed in close proximity to the source of the photons, compared with the distance to the sun, increases the density of incident photons from $1kW/m^2$ in a traditional solar photovoltaic (PV) system up to $300kW/m^2$ in some TPV systems [3]. This difference in emissive power is highlighted by Fig. 1-1, which compares a blackbody heated to 1000°C and sunlight at the Earth's surface.

Higher emissive power levels from a locally heated blackbody result in higher power production densities than are possible with traditional solar photovoltaic systems. One estimate of maximum achievable output power density for TPV systems is $5W/cm^2$ [5] approximately 500 times that of a traditional flat plate PV system. Researchers in this field have already demonstrated power densities of $1.5W/cm^2$ [6]. Other attractions of

TPV systems include fuel versatility, compact size, silent operation, and low maintenance costs.

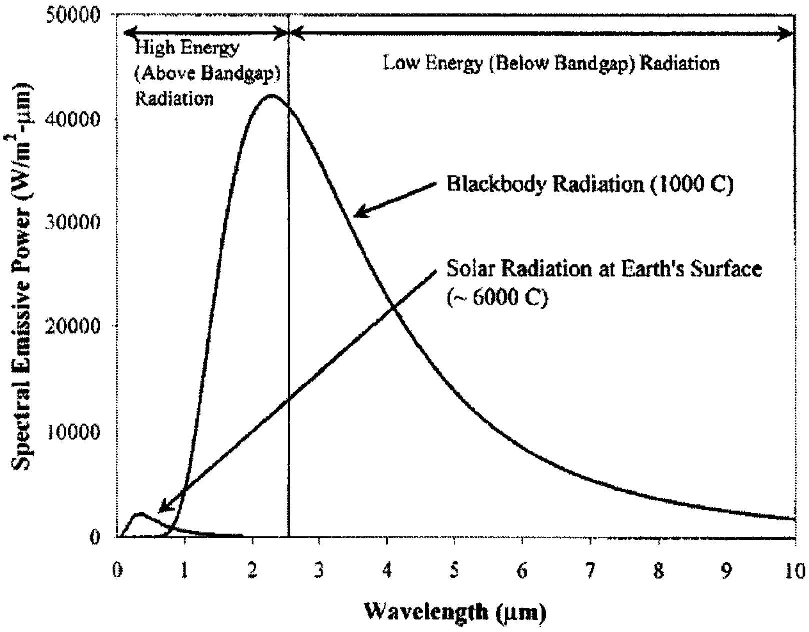

Figure 1-1: Comparison of Solar and Blackbody Radiation Intensity [4]

1.6 Potential Applications for Thermophotovoltaics

Potential applications for TPV technology include providing remote power for oil and gas well sites and secluded cabins, as well as military, aerospace, and sea-going functions. A TPV system could also be integrated into a residential heating system, in a combined heat and power (CHP) type application [7] [8]. This has the potential to take the furnace and possibly the entire residence "off-grid," with the TPV system generating enough power to satisfy the needs of the entire dwelling.

This concept of utilizing thermophotovoltaic cogeneration is not only applicable to residential installations, but large commercial installations as well. Industries already utilizing high temperature processes, such as large furnaces or kilns would be likely candidates for the incorporation of thermophotovoltaics. A TPV system installed into such a process would provide a constant source of electricity to offset some of the plant's power costs.

Thermophotovoltaic technology could also be applied to the transportation industry, as exhibited by the Viking 29 project at the Vehicle Research Institute at Western Washington University, [9] which resulted in the World's first thermophotovoltaic powered car. Thermophotovoltaics could also be adapted to provide power for recreational vehicles (RV's), which typically require a power supply if left stationary for long periods. Some RV owners have addressed this problem by installing solar systems to charge batteries, but TPV technology could supplant solar technology by offering sun-independent, high-density power.

Applications suggesting thermophotovoltaic technology integration ranging from systems powered by radioisotope for installation in small spacecraft [10], to systems powered by biomass, such as wood powder [11] attest to the wide range of possible applications for thermophotovoltaics.

1.7 Motivation and Objectives

1.7.1 Thesis Motivation

The development of commercial thermophotovoltaic systems would result in residential or commercial locations utilizing this technology decreasing or eliminating their dependence on grid-connected power. TPV units for remote power generation offer advantages including high power density, low noise and no moving parts. Hybrid vehicle applications are also possible, and may lead to transportation options with reduced environmental impact. Unfortunately, the developmental pattern of TPV research has been concentrated on the advancement of individual system components, with relatively little attention to system integration [12].

Increased knowledge of TPV system performance in non-idealized situations is essential if commercial applications are to be realized. The use of readily available components is also necessary in order for these systems to be economically feasible.

1.7.2 Research Objectives

In order to improve thermophotovoltaic system knowledge, a prototype TPV system will be designed and constructed as a proof of concept instrument for commercial applications. Commercially available parts will be used as often as possible in order to reduce system costs. Overall system performance will then be measured and the effectiveness of various system components discussed.

The performance of the auxiliary equipment used in the system will be determined through measurement of emitter temperature, cooling load, and overall burner performance. The output of the TPV cells will also be investigated, providing information on cell power output, power density and fuel to electric conversion efficiency. Recommendations for future design improvements will then be made in light of these experimental findings.

The results of this study will be presented in the following order; first the current state of the technology will be portrayed through a literature review, leading into an in-depth explanation of the design and construction of a prototype thermophotovoltaic unit. The methods of testing, and the results from tests performed on this prototype unit will then be discussed, and conclusions and recommendations outlined.

2. LITERATURE REVIEW

2.1 History of Thermophotovoltaic Development

Thermophotovoltaics, the direct conversion of light to electricity, was first researched nearly 50 years ago by Dr. Henry H. Kolm [13] at MIT's Lincoln Laboratory (Lexington MA). His experiment used a Coleman camping lantern to provide light for Silicon cells to convert into electricity. Dr. Kolm's exploratory report concluded with the forecast that efficiencies of 5-10% were possible with proper system improvements.

Many literature references [14] credit Professor Pierre Aigrain with providing impetus for the research community to perform the first in-depth studies in thermophotovoltaics. During a series of lectures given in late 1960 and early 1961 while a visiting professor at MIT (Cambridge MA), he suggested the possibility of directly converting infrared radiation (IR) to electricity using a photovoltaic converter. Some of the MIT faculty seemed to be prompted by this lecture series, including Professors Wedlock and Gray, who later worked on the development of Ge cells.

In addition to the developments at MIT in the 1960s, the United States Army was also working to advance the technology. At this time, work was being performed to investigate if TPV could provide a portable, reliable, power source with no moving parts and low noise (acoustic). In fact, the US Army is still working with TPV systems to meet these same requirements, although increased demands on efficiency and power output are now in place [15].

The most notable advance to come from the U.S. Army's TPV research during this early period was Dr. Guido Guazzoni's work with a group of rare earth oxides found to emit with greater intensity in the waveband utilized by TPV cells [16]. This pioneering work is still being expanded upon today in order to increase TPV system efficiencies. By the mid 1970s, the U.S. Army abandoned most of the thermophotovoltaic research program, choosing instead to concentrate on more proven thermoelectric technology to meet the need for portable power.

A resurgence in non-military interest in thermophotovoltaic technology occurred in the 1970s due to the energy crisis in North America, which shifted attention from fossil fuel energy to renewable energy forms. Although TPV does not strictly fall into the category of a renewable energy source, increased research and development in solar cells helped TPV research, as many of the early TPV designs used solar (Si) cells. European organizations also began to contribute in this period, including groups from Germany [17] and Italy [18].

In the early 1990s, the National Renewable Energy Laboratory (NREL) in the United States began hosting conferences devoted to the development of thermophotovoltaics. These conferences enhanced the spread of knowledge throughout the research community and have had a positive impact on TPV development. NREL's interest in TPV systems in the 1990s was due, in large part, to renewed military interest.

Other contributors to TPV research in the last decade include [19] RPI (Troy, NY.), Sarnoff Corporation (Princeton NJ), Astropower Inc. (Newark, DE), Quantum Group Inc. (San Diego CA), McDermott Technology Inc. (Lynchburg, VA), Thermo Power Corporation (Waltham, MA), MIT Lincoln Laboratory, as well as Western Washington University and JX Crystals Inc. (Issaquah, WA). A recent withdrawal of interest in the past 5 years in the U.S. seems to fit the boom and bust cycle that TPV development has followed since its conception. However, the downturn in interest has this time been offset by increased interest from groups in Europe including The Fraunhofer Institute for Solar Energy Systems (Freiburg, Germany) and the Paul Scherrer Institut (Villigen, Switzerland).

2.2 Photovoltaic Operational Principals

The principals behind thermophotovoltaic technology are very similar to traditional photovoltaics, such as solar cells. In both processes photons are absorbed in a semi-conductor containing a built-in voltage barrier, or P-N junction – an interface of positively and negatively doped semi-conductors. These absorbed photons eject electrons from the (almost) filled valence band to the (almost) empty conduction band of the semiconductor atoms, as shown in Fig. 2-1. For each absorbed photon, a hole-electron pair of mobile charge carriers is created, and this mobile charge can then be collected across the PN junction to produce a current. To form this hole-electron pair, the energy of the photon must be greater than the energy gap between the valence band and the conduction band of the semi-conductor (this is commonly referred to as the bandgap energy).

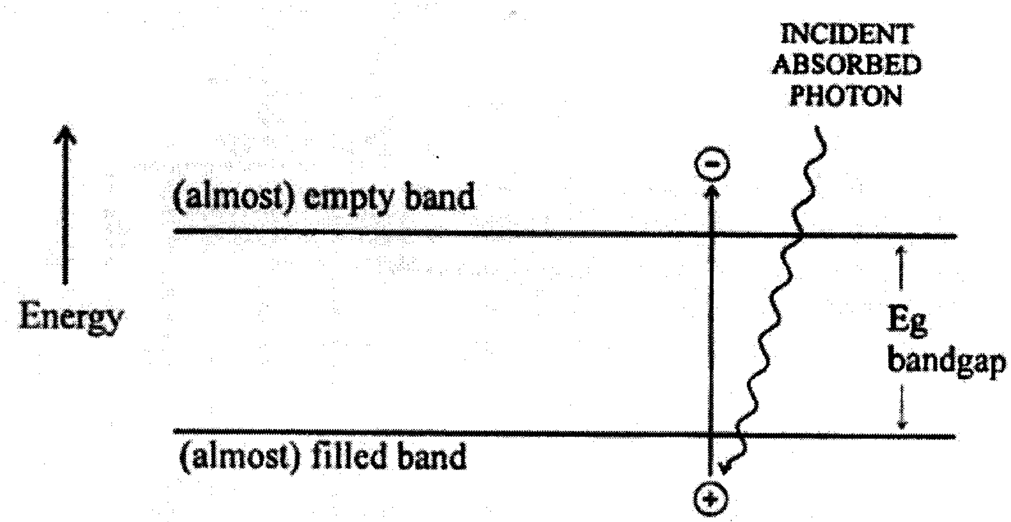

Figure 2-1: Operation Schematic of PV Cell [20]

Traditional silicon photovoltaic cells, as mentioned earlier, are designed to use the high-energy photons emitted by the sun, and although these cells are available currently at relatively low cost, they are not suited for use in TPV systems. This is due to the fact that silicon has a relatively high bandgap of 1.12 eV between its valence band and conduction band. Subsequently, in order to excite electrons to jump into the conduction band from the valence band, high-energy photons are required. Although these are readily available from the sun, in order to use silicon cells efficiently in a TPV system, emitter temperatures of over 2000K (1730°C) are needed. At this temperature, material degradation is a major problem, and components are prone to failure.

Photovoltaic systems with lower bandgap values than silicon cells include: gallium-antimonide (GaSb); indium-gallium-arsenide (InGaAs); and gallium-indium-antimony-arsenide (GaInSbAs) cells, with bandgaps of 0.73 eV, 0.68 eV, and 0.55 eV respectively. Of these three cell types, GaSb cells use technology similar to what is used to manufacture silicon photovoltaic cells, and therefore are relatively cheap to fabricate [21]. The InGaAs and GaInSbAs cells employ more complicated fabrication methods, and are therefore more difficult and expensive to manufacture.

A PV cell's performance is dependent on several factors including: illumination level; applied load; cell area; and cell temperature. A TPV cell responds to these influences in a manner similar to PV (solar) cells.

Illumination level is an obvious influential factor in cell performance, since PV cells use photons to knock electrons free and generate electricity. Here the illumination level is taken to mean the intensity of useable photons incident on the cell. Useable photons are those that possess energies greater than the bandgap energy (E_g), and therefore can knock electrons from the valence band to the conduction band of the semiconductor. Photons possessing energy lower than E_g generate waste heat by thermal excitation if absorbed by the photovoltaic cell.

Voltage has a limited response to illumination, and only varies under very low intensities. Once the illumination level has risen above a certain value, voltage remains constant. The larger impact is found on cell current, which has a proportional dependence on illumination level. The impact of cell area is similar, and has no effect on cell voltage, while having a proportional effect on cell current generation. These results are valid when considering a single cell only, and do not apply when multiple cells are connected in series or parallel circuits.

Another factor that has an effect on cell performance is the uniformity of cell or circuit illumination. When PV cells are joined together to form a circuit, the cell with the lowest current production limits the amount of current generated by the circuit. If a TPV emitter has non-uniform emission intensity along its length, the power produced by the system will be limited by the power production of the cell receiving the lowest illumination intensity.

Cell performance also varies as the applied load is changed, even if all other performance variables are kept constant. Under increasing load, the cell maintains a constant current output until such a point that it is no longer possible, and the current quickly drops to zero. An example of a graph detailing this behaviour, called a current versus voltage (IV) graph, is given in Fig. 2-2. Here it can also be seen that the point of zero current flow corresponds to the open circuit voltage (V_{oc}) value, and the point of zero voltage corresponds to the short circuit current (I_{sc}) value. The open circuit voltage and short circuit current values are the maximum cell voltage and current outputs possible at any one illumination intensity.

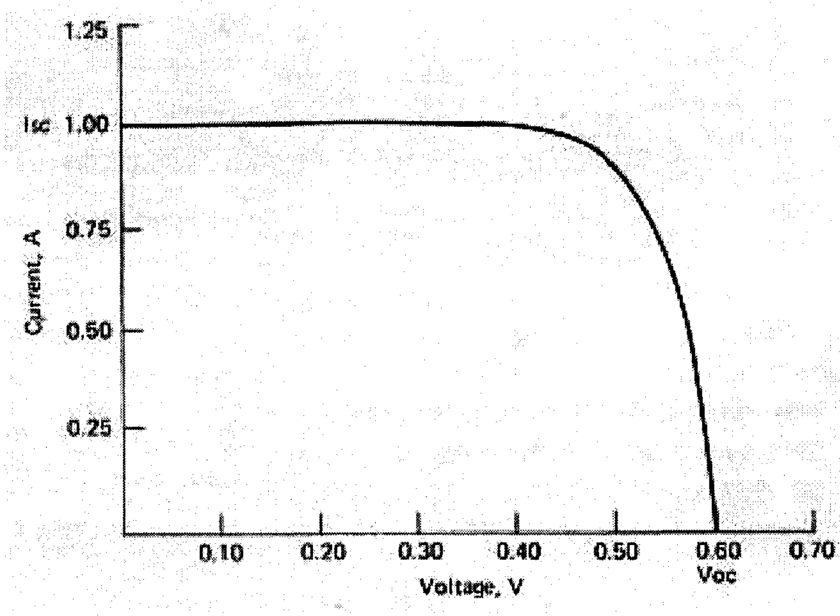

Figure 2-2: Typical IV Curve [22]

Cell power production (the product of voltage and current output) also changes with varying loads. A typical power curve is given in Fig. 2-3 and it can be seen that power increases with increasing voltage to a maximum power point (P_{max}) and then drops off to zero as the voltage value approaches V_{oc}. While the voltage value at the maximum power point (V_{max}) can be deduced from this graph, to determine the current value at the maximum power point (I_{max}), the power versus voltage graphs and the current versus voltage graphs are superimposed, as shown in Fig. 2-4.

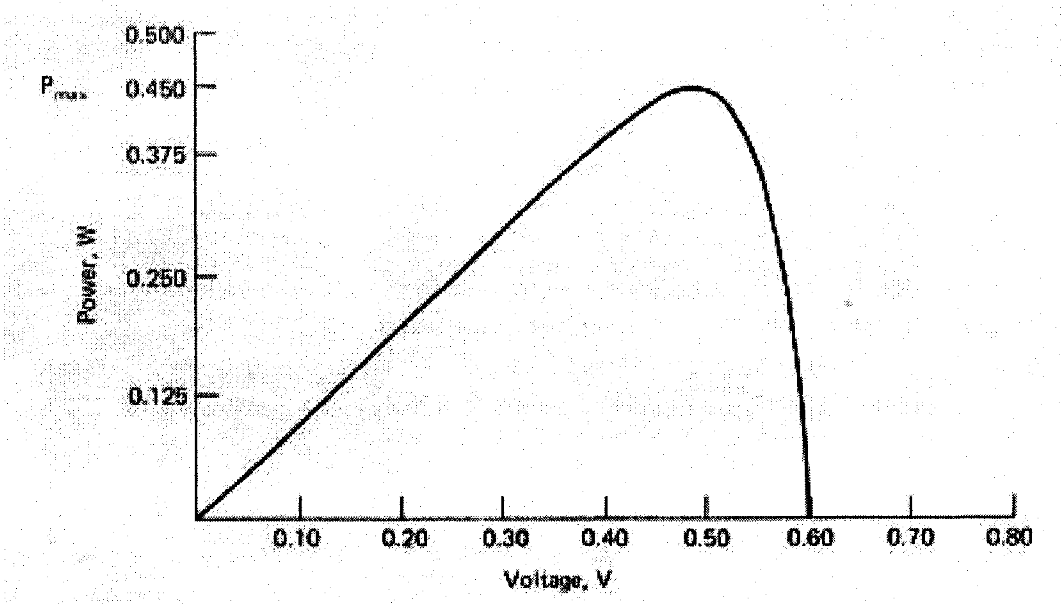

Figure 2-3: Typical Power Curve [22]

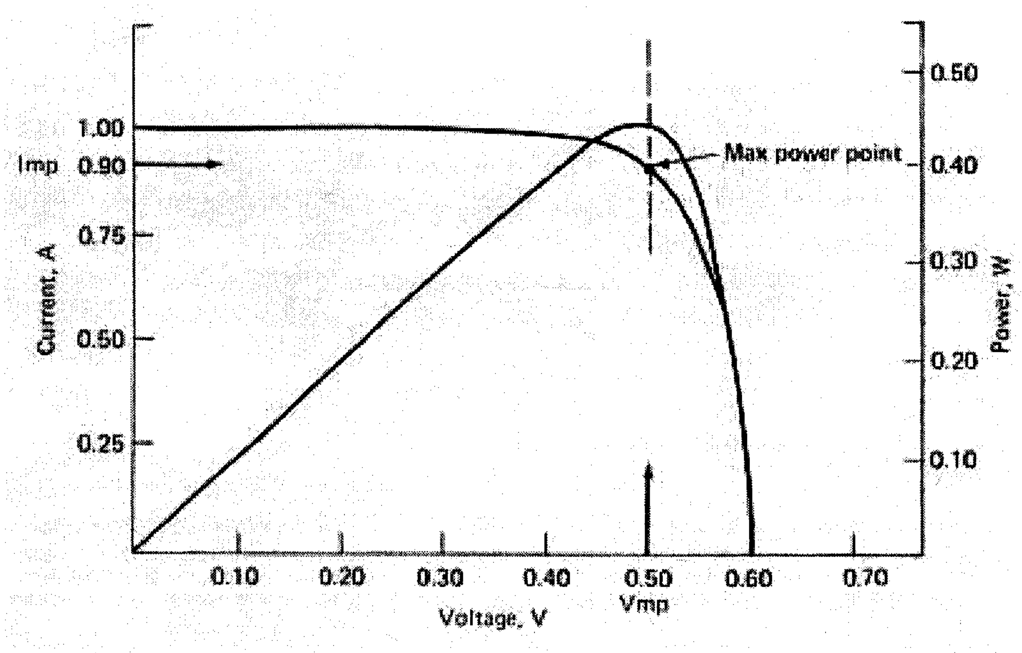

Figure 2-4: Superimposed Power and IV Curve [22]

The final factor influencing cell performance is cell temperature, which is inversely proportional to cell power output. This reduction in power output results from cell voltage decreasing with increasing temperature. Cell current is relatively unaffected by temperature variation.

Values commonly used to describe the performance of PV cells include V_{oc}, I_{sc}, I_{max}, V_{max}, P_{max}, and fill factor (FF). Fill factor is the ratio of the maximum power of a cell to the product of the cell's open circuit voltage and short circuit current, as given by the formula:

$$FF = \frac{V_{\max} \times I_{\max}}{V_{oc} \times I_{sc}} \tag{2.1}$$

where:

V_{oc} = open circuit voltage

I_{sc} = short circuit current

$V_{\max}$ = voltage at maximum power point

$I_{\max}$ = current at maximum power point

The value of the fill factor is a measure of the imperfections present in a PV system in the form of shunt and series resistances. Shunt resistance represents the amount of leakage between the positive and negative terminals of a PV cell. Series resistance refers to the resistance losses between the PV cell and the load. Ideally, the shunt resistance should be as high as possible, and the series resistance as low as possible.

2.3 Traditional Thermophotovoltaic System Design

A thermophotovoltaic system is typically comprised of four main components: a heat source; an emitter that converts thermal energy to light energy through photon emission; spectral filtering components to reflect/recycle non-usable wavelengths; and the TPV cells. A typical system schematic is given in Fig. 2-5. The arrows represent thermal energy transfer from the heat source to the emitter and photon emission from the emitter through the spectral filtering components to the TPV cells. A portion of the non-usable photons is recycled back to the emitter by the spectral filters. The remaining photons are then converted to DC power and waste heat by the TPV cells.

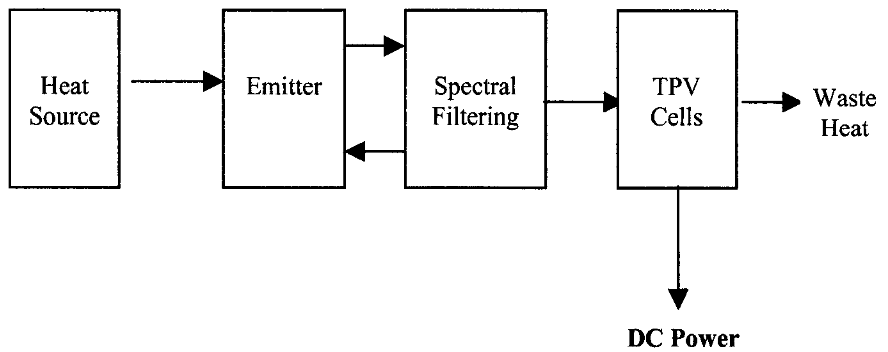

Figure 2-5. Typical TPV system schematic

A short review of emitter, spectral filtering and TPV cell technology will now be presented. Nearly all the work in the development of thermophotovoltaics has concentrated on individual component optimization (particularly emitter materials and TPV cells), with total system development only occurring in the last 5-10 years [5]. This overview is meant to expose the reader not only to the particular components used in the research apparatus constructed during this project, but also to components used in other systems in order to give a more balanced view of the technology as a whole.

2.3.1 Emitters

If the heat source is considered the heart of a TPV system, the emitter must be viewed as the circulatory system, taking the thermal energy and transporting it in the form of photons to the TPV cells. Generally, a TPV emitter can be one of two general types, employing either narrow or broadband emission. A common broadband emitter material is silicon carbide, which has high emittance values and good temperature stability up to

1900K. A high emittance is important in broadband emitters in order to transform as much thermal energy into electromagnetic radiation as possible. Since emittance values provide a comparison between the material and a perfect blackbody emitter, higher values result in increased emissive power at any particular temperature.

This transformation is also a function of temperature and as can be seen in Fig. 2-6, increasing temperature not only increases the intensity of emission, but also moves the peak of the emission curve to the left, as predicted by Wien's displacement law [23]. Shifting the peak emission to the left is desirable since it results in a higher proportion of the total emitted power falling within the waveband useable by TPV cells (represented in Fig. 2-6 as GaSb cells). Increasing the temperature is only practical to a certain extent, with material degradation problems of the emitter and other optical cavity components limiting temperatures to below 1600°C.

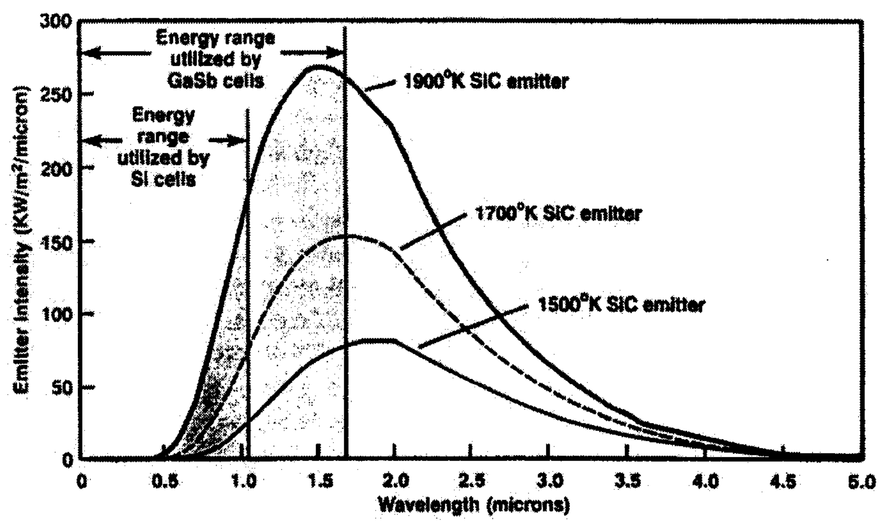

Figure 2-6. SiC Emission Spectra [24]

In actuality, combustion-heated broadband emitter systems have not been able to achieve emitter temperatures anywhere near 1600°C. Researchers have found that "any parasitic losses present in the optical cavity quickly defeat the attempt to recycle non-convertible, longer wavelength infrared energy with filters" [25]. This limited ability to recycle non-useable wavelengths results in increased waste-heat loss and decreased emitter temperatures. In review of the available literature, broadband combustion-fired emitter temperatures usually range from 1000°C to 1250°C.

One method that can be used to increase emitter temperatures and decrease energy loss via waste heat generation is to use an emitter that emits a high percentage of its energy within the narrow range useable by the TPV cells used in the system. This decreases the dependence on spectral filtering by preferentially emitting radiation in the useable waveband. Examples of this approach include selective and matched emitters.

Selective emitter materials include those incorporating rare earth elements, first studied by Guazzoni in 1972 [16]. The relatively narrow emittance of some of these rare earth oxides, including Ytterbia, Erbia, Holium and Ndium, is exhibited in Fig. 2-7.

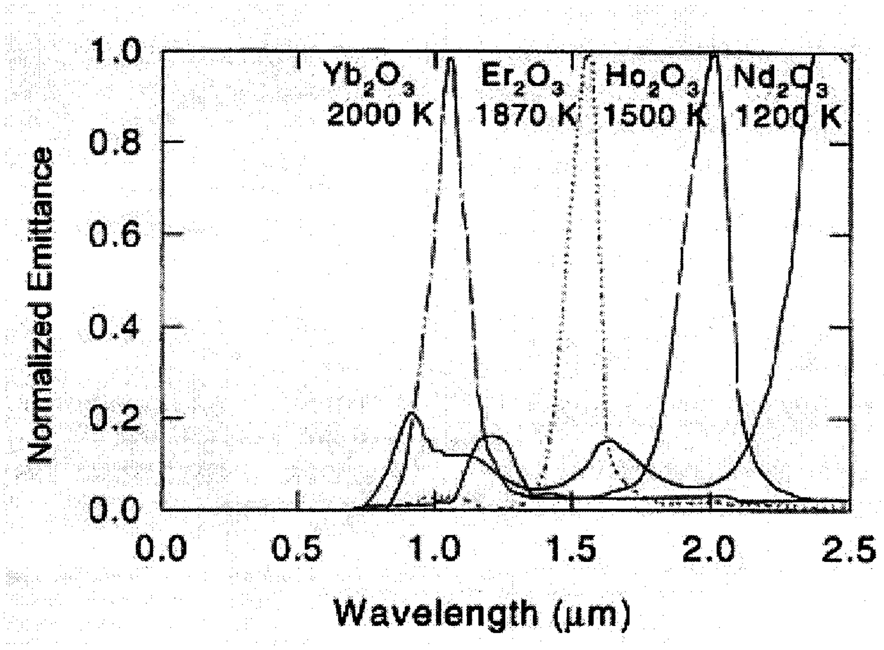

Figure 2-7: Rare Earth Oxide Emission Characteristics [26]

While these emission characteristics are advantageous from a spectral management point of view, they also pose problems as stated by Ferguson and Fraas [25]. The emission is sometimes too selective, resulting in emitters with low power densities unless extremely high temperatures are used. Other highlighted selective emitter problems include material lifetime problems and low chemical to radiation coupling efficiencies.

Emitter temperature measurement is also a problem when using selective emitters, since emission properties of selective emitters often change with temperature. Black or grey body emission characteristics cannot be assumed in these cases, and this continues to be a point of uncertainty in selective emission systems.

Manufacturing rare earth oxides into small diameter fibrous form has reduced decomposition due to differing thermal expansion properties between the rare earth oxides and their supporting substrates. This has mitigated poor spectral performance and material lifetime problems, which have traditionally accompanied selective emitters.

Another material that exhibits selective emission characteristics for use in TPV systems is tungsten, which has been found to emit over a limited range within the useable waveband of TPV cells. Research in this area is continuing in order to increase TPV system efficiencies using structured tungsten [27] as well as unstructured, antireflective-coated tungsten [28] emitters. The use of tungsten as a selective emitter material removes many concerns regarding material degradation since tungsten has the highest melting temperature of any element. This is complicated however, by the fact that tungsten only exhibits selective emission properties in its non-oxidized form. The tungsten must therefore be kept in a vacuum or inert atmosphere during system operation.

Matched emitters attempt to solve the low power density problem that plagues selective emitters by expanding the emission wavelength range. Co and Ni doped MgO have exhibited very favourable emission characteristics for a TPV cell utilizing wavelengths from 0.8-1.8μm [25]. The emissions from Ni-doped MgO and a theoretical blackbody are given for equal emitter power outputs in Fig. 2-8.

Figure 2-8 also highlights another advantage of using selective and matched emitters. For the same energy output, a selective or matched emitter will achieve a higher temperature than a broadband or black body emitter. This is due to the fact that the selective or matched emitter is constrained to shed energy in a narrow wavelength band. In order to reach thermal equilibrium, the selective/matched emitter will emit at a higher intensity than a blackbody within this narrow band. Since, by definition, nothing can emit at a higher intensity than a blackbody for a particular temperature, the selective/matched emitter material must be at a higher temperature than a broadband or near-blackbody emitter for the same power output. Figure 2-8 exhibits this by the integrated power under each curve being equal while the experimental Ni-doped MgO, and predicted blackbody temperatures differ.

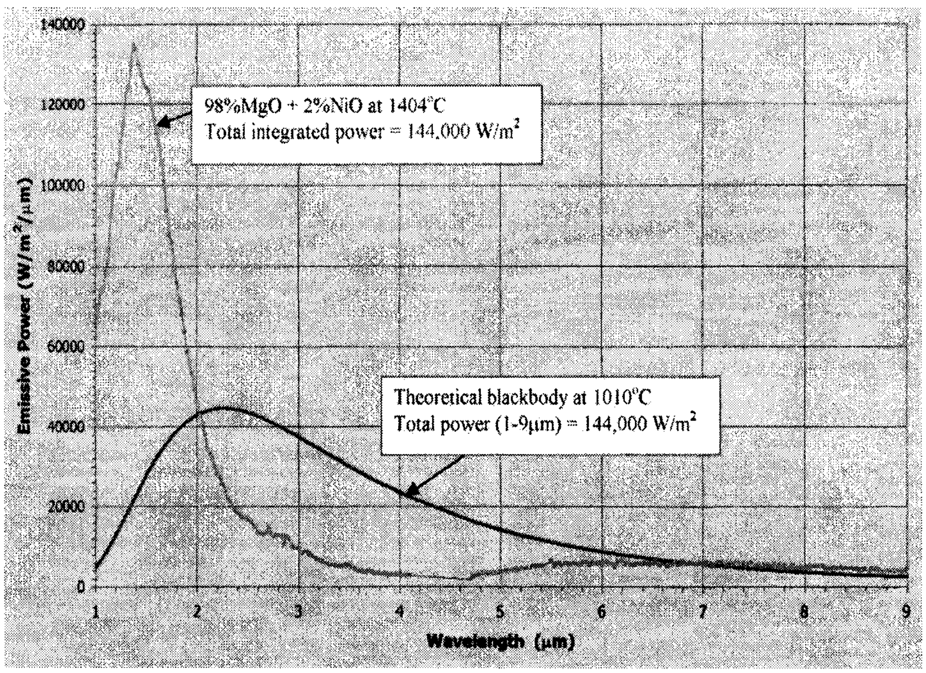

Figure 2-8. Ni-Doped MgO Emission [29]

2.3.2 Spectral Filters

Spectral filtering, initially regarded as a secondary system component and neglected, has been assigned greater importance with the progression of TPV system development. It was discovered early on that spectral filtering had a much larger effect on efficiency than first predicted, and if neglected, leads to low emitter temperatures and excessive cell heating. Some even attribute the lack of high efficiency (>10%), commercially available TPV generators to the absence of practical infrared filters that can withstand the operational environment in a TPV system [29].

The type and extent of spectral filtering required depends both on the type of emitter used, as well as the electromagnetic wavelengths useable by the TPV cell. Ideally, the spectral filtering component would recycle all non-useable photons back to the emitter, decreasing the required energy input to keep emitter temperatures high, and reducing the waste heat removal requirements of the TPV cells. Spectral filters used in various TPV systems vary from complex, including interference filters using 60 or more layers of coatings [30] and using electron beam lithography and masked ion beam lithography techniques [31] to fairly simple, including using quartz glass or water to absorb long-wavelength radiation [32].

One type of interference filter works on the principal of using alternating layers of two or more dielectric materials. By varying the thickness of the layers constructive and destructive interference, caused by varying refraction index values, results in certain wavelengths being reflected by the filter. This allows the designer to "tune" the light that is transmitted through the filter. Complexity of these dielectric stack filters increases as the range of wavelengths reflected by the filter is widened, with some proposed filters using as many as 60 layers [30]. The complex methods used to manufacture these devices is highlighted by the fact that although multiple layers may be used, the entire coating is usually only about 2μm thick.

Problems associated with dielectric stack filters include the inability of some dielectric materials to withstand high temperatures, and cost. Another important difficulty with these filters is the fact that they are generally designed for maximum filtering ability at one particular incident light angle. Light approaching the filter at an angle other than this is filtered less effectively. Since the emitters used in most TPV systems are diffuse (emitting in all directions), the observed effectiveness of most dielectric stack filters is lower than the theoretical maximum. One possible method to avoid this angular dependence is to use IR reflecting thin films such as indium tin oxide (ITO) and antimony-doped tin oxide (ATO), and work is continuing in these areas [3].

Another type of spectral filter that has been proposed (and patented) by Horne, Morgan and Sundaram of EDTEK Inc. (Kent, Washington) [33]. These filters are composed of sub-micron antenna elements that are etched into a metal film using electron beam or masked ion beam lithography. A photomicrograph of some of these antennae is shown in Fig. 2-9.

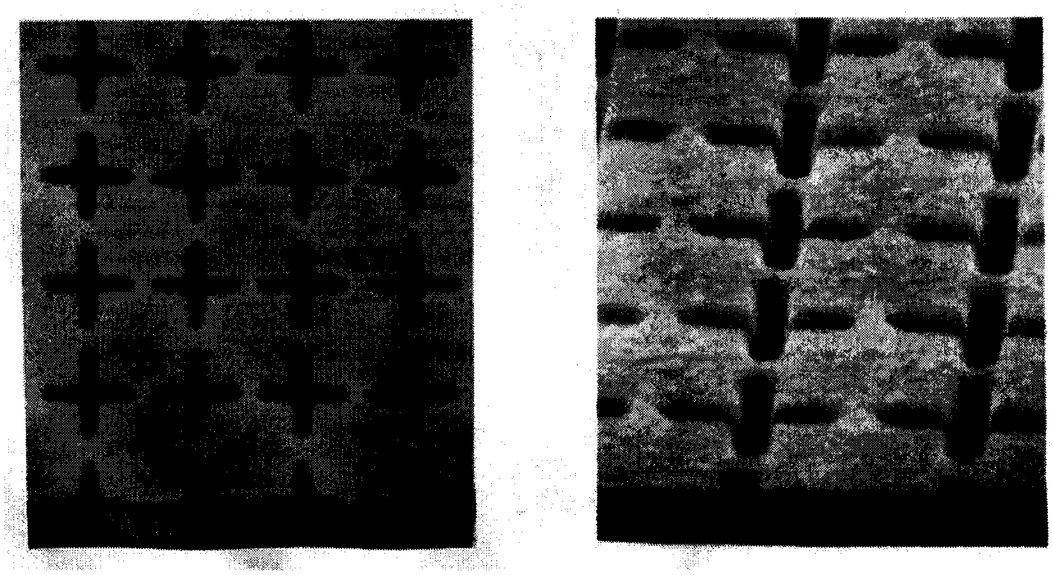

Figure 2-9: Detail of EDTEK Bandpass Filter [33]

The interaction of electric and magnetic fields on the mesh of the antenna elements causes inductive resonance to occur, creating a bandpass filter. The reflectance and transmittance properties of the filter depend on; the size, shape, and spacing of the elements, resistivity of the metal film, and dielectric and optical properties of the substrate.

Another, less complicated filtering method is to place a material that absorbs non-useable wavelengths between the emitter and TPV circuits. One such material is quartz, which has a relatively high absorbance for wavelengths greater than 3.5μm. It has been found that IR grade quartz (manufactured in the absence of water) performs best since it does not contain hydroxyl molecules, which have a characteristic emission band between 2.5-3.0μm [34]. Often, this quartz component is also used as a shield to protect the delicate PV cells from high temperature convective currents and exhaust gases in systems with combustion-heated emitters.

2.3.3 Thermophotovoltaic Cells

The evolution of TPV cell design has been the single most important factor in the advancement of thermophotovoltaic power generation systems. Early development of TPV cells concentrated mainly on silicon and germanium converters, resulting in relatively low conversion efficiencies [12]. This situation was improved by the high efficiency solar cell program conducted by the U.S. Department of Energy (DOE) which investigated photovoltaic cells based on III-V semi-conductors. This lead to the development of PV cells which have decreased bandgap energies and are more suitable for TPV systems.

The development of new types of cells and fabrication methods is still a very active area. The cells discussed in literature vary from relatively simple and cheaply fabricated GaSb cells [8] to relatively complicated and expensive cells such as Gallium-indium-antimony-arsenide (GaInSbAs). Increased complexity and cost usually results in cells with lower bandgap energies. This should in turn lead to a proportional increase in spectral efficiency, but recent findings have cast this theory into doubt [35], particularly at low emitter temperatures. Nevertheless, many believe that more advanced TPV cells are needed to bring the technology into the commercial marketplace [12]. This may include employing tandem structures where cells with different bandgap values are stacked on top of one another, and/or reflectors on the back surface of cells to reflect wavelengths that are not utilized by the semi-conductor back to the emitter.

2.4 Literature Review Summary

Based on the information compiled during the literature research, aspects of the prototype design that were identified as critical to the construction of an efficient, economically viable thermophotovoltaic power generation device included:

- a burner/emitter system capable of efficiently converting fuel to electromagnetic radiation at high temperatures. In order to simplify system complexity at this stage, a broadband emitter type was favoured over a selective or matched emitter.
- a spectral filtering system to minimize energy loss by recycling non-useable emissions back to the emitter.
- cost-effective, efficient and available TPV cells.

3. EXPERIMENTAL APPARATUS

The design process began once the basic principals for the prototype TPV unit were formed from a review of the available literature. One of the unique requirements for components in this system was that they had to be resistant to temperatures up to 1100°C (the maximum expected emitter temperature) unless actively cooled. This condition limited the types of materials that could be incorporated in areas such as the burner/emitter, as well as the types of insulation available to minimize energy loss.

Since one of the objectives of this work was to construct a commercially viable prototype, major system components such as the burner, spectral filtering elements and the TPV cells were not developed in-house, but obtained externally. This lowered the overall cost of the prototype by using off-the-shelf components as often as possible, and added to the commercial viability potential of the apparatus.

Throughout the design process the solid modelling package - SolidWorks 2003, (manufactured by the SolidWorks Corporation) was used to design the layout of the system and ensure the individual pieces would fit upon assembly. This proved to be a valuable tool, and was used to keep track of design changes, minimize space conflicts within the system, and generate drawings for part fabrication.

Preliminary design calculations, dealing with the proposed spectral control scheme that was later adopted into the system, and predicted cooling loads, are given in Appendix A. These calculations were used to formulate specifications for spectral filtering component and TPV cell performance, aid in the design of the cooling system, and give a preliminary indication of expected performance.

After the design details were finalized, a prototype thermophotovoltaic unit was constructed at the Alberta Research Council in Edmonton, Alberta. The main purpose of this unit was to serve as a proof of concept for possible commercial applications of the technology, one of the Alberta Research Council's core directives. Design, construction, commissioning and testing of this unit as reported in this volume occurred over a 26-month period, beginning in September 2001.

3.1 System Overview

A solid model representation of the experimental apparatus used in this study is given in Fig. 3-1 and Fig. 3-2. Figure 3-1 represents a longitudinal cross-section of the entire unit, where an overall length of just over 900mm (35.6") can be seen. Figure 3-2 is a lateral cross-section at a point approximately half way up the unit, and emphasizes the cylindrical design of the apparatus. Dimensions are presented both in millimetres and [inches]. The lower insulation piece, as well as the TPV cells and water-cooled channels on the backside of the unit have been hidden in Fig. 3-2 to provide a clearer view.

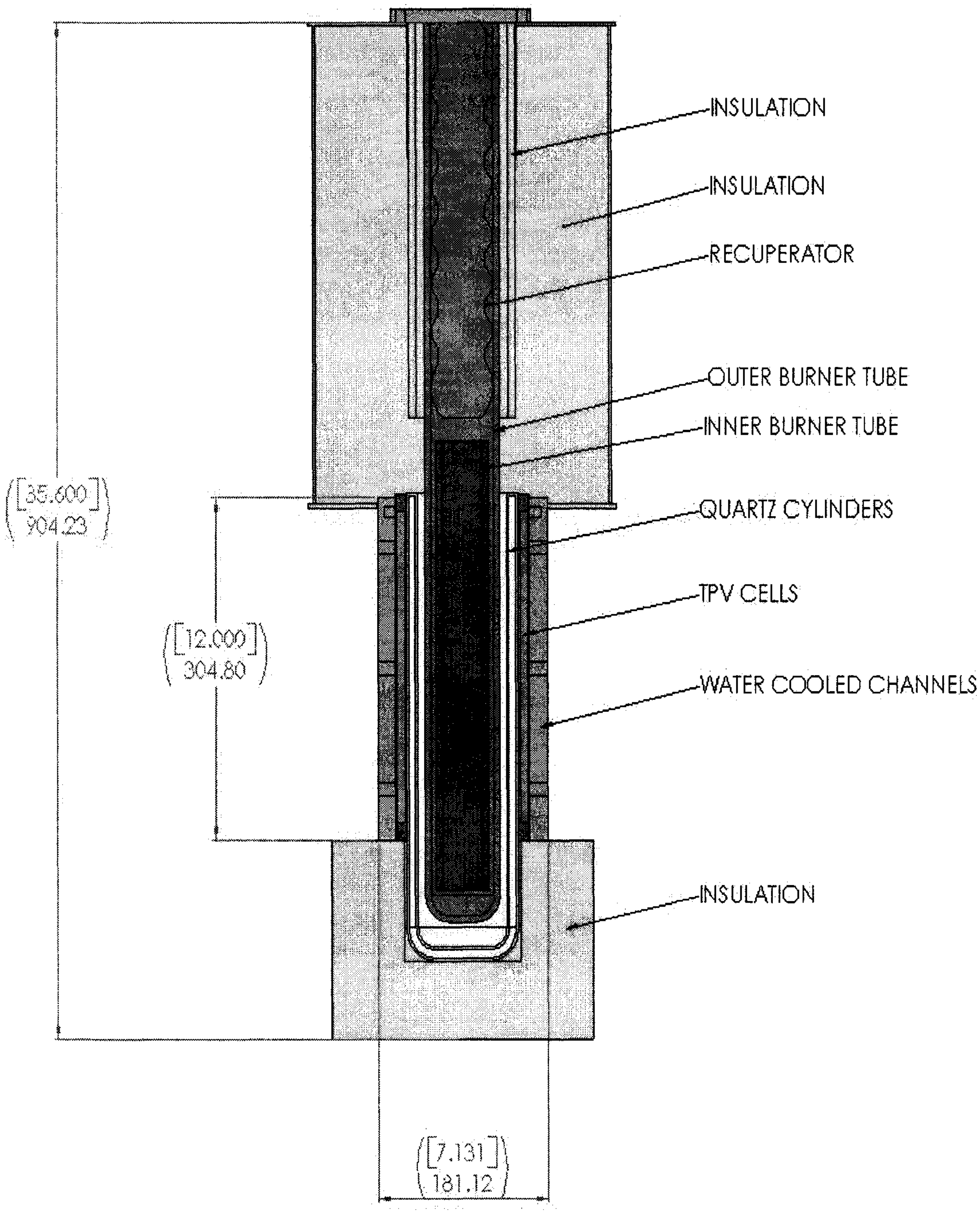

Figure 3-1: Solid Model Representation of Experimental Apparatus

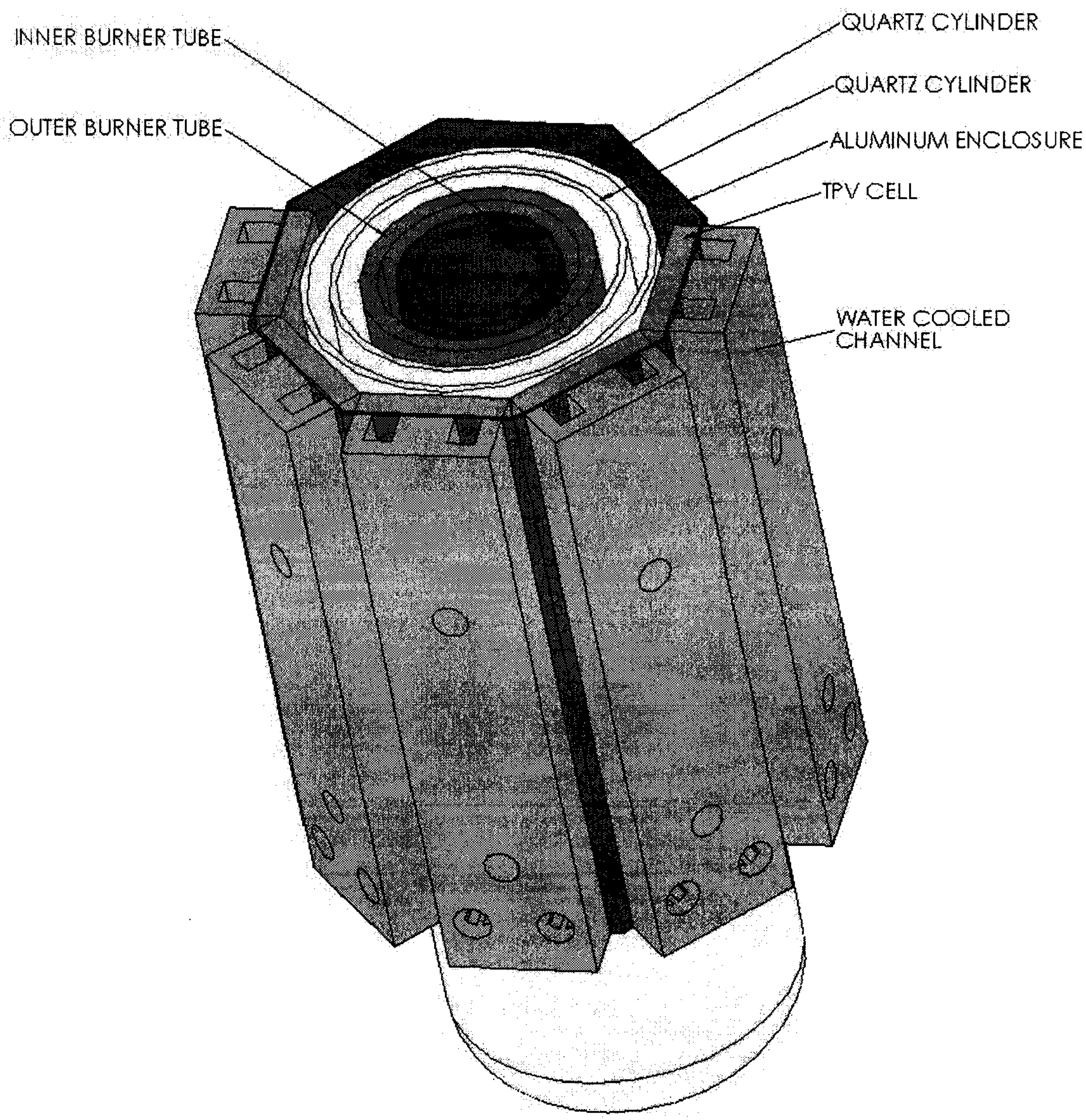

Figure 3-2: Lateral Cross-Section of Solid Model

This prototype represented by Figures 3-1 and 3-2 has been assembled at the Alberta Research Council in Edmonton, Alberta, and is pictured in Fig. 3-3. The unit is in operation in this photograph, with the lower section of the prototype (including the TPV cell enclosure, attached cooling channels and supporting insulation) lowered, to expose the burner/emitter.

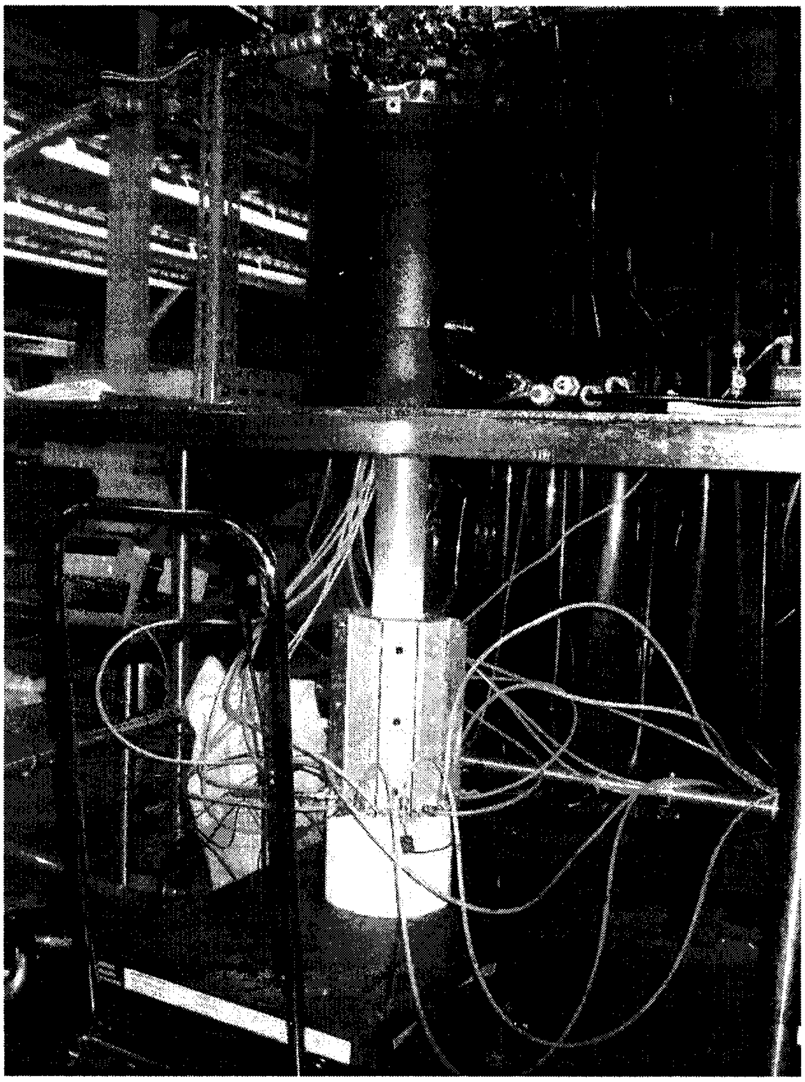

Figure 3-3: Operational TPV Prototype

3.2 Burner/Emitter

The unit is powered by a Rekumat C80 radiant burner, manufactured by WS Thermal Process Technology Inc. The burner has an outer diameter of 80mm and an overall length of 800mm. This was a convenient choice for this system due to the fact that the burner's mode of operation is to utilize combustion to heat an outer SiC tube to temperatures up to 1250°C [36]. The radiation from this outer SiC tube then heats the surrounding area, and acts as a broadband (grey-body) emitter for this TPV system.

By using a commercially available burner, custom design work involving ceramic components was avoided. Off-setting this advantage is the fact that the shortest burner available from WS is nearly three times longer than needed for this prototype, requiring a large portion of the burner be insulated to prevent excessive losses, as exhibited by the upper and lower insulated regions in Fig. 3-1.

In a schematic of a Rekumat© radiant burner, given in Figure 3-4, the burner's mode of operation is highlighted. As can be seen, the burner fires into an inner SiC cylinder, the combustion products then continue to the end of this cylinder, reverse direction and flow between the inner cylinder and an outer SiC cylinder, before passing over a internal recuperator and out to exhaust.

Using this configuration, WS claims to have a maximum temperature difference of 10°C over the 800mm length of this burner under normal operating conditions, such as installation in a furnace with uniform surroundings. This is important, as maximum TPV cell efficiency can only be achieved if the emission source is uniform over the length of the circuits. The advertised temperature uniformity was another factor in choosing this burner.

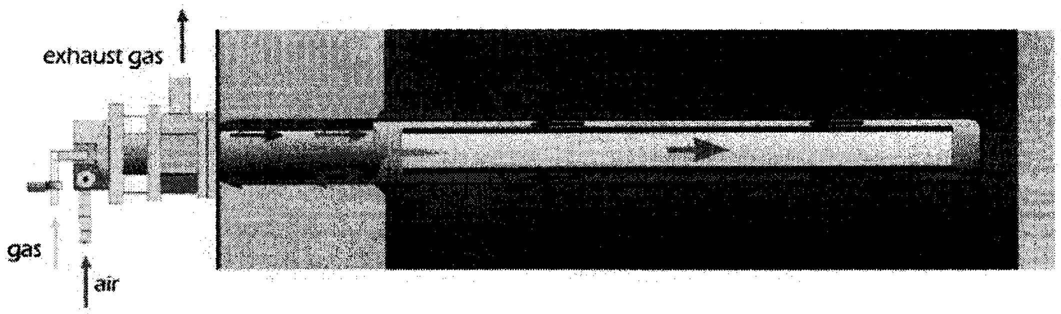

Figure 3-4: Operational Schematic of a Rekumat© Burner Manufactured by WS Thermal Process Technology Inc.

Burner ignition and monitoring were accomplished via a burner control unit (BCU) manufactured by Krom Schroder (model BCU-440). This system uses normally closed solenoid valves to control air and fuel flow during ignition and operation. During start-up, the BCU opens the air valve first, and then allows fuel flow to occur for a preset amount of time while activating an electronic ignition system. If ignition is not sensed by a flame ionization sensor within a certain period the control unit closes the fuel valve while purging the system with air and reporting an error signal on the control box.

If flame is sensed during electronic ignition, the system proceeds through a proving period before settling into the normal operation mode. If at any time during normal operation the flame ionization sensor does not sense flame, the fuel solenoid valve is closed while maintaining airflow to purge the system. A view of the burner control unit and control valves is given in Fig. 3-5.

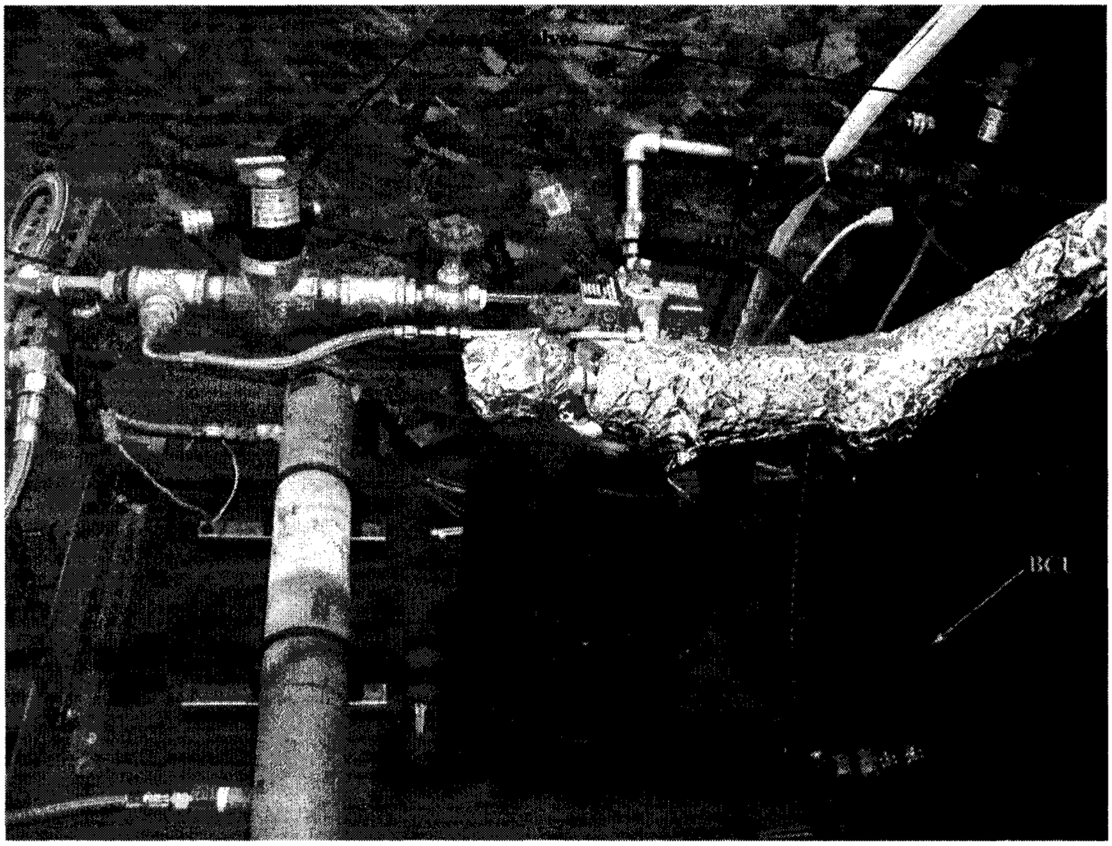

Figure 3-5: Installation View of BCU

3.3 Spectral Filtering Components

The range of wavelengths that can be converted to electricity in a TPV system or useable waveband depends upon the type of PV cells used. Based on the choice of PV cells used in this experiment (discussed in section 3.4), the waveband of useable radiation for this system is between 0.8μm-1.8μm. Ideally, all wavelengths outside this range would be reflected back to the burner surface in order to increase burner temperatures and decrease waste heat generation at the cell surface. In order to accomplish these goals, two spectral filtering components were utilized in this system.

3.3.1 Quartz Filters

The first spectral filtering component used in this system was a double walled quartz cylinder, as represented in Figures 3-1 and 3-2. Type 214 quartz manufactured by General Electric, was chosen for both cylinders because it is "dry" quartz, manufactured in the absence of water. This is important in order to minimize non-useable emissions in the 2.5-3.0μm range due to hydroxyl formation in quartz manufactured using water. The transmission characteristics of GE Type 214 quartz and typical "wet" quartz (manufactured in the presence of water) are given in Fig. 3-6.

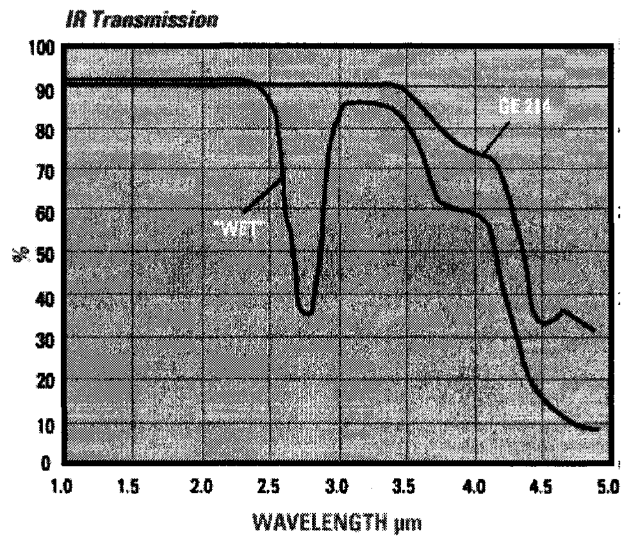

Figure 3-6: Quartz Transmittance Curve [37]

The inner and outer quartz cylinders have outer diameters of 90mm and 115mm respectively and a wall thickness of 2.5mm. Both cylinders are capped on the bottom and then joined together at the top, creating a sealed space between the two cylinders. This space was then evacuated to provide a thermal conduction/convection break between the burner and the TPV cells. A detailed drawing of this quartz component is provided in Appendix B.

The transmittance of type 214 quartz begins to diminish past 3.5μm, as seen in Fig. 3-6. At wavelengths beyond 3.5μm the role of the quartz switches from a transparent window to a long wavelength radiation shield, in order to decrease the intensity of off-band emissions reaching the TPV cells. The ability to absorb long wavelength radiation was the primary reason for incorporating quartz into this system, and although the absorbed radiation was re-emitted by the quartz, it was emitted in all directions, including back towards the emitter. To gauge the effect the two quartz layers had on the long wavelength energy transfer, a simple 1-D analysis [23] shows that of the radiation absorbed by the quartz, the amount that reaches the TPV cells decreases as 1/(N+1), where N is the number of quartz layers. For two quartz layers, the amount of energy beyond 3.5μm that reaches the TPV cells should be approximately 1/(2+1) or one-third the energy that is absorbed by the quartz.

3.3.2 Dielectric Filters

In order to minimize mid-wavelength (2-3.5μm) energy loss, nine-layer dielectric filters (manufactured by JX Crystals Inc.) were used as the second spectral filtering component in this prototype. Each filter was composed of nine alternating layers of silicon and silicon dioxide coated onto a 50mm x 75mm x 1mm quartz microscope slide. A single filter is pictured in Fig. 3-7 and a typical reflectance curve is given in Fig. 3-8. These filters were chosen based on their successful incorporation in previous TPV test stands fabricated by JX Crystals Inc., and their low transmission characteristics between 2-3.5μm.

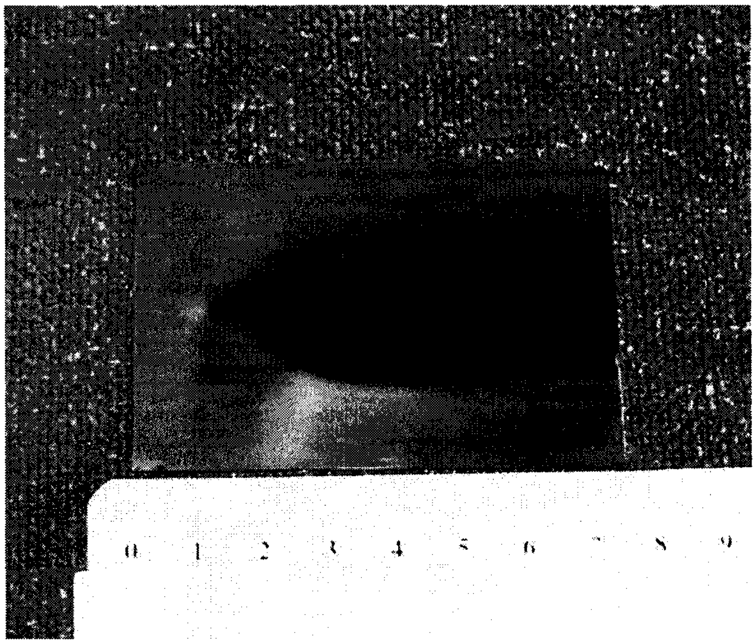

Figure 3-7: Nine Layer Dielectric Filter

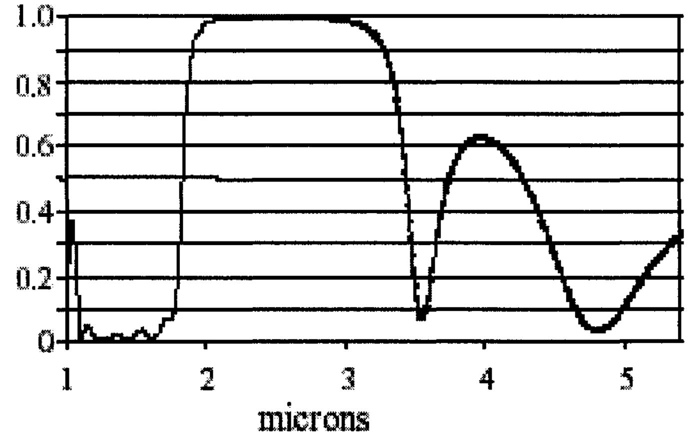

Figure 3-8: Nine Layer Dielectric Filter Reflectance Curve

3.4 TPV Cells/Circuits

Due to cost and availability, GaSb PV cells manufactured by JX Crystals Inc. (Issaquah, WA) were chosen for this project. The president of JX Crystals Inc., Lewis M. Fraas, co-invented the GaSb cell in 1989 while at Boeing, and in 1993 JX Crystals Inc. was granted a license to market the Boeing technology [38]. GaSb cells were purchased from JX Crystals in two configurations, as single test cells, and in 72-cell circuits.

Figure 3-9 shows a single GaSb cell unit as received from JX Crystals Inc. The cell is mounted on a copper substrate, with positive and negative leads attached. Dimensions of the GaSb cell are approximately 10mm x 14mm x 1mm. The circuits purchased from JX Crystals Inc., pictured in Fig. 3-10, are composed of three parallel circuits of 24 series connected cells, for a total of 72-cells per circuit. Circuit dimensions are approximately 50mm x 278mm x 6mm. Detailed drawings of both the single cell test unit and the GaSb circuit are provided in Appendix C.

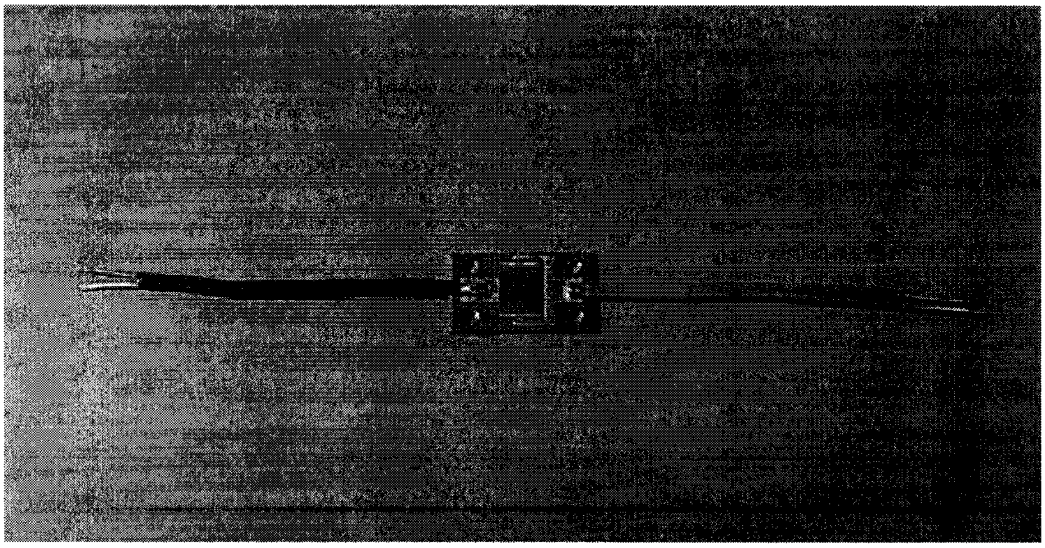

Figure 3-9: GaSb Test Cell

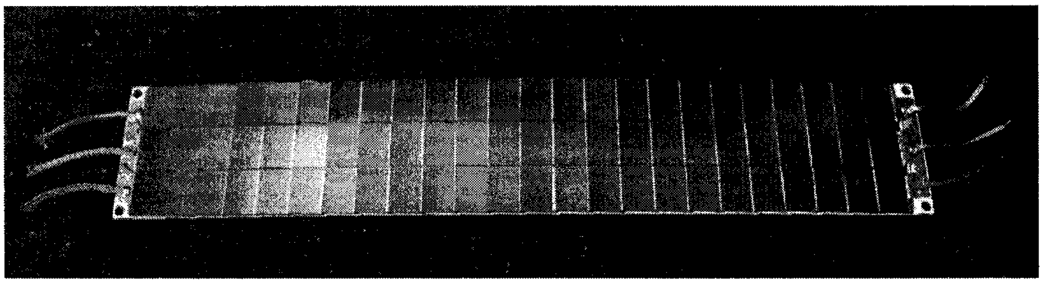

Figure 3-10: 72-Cell GaSb Circuit

A graph displaying the typical quantum efficiency characteristics of these GaSb cells is presented in Fig. 3-11. Quantum efficiency (QEext) is a measure of the cell's ability to convert photons to electrical current, and is dependent on wavelength. As shown below, wavelengths in the approximate range of 0.5-1.8μm can be converted to electricity with varying efficiencies.

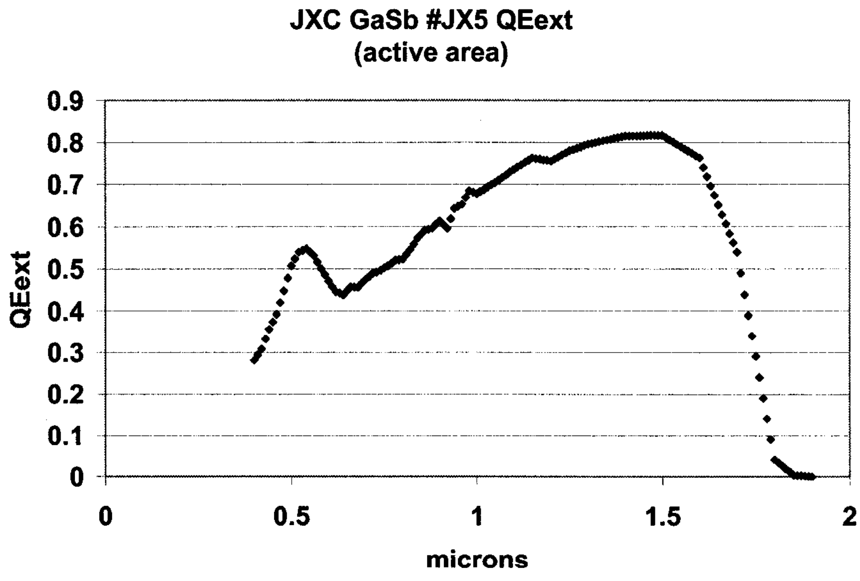

Figure 3-11: Typical Quantum Efficiency Characteristics of GaSb Cells Manufactured By JX Crystals Inc.

3.5 Optical Enclosure

A water-cooled enclosure was used to support both the single cell and 72-cell GaSb circuits. The eight-sided enclosure was manufactured from two 0.040" thick aluminium pieces, each bent into one half of an octagon and flanged at both sides to facilitate attachment via screws. To cool the enclosure, water channels were milled into aluminium bar-stock, and were then bonded to the outside surface of each of the eight enclosure faces. Figure 3-12 features a typical cooling channel, and Fig. 3-13 details the installation of these cooling channels on the outer faces of the eight-sided optical enclosure.

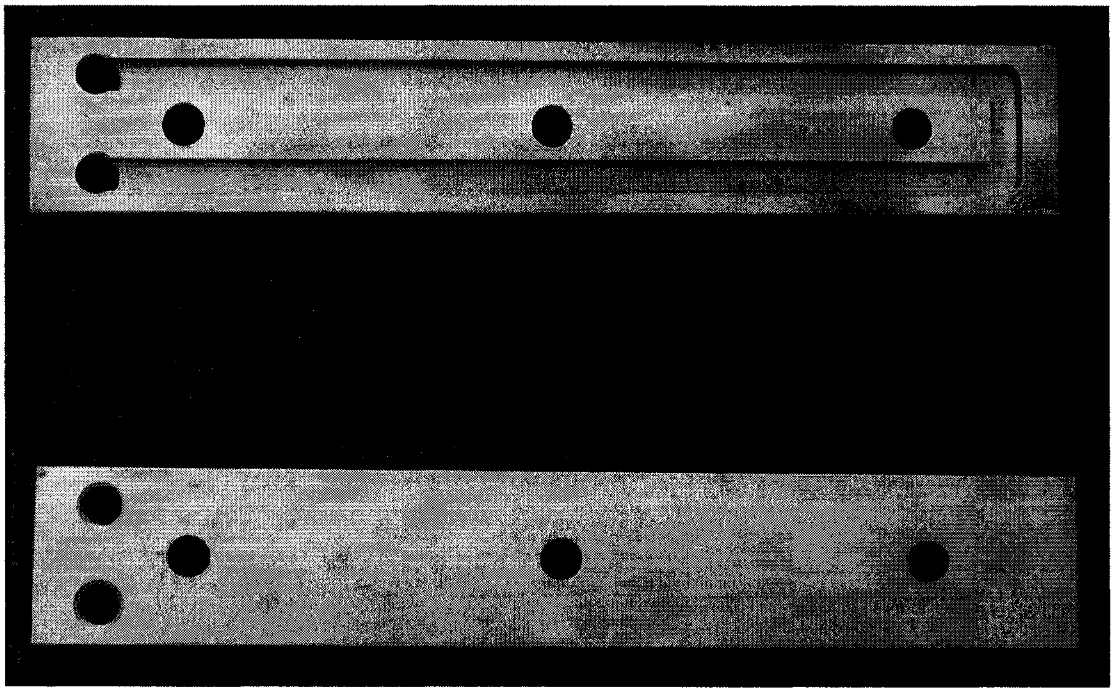

Figure 3-12: Typical Aluminium Cooling Channels

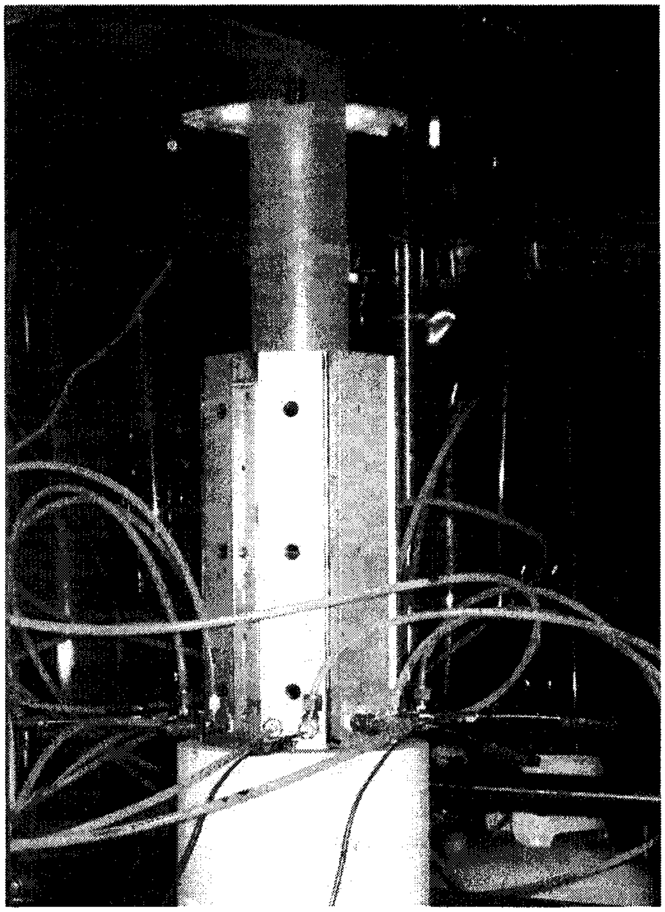

Figure 3-13: Mounted Cooling Channels

3.6 Data Acquisition

A process and information diagram (P&ID) for the thermophotovoltaic test bench is given in Figure 3-14. Mass flow controllers were initially used on both the air (AliCat Model MC-500SLPM-D/5M,5IN, range 0-500 SLPM) and fuel (Alicat Model MC-10SLPM-D/5M,5IN, range 0-10 SLPM) supply lines to set flow rates. These units are self-correcting for both pressure and temperature, requiring the user only to input the desired flow. It was later found that at burner firing rates greater than 10kW, the pressure drop across the air control valve resulted in insufficient flow. This required the valve to be removed from the controller, effectively reducing the air mass flow controller to a mass flow meter. Air flow was then controlled by a hand valve upstream of the meter (HV 004 in Fig. 3-14).

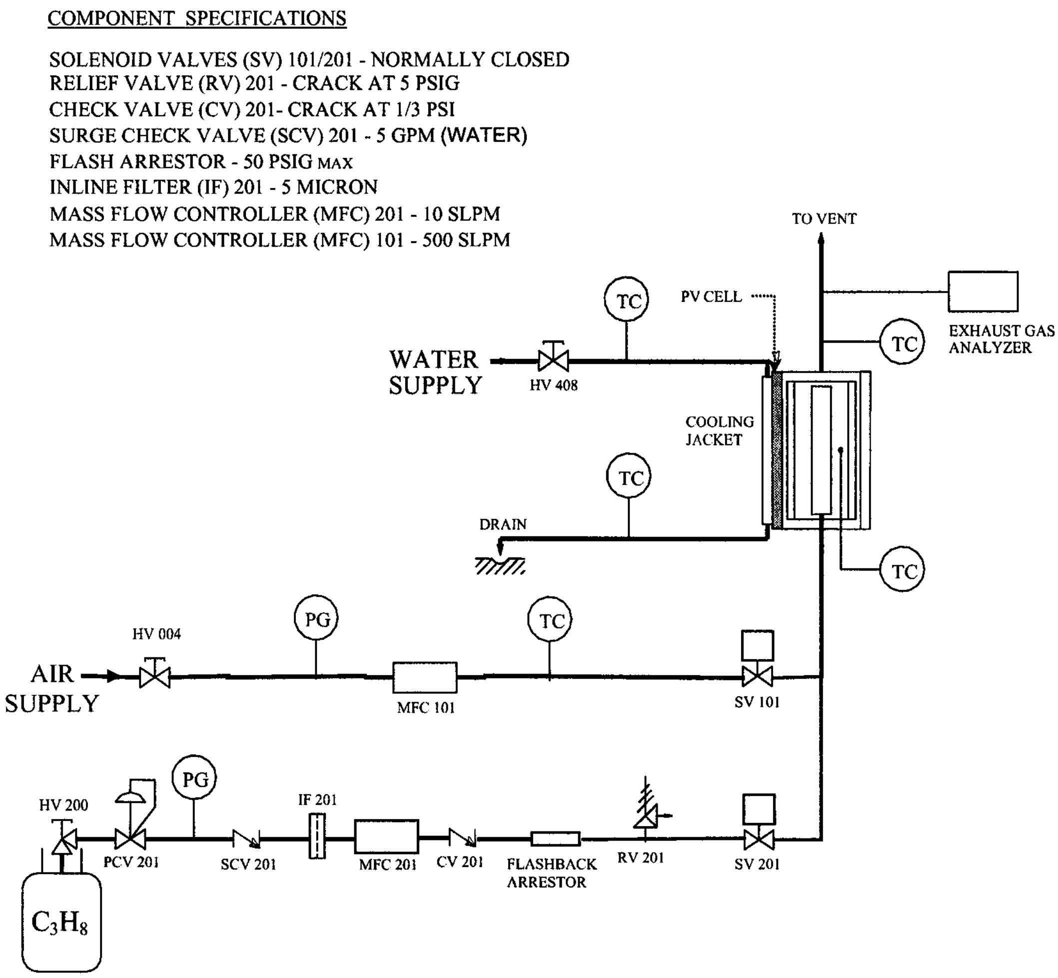

Figure 3-14: Thermophotovoltaic Prototype P&ID

Burner supply air was provided by a Regenair© regenerative blower manufactured by Gast Inc. (model R5325A). This model is larger than what is specified by the burner manufacturer, but was needed due to the additional pressure drop caused by the in-line air mass flow meter. Fuel (propane) was supplied by a standard 20lb bottle and two-stage regulator. A surge control valve, check valve, relief valve, and flashback arrestor were added to the fuel line upstream of the burner for safety reasons. Building supply water was used to cool the optical enclosure, with flow rates independently set for each of the eight cooling channels.

Thermocouples were used throughout the system to track energy flow. A Type T thermocouple was installed on one of the eight water inlet lines, upstream of the cooling channel, and was assumed to be representative of all inlet water temperatures. This was a reasonable assumption, since the same supply pipe supplied all water lines. Type T thermocouples were also installed on the exit fittings of all eight water channels, and used to determine the energy removal rate from the optical enclosure. Type K thermocouples were installed on the inlet and exhaust air streams.

A Hewlet Packard data acquisition/switch unit (model 3490A) was used in conjunction with a laptop computer to monitor and store data. Removable multiplexer cards (Agilent models 34902A and 34901A) provided communication between the air and fuel mass controllers and the data acquisition unit via RS-232 connections. Thermocouples were wired directly into the multiplexer cards and provided readings in degrees Celsius once the corresponding channels on the cards were programmed for the proper thermocouple type. The burner control unit (BCU) was utilized only to monitor burner operation (to ensure proper ignition and prevent an explosive situation by immediately stopping fuel flow upon sensing loss of flame) and was not connected to the data acquisition unit.

4. EXPERIMENTAL PROCEDURES AND RESULTS

Experimental testing of the prototype TPV unit progressed in two distinct stages. The first stage involved the use of single GaSb test cells to provide information on burner performance and the required cooling capacity of the optical enclosure without risking damage to the full-sized cells. Full-sized circuits composed of 72 GaSb cells were then installed during the second experimental stage, and performance data gathered. The same burner and auxiliary equipment were used in both testing regimes and only minor changes were made to the optical enclosures used to support the single cell and 72-cell circuits.

4.1 System Description Using Single GaSb Cell Test Units

4.1.1 Single GaSb Cell Test Units

As a first step in the design of the optical enclosure, test units consisting of a single GaSb cell were used to approximate full-sized circuit performance without endangering the full-sized circuits. This approach was taken due to the high cost of the circuits, and the fact that this was the first time a WS Rekumat© radiant tube burner had been incorporated into a TPV system. Figure 4-1 depicts the two GaSb single-cell units provided by JX Crystals Inc. used during testing. The cells pictured here have been mounted on copper plates used for positioning the cells on the outside of the optical enclosure.

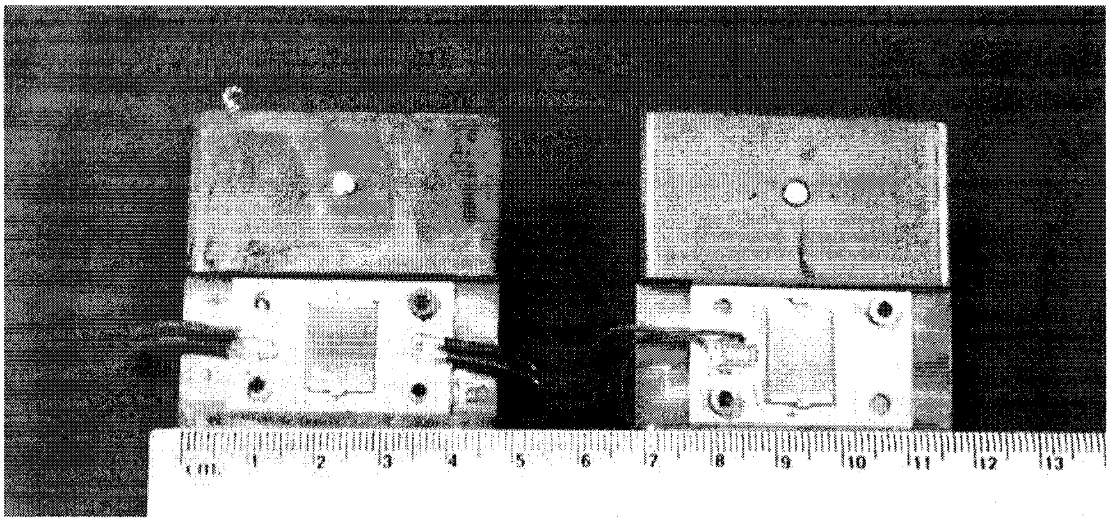

Figure 4-1: GaSb Single Cells

As can be seen in Fig. 4-1, the cells are not identical. The cell on the left has been wired in order to give an open circuit voltage (V_{oc}) measurement, and the cell on the right has a resistor wired across the positive and negative terminals. When a voltage is taken across this resistor, the short circuit current (I_{sc}) can be determined using the formula:

$$I_{SC} = \frac{V}{R_{resistor}} \tag{4.1}$$

where: Isc = short circuit current

V = measured voltage across resistor

$R_{resistor}$ = value of resistor wired across TPV cell

Figure 4-2 is a current versus voltage (IV) curve supplied with the single test cells. This curve was generated at JX Crystals Inc. using a flash stand apparatus in which tungsten bulbs were used to illuminate the cells with an intense flash of light for a very short period of time. Current and voltage values are recorded over this short interval, producing the graph in Fig. 4-2. The fact that illumination occurs over a short interval is important since cell performance changes with temperature, and cell heating during these tests is virtually non-existent. Other values, such as V_{oc}, I_{sc}, I_{max}, V_{max}, P_{max} and FF are also provided by this apparatus, and are listed beside the curve.

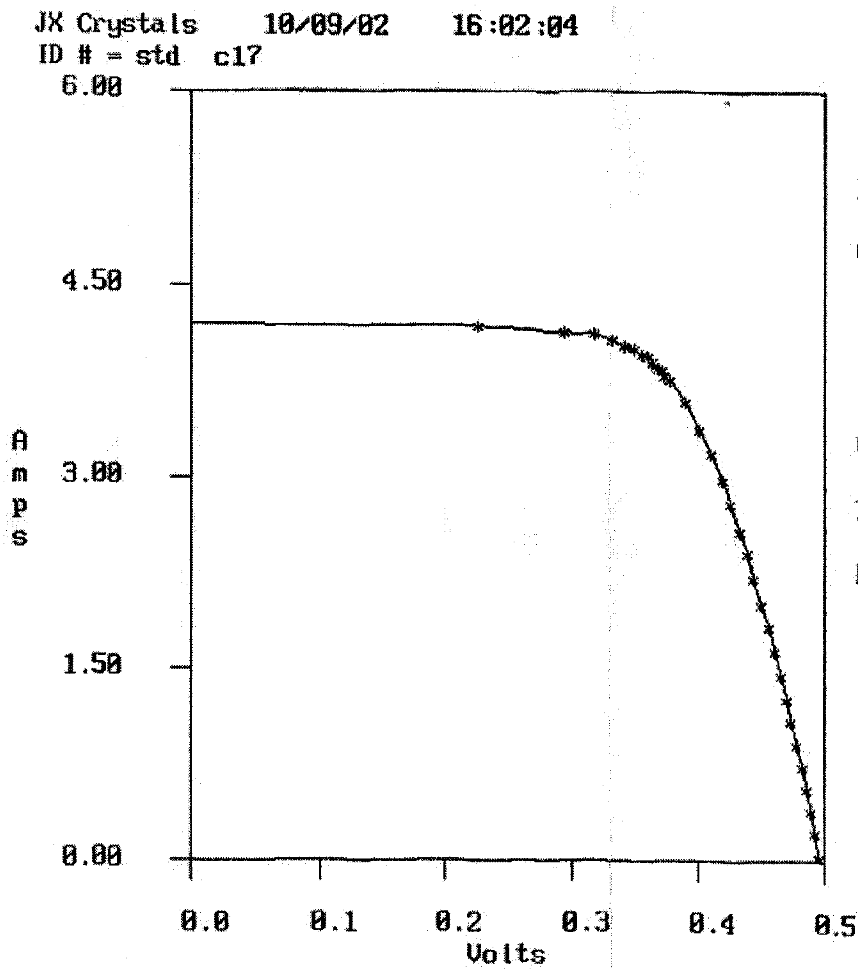

Figure 4-2: Single Cell Specification Curve

During system operation the single GaSb test cells were attached to the outside of the optical enclosure using the copper mounting plates exhibited in Fig. 4-1. These cells were then illuminated by the emitter through a 12mm diameter hole in the cooling channels and optical enclosure. A test cell mounted to the exterior of the optical enclosure is pictured in Fig. 4-3. Both the V_{oc} and I_{sc} test cells were mounted for each test run, on opposing faces of the octagonal enclosure. V_{oc} data, and the voltage values used to calculate I_{sc}, were recorded by the data acquisition unit.

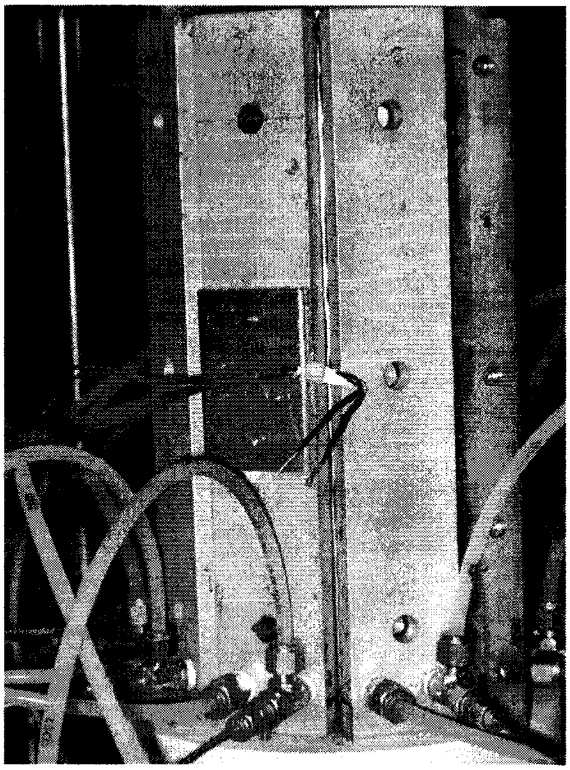

Figure 4-3: Mounting View of Single GaSb Test Cell

4.1.2 Spectral Filtering

Spectral filtering was provided by the double-walled quartz component discussed earlier, as well as the nine-layer dielectric filters provided by JX Crystals Inc. In this configuration, the dielectric filters were bonded to the interior faces of the optical enclosure using an optically transparent silicon-bonding agent manufactured by Dow Corning. Sylgard©184 is a two-part liquid component kit that is often used as an adhesive/encapsulant for solar cells. The base and curing agent were mixed at a 10:1 ratio, and then degassed in a vacuum environment for approximately 30 minutes. The degassing procedure removed any bubbles introduced by mixing the base and curing agent. Before the filters were installed, the interior surface of the optical enclosure was painted black to prevent reflection off the inner surfaces of the aluminium enclosure and capture as much of the energy passing through the dielectric filters as possible. This energy was then measured via the temperature rise in the cooling water on each of the eight enclosure faces.

The dielectric filters were bonded to the interior faces of the optical enclosure by applying the bonding agent to the back of the filters and mating to the painted surfaces of the optical enclosure. The bonding agent was applied as completely and evenly as possible to eliminate air gaps between the filters and the optical enclosure and enhance cooling. Placing the assembly in a convection furnace at a temperature of 125°C for a period of 20 minutes decreased cure times. Figure 4-4 details the interior of the optical enclosure after the installation of the dielectric filters.

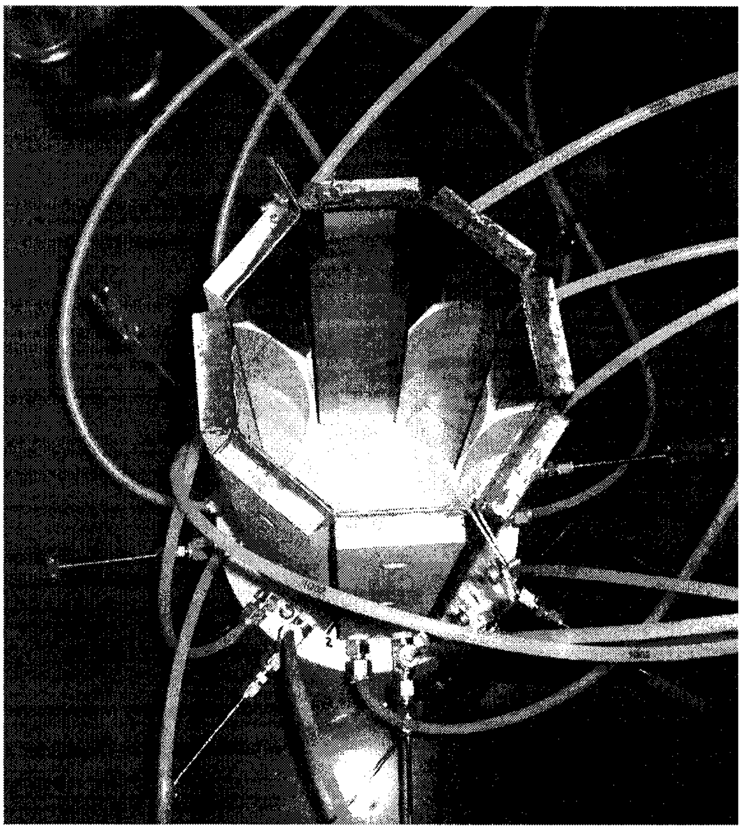

Figure 4-4: Installation View of Nine Layer Dielectric Filters on Inner Faces of Optical Enclosure

Since the single cell test units were mounted on the outer surface of the optical enclosure, light emitted from the burner had to pass through both the quartz and dielectric filters before illuminating the cells. This portion of the experimental apparatus was designed this way in order to emulate, as closely as possible, the conditions that would be present during testing of the full-sized circuits. Since results from high temperature radiation enclosures are very sensitive to changes in external boundary conditions, the configurations of the optical enclosures for the single cell and full-size circuits tests were made as close as possible to facilitate comparison of results.

During this phase of testing, optical temperature measurements were taken through view-ports similar to the ones used to illuminate the cells. In order to minimize error introduced by measuring the temperature of the burner through the spectral filtering components, an optical thermometer with a sampling frequency outside those affected by the quartz and dielectric filters was required. A portable infrared thermometer (model OS3707) manufactured by Omega Engineering Inc. fit these requirements. The spectral response of this instrument is 1.0-1.6μm, which is within the useable range of the GaSb cells, and outside the primary range of influence of both the quartz and dielectric filtering components.

4.2 Single Cell Experimental Procedure

General system operation began with the assembly of the optical enclosure, quartz filter and bottom piece of insulation. These components were placed on a cart with an adjustable-height platform. The inlet and outlet lines were then connected to each of the eight water cooling channels, and are shown as the white tubes attached to the bottom of each cooling channel in Fig. 4-5a. The cart was manoeuvred to center the quartz and optical enclosure on the outer burner tube, and the platform was raised to mate the components and seal the optical enclosure, as shown in Fig. 4-5b.

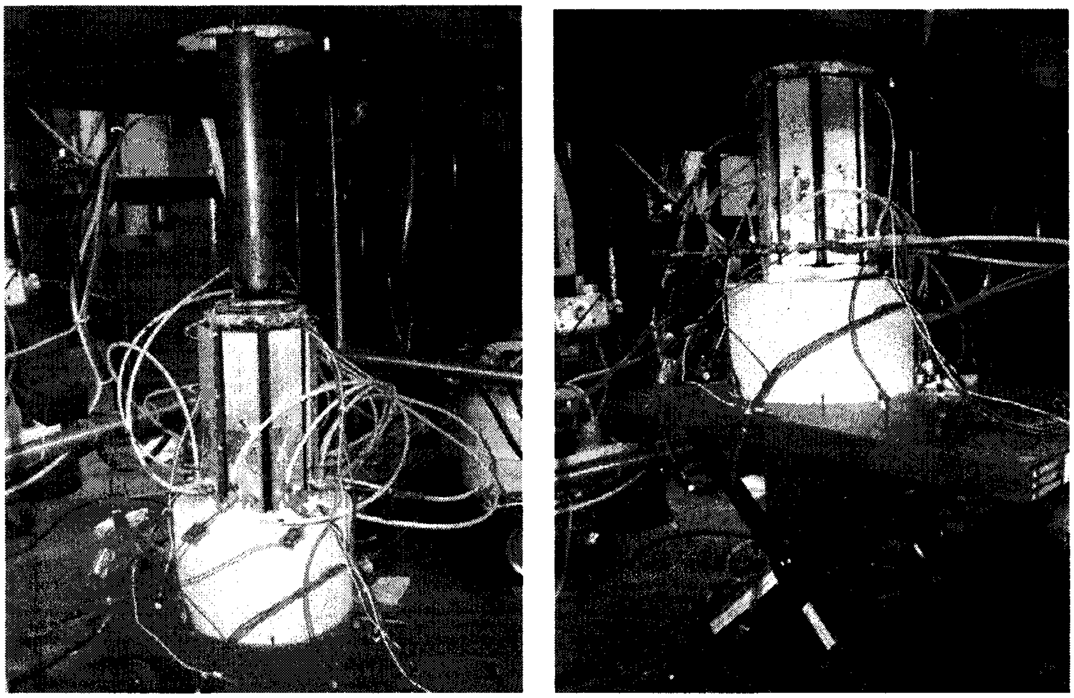

(a) (b)

Figure 4-5 (a) and (b): Positioning of Optical Enclosure

With the platform in position, the cooling water was turned on and adjusted to ensure a flow rate between 0.5-1.5L/min for each cooling channel (depending on the system firing rate). The combustion air blower, burner control unit and data acquisition system were then turned on. The desired fuel flow rate was programmed into the mass flow controller, and the valve on the propane bottle opened. Combustion airflow rates were set by adjusting a gate valve until the proper reading was displayed on the downstream air mass flow meter, and air was allowed to purge the system for 1-2 minutes before activating the automated ignition sequence through the burner control unit. Run times varied from 20 minutes to 6 hours depending on the goal of the experiment.

After the initial water flow rate measurements were performed, the optical thermometer was placed on a tripod and positioned to take readings through one of the view ports. An optical sight built into the thermometer aided positioning. The user was then required to set a dial indicating distance from the lens of the thermometer to the target. This was done by estimating the distance from the lens to the outer burner tube using a tape measure and then making fine adjustments to adjust the dial to the position at which the highest temperature reading was displayed. The method of adjusting to the highest temperature reading was also used when aiming and positioning the thermometer with the optical sight. A user input value of ε=0.85 was used for target emittance, based on spectral emission data received from the burner manufacturer.

4.3 Single Cell Test Results

One of the areas investigated during this portion of testing was the effect of emitter temperature on single cell performance. This is important because it provides an indication of cell output sensitivity to temperature. Optical enclosure cooling system performance was studied to determine the cooling load of the optical enclosure before full-sized circuits were installed. This was done to ensure the design of the system was capable of keeping the 72-cell circuits below their maximum recommended operational temperature of 90°C. The effect of spectral filtering components on cell performance was also studied in these initial test runs.

4.3.1 Single Cell Sensitivity to Emitter Temperature

Figure 4-6 highlights the relationship between single cell I_{sc} output and emitter temperature. This graph shows a power-type dependence exists between the two variables. A relationship of this type is expected since current production by photovoltaic cells is proportional to light intensity, which in turn has a relationship to temperature given by:

$$i'_{grey} = \varepsilon \frac{\sigma}{\pi} T^4 \tag{4.2}$$

where:

i'_{grey} = total intensity of a grey body (the SiC emitter can approximated as a grey body)

ε = grey body emissivity (approximated as $\varepsilon = 0.85$ for the SiC used in the outer burner tube/emitter)

σ = Stefan-Boltzmann constant = 5.67×10^{-8} W/m^{2}K^4

T = surface temperature

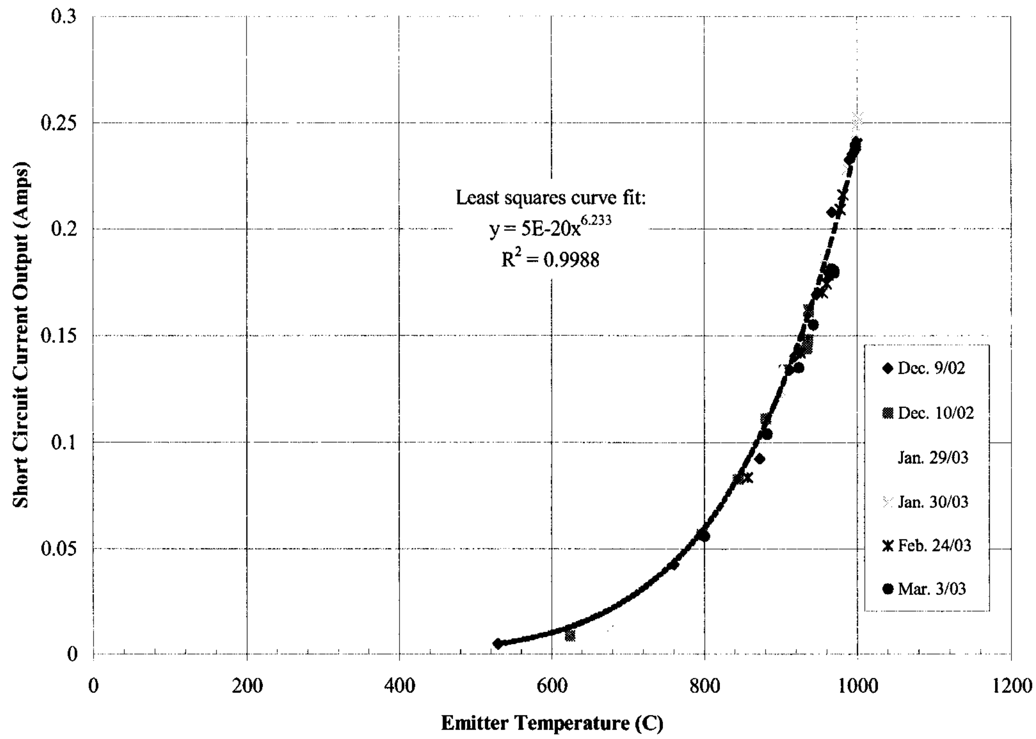

Figure 4-6: Relationship between Single Cell I_{sc} Performance and Emitter Temperature

Figure 4-7 displays the effect emitter temperature had on open circuit voltage for a single cell test unit. As expected, cell voltage rises with emitter temperature to a maximum value and then levels off, remaining relatively constant as emitter temperature increases. This behaviour is typical of that described in photovoltaic cell literature.

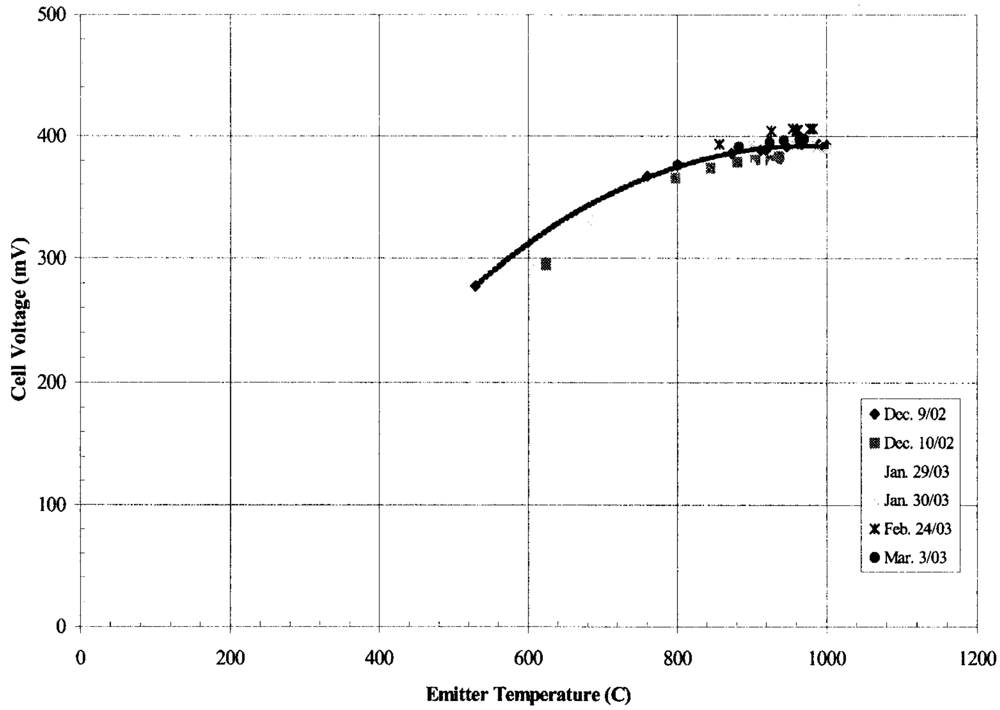

Figure 4-7: Relationship between Cell Voltage and Emitter Temperature for Single Cell Test Unit

During the emitter temperature measurements taken during the single cell tests, a temperature gradient was discovered on the emitter surface. Differing values for emitter temperature were found between readings taken at the mid-level view-ports (where the single cell circuits are mounted in Fig. 4-3) and the view-ports approximately 108mm above and below. The temperature difference between the mid-level view-port and the upper view-port ranged from 10°C to 15°C, while the temperature difference between the mid-level and bottom view-port ranged from 47°C to 55°C.

The temperature gradient was caused by the way the burner was incorporated into this system. The closed end of the outer tube/emitter was enclosed in a hollowed out cylindrical piece of refractory insulation as detailed in Fig. 3-1. This was done to provide a support surface for the optical enclosure, minimize radiant losses, and protect the surrounding equipment, but resulted in the emitter temperature being higher at this enclosed end (where it was surrounded by insulation) than within the enclosure.

Because non-uniform emitter temperatures can decrease the conversion efficiency of circuits constructed of multiple cells, this problem must be rectified for maximum electrical conversion efficiency. One possible solution involves placing a piece of high temperature insulation, such as alumina, inside the outer burner tube, near the bottom, where it is enclosed by insulation. This would remove the convective heat transfer from the combustion gases at the end of the tube and replace it with conduction heat transfer through the alumina insulation, reducing the temperature at the end of the tube, and compensating for the lower energy loss through the enclosure insulation. Apart from this conceptual design for a solution, no other work was done during this project to rectify the non-uniformity of the emitter temperature.

4.3.2 Cooling System Results

The performance of the cooling system for the optical enclosure was confirmed during this test period. Operating the burner at the maximum firing rate of 12kW resulted in a maximum enclosure-cooling rate of $6.34kW_{th.}$ The cooling water exit temperatures varied between 21°C and 35°C, depending on the water flow rate. Based on these results, no modification to the enclosure cooling system design was deemed necessary in order to provide proper cooling for the 72-cell circuits.

4.3.3 Spectral Filtering Results

At the end of this testing period, the spectral filtering components were removed to help quantify their effect on the system. Table 4-1 shows the results from tests performed with different combinations of spectral filtering components installed. Clearly both the quartz and nine layer dielectric filters have a significant impact on single GaSb cell short circuit current output. All tests were conducted using identical air and fuel flow setpoints.

The baseline case, where both the quartz and dielectric filtering components were installed, resulted in an I_{sc} output of 0.252A. System operation when the quartz component was removed resulted in a 33% decrease in I_{sc} output compared to this baseline case. Removal of the dielectric filters had a more pronounced effect and decreased the baseline I_{sc} output by 76%. An I_{sc} output reduction of 88% was found when both spectral filtering components were removed compared to when they were both installed in the system.

Table 4-1: Performance of single cell circuits under differing spectral filtering conditions

Date	Test Conditions	Voc (mV)	Isc (A)	Isc Decrease (%)
Jan.30/03	Quartz - I, Filters - I	387.7	0.252	0
Jan.29/03	Quartz - N, Filters - I	375	0.169	32.9
June 16/03	Quartz - I, Filters - N	332.3	0.06	76.2
June 12/03	Quartz - N, Filters - N	316.8	0.029	88.5

where:

I – indicates the spectral filtering component was installed

N – indicates the spectral filtering component was not installed

4.4 Full Size Circuit (72-Cell) System Description

Once testing with single cells provided data confirming the ability of the optical enclosure to remove waste energy at a rate sufficient to maintain the full sized circuits within their operational temperature range (< 90°C), the system was modified to install the 72-cell circuits. Every effort was taken to keep these modifications to a minimum and only minor changes to the optical enclosure were required.

4.4.1 Optical Enclosure Modifications

The differences between the optical enclosures used during the single cell and the 72-cell circuit tests were:

- cooling channels were shortened from approximately 305mm long to approximately 260mm long in order to allow clearance for four holes to be drilled through each face of the optical enclosure to mount the 72-cell circuits. The overall optical enclosure length of approximately 315mm was maintained.

- Each of the eight faces of the optical enclosure were lengthened by 5 mm, to allow for the increased thickness of the 72-cell circuits compared to the 1mm thick dielectric filters. This additional clearance was needed to prevent the circuit edges from clashing and led to an overall increase in the inscribed diameter of the octagonal optical enclosure of approximately 12 mm.

The effects of these changes are judged to be minor for the following reasons:

- The decrease in cooling channel length did not result in a significant decrease in the cooling capacity of the optical enclosure.
- Although the overall inscribed diameter of the optical enclosure was increased to allow enough clearance to install the 72-cell circuits, positioning the dielectric filters on the face of the circuits (see section 4.4.2) results in the dielectric filter-emitter distance being very similar (within 0.5mm) to the single cell case when they were mounted on the interior faces of the smaller octagon.

The optical enclosure resulting from these changes and the installation of the 72-cell GaSb circuits is described in the next section.

4.4.2 Description of 72-cell GaSb Circuits

The performance of each of the 72-cell circuits was tested before shipment from JX Crystals Inc. using the same flash test stand that quantified the performance of the single cell test units. The results of these tests are provided in Appendix D.

Upon investigating methods to mount the 72-cell circuits on the interior faces of the optical enclosure, it was observed that the substrates of the circuits were warped. This resulted in the back surface of the circuit being bowed along its length. The degree of warping was different for each circuit, and resulted in varying gaps between the circuits and the flat optical enclosure. This would have resulted in poor thermal transfer and possible circuit damage due to overheating if left unchecked.

In order to fill the gap between the circuits and the enclosure, a product manufactured by the 3M Corporation was investigated. Thermally Conductive Interface Pads, model 5509, with an uncompressed thickness of 2.5mm, were installed behind the circuits and then compressed into the shape of the gap by tightening the mounting screws at the four corners of each circuit. A Type J thermocouple was installed between the interface pad and the circuit, and the system was operated at low firing rates in order to observe the resulting circuit temperatures. Although the interface pads seemed to conform to the bowed circuits readily upon compression, their relatively poor thermal conductivity (5W/mK) resulted in inadequate circuit cooling.

Aluminium shims were then hand-made to match the individual shape of the gap between each circuit and the enclosure. A thermally conductive paste manufactured by Omega Inc. (Omegatherm 201) was used to fill any remaining voids between the aluminium shims and the mating surfaces of the circuits and the optical enclosure. A Type J thermocouple was installed between the back of the circuit and the shim, and the system operated to observe the resulting circuit temperatures. The increased thermal conductivity of the aluminium shims over the thermal interface pads allowed the circuits to remain within the required operating temperatures at all burner-firing rates.

Figure 4-8 details the positioning of four 72-cell circuits in one half of the optical enclosure. The circuits in Fig. 4-8 have not yet been fitted with nine-layer dielectric filters. The filters were bonded to the front surfaces of the circuits using Sylgard©184, manufactured by Dow Corning. Methods and procedures similar to those used to bond the filters to the inner surfaces of the optical enclosure during single cell testing were used to attach the filters to the front surface of the 72-cell circuits. Figure 4-9 details all eight circuits after installation of the nine layer dielectric filters. All tests performed on these circuits were done with the dielectric filters installed, in order to prevent circuit damage due to excessive absorption of non-useable wavelengths.

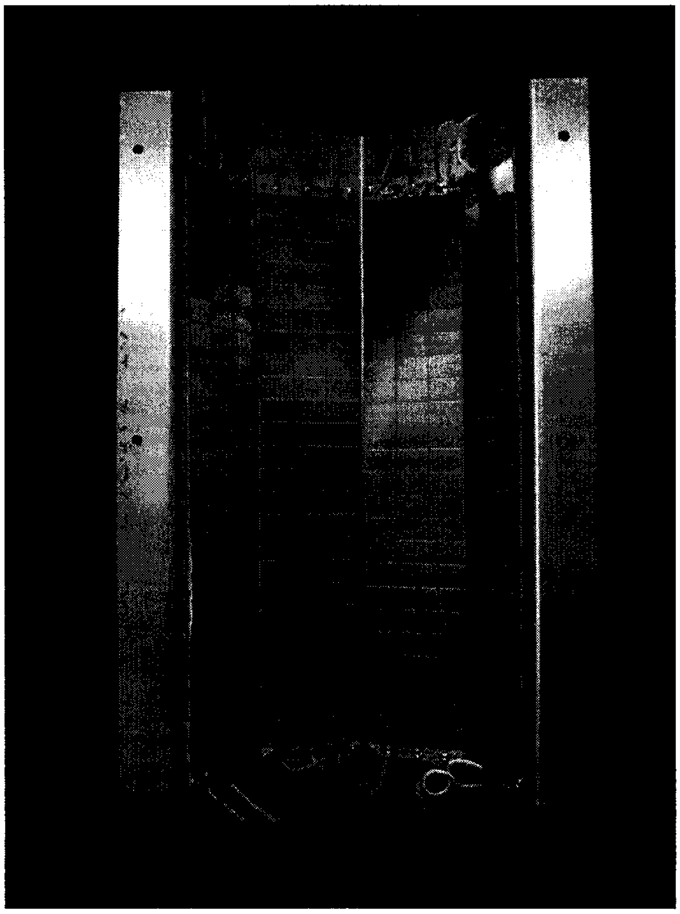

Figure 4-8: Typical Circuit Installation

Figure 4-9: Circuits with Dielectric Filters Installed

4.4.3 Burner Operation

Multiple tests were performed at different firing rates in order to obtain circuit performance data. In these initial tests, the burner and all other auxiliary equipment were set exactly as it was in the single cell test runs. A combustion analyzer (Kane May Quintox Flue Gas Analyzer, Model KM9106, manufactured by Kane International Ltd.) fitted with O_2, CO, NO, and NO_2 sensors, was then used to determine if the burner was operating efficiently. The results when the burner was operated at airflow rates determined by stoichiometric calculation (with 3% excess air), the operational procedure up to this point, were very poor.

Results obtained from the combustion gas analyzer showed that under these airflow rates the burner was oxygen starved, resulting in high CO production (>20,000 ppm), a key indicator of inefficient combustion. The combustion analyzer was not fitted with a hydrocarbon sensor, but at these levels of CO production, hydrocarbons were very likely present in the flue gas.

The operational procedure recommended by the burner manufacturer is to set air and fuel flows based on differential pressure measurements taken across orifice plates in the air and fuel supply lines. The burner used in this system was modified to set the flow rates using a mass flow controller for the fuel flow and a mass flow meter for the airflow. During initial configuration and commissioning, WS Thermal Process Technology Inc. was contacted to inquire about a slip stream that is taken off the air supply line (downstream of the mass flow meter) and used as cooling air for the gas lance traveling through the recuperator to the burner tip. If this cooling air was not used in the combustion process, additional airflow would have been accounted for at the air mass flow meter. The technical staff at WS confirmed that this cooling air was eventually mixed and combusted along with the other supply air, so no allowances were made.

The best explanation for the observed poor burner performance is that the cooling air, which mixes with the fuel at the burner tip rather than upstream with the balance of the air supply, does not mix efficiently and extra supply air is needed to ensure complete combustion. This may be accounted for when the burner is operated using differential pressure to set the airflow rate, but was not accounted for through the use of mass flow control. There is a need for additional investigation in this area, but no more was done during this project.

Since the burner was most likely not combusting all the fuel input during single cell testing, no data comparing cell performance to burner firing rate is given, or can be calculated, due to the fact that the exact firing rate of the burner is unknown. Therefore the data presented in the last section compares single cell performance to emitter temperature only.

4.5 Comparison of Single Cell and 72-Cell Circuit Results

The initial tests with the 72-cell circuits installed in the optical enclosure were performed using the same burner flow rates as used during single cell tests. Therefore a limited comparison of the data can be performed. In particular, since the fuel and air flow rates at any particular firing rate were the same, the emitter temperature in both cases should be similar. This emitter temperature similarity could not be confirmed during tests incorporating 72-cell circuits, since the installation of the circuits prevented a direct view of the emitter surface while the system was in operation. It is then of interest to see if a comparison of the open circuit voltage (V_{oc}) and short circuit current (I_{sc}) can be made between the single cell and 72-cell circuits. If these results can be correlated, the method of testing an optical enclosure by using a single cell mounted on the outside of the enclosure, without risking damage to full size circuits, can be confirmed.

In order to compare the single cell data to the 72-cell circuit data, simple series and parallel circuit theory was used. Since the 72-cell circuits are made up of three parallel circuits, each containing 24 cell cells wired in series, rules governing current producing devices wired in series and parallel were employed. As explained by Buresch [22], a parallel-connected photovoltaic circuit has an open circuit voltage (V_{oc}) and short circuit current (I_{sc}) values given by:

$$V_{oc\ PARALLEL} = \frac{\sum_{i=1}^{n} V_{oc\ LEG}}{n} \tag{4.3}$$

$$I_{sc\ PARALLEL} = \sum_{i=1}^{n} I_{sc\ LEG} \tag{4.4}$$

where:

$V_{oc\ LEG}$ = open circuit voltage of each leg of the parallel circuit

$I_{sc\ LEG}$ = short circuit current of each leg of the parallel circuit

n = number of legs in the parallel circuit

A series connected circuit has I_{sc} and V_{oc} values given by:

$$V_{oc\ SERIES} = \sum_{i=1}^{ncell} V_{oc\ CELL} \tag{4.5}$$

$$I_{sc\ SERIES} = I_{sc\ MIN} \tag{4.6}$$

where:

$V_{oc\ CELL}$ = open circuit voltages of individual cells in the series circuit

$I_{sc\ MIN}$ = minimum individual short circuit current value of all the series connected cells

$ncell$ = number of individual cells contained in the series circuit

These equations were used to approximate the response of just one cell in the 72-cell circuit during test runs performed on the full sized circuits before the burner malfunction was discovered. This approximation of single cell performance was then compared to data from the single cell tests. The results of this comparison are given in Tables 4-2 and 4-3.

Table 4-2: Single cell performance results during oxygen deficient burner operation

	Firing Rate	Voc	Isc	Circuit Temperature (deg. C)
Jan. 30/03	12kW	0.388V	0.252A	28.5
Dec. 9/03	12kW	0.393V	0.242A	24.33

Table 4-3: Approximated performance of a single cell within a 72-cell circuit during oxygen deficient burner operation

	Firing Rate	Voc (single cell equivalent)	Isc (single cell equivalent)	Circuit Temperature (deg. C)
Sept. 18/03	12kW	0.348V	1.09A	59.5
Oct. 10/03	12kW	0.351V	1.06A	58.4

As can be seen in these tables, the V_{oc} values for the single cell and 72-cell cases are relatively close. The difference between the V_{oc} values of the single cell cases and 72-cell cases is explained by the fact that V_{oc} is inversely proportional to temperature, and the tests were performed at different cell temperatures. From the single cell tests (Table 4-2), the proportionality constant between voltage and temperature was calculated as:

$$\frac{0.393V - 0.388V}{24.33°C - 28.50°C} = -1.20x10^{-3}\frac{V}{°C}$$

Using the single cell V_{oc} values as a starting point, and by applying the proportionality constant to the temperature readings for the 72-cell circuits, the 72-cell V_{oc} values in Table 4-3 are predicted to within 0.003V, or 0.9%.

The I_{sc} values of the single cell and 72-cell circuit did not prove as comparable as the V_{oc} values. As can be seen in Tables 4-2 and 4-3, the I_{sc} values of the single cell tests were considerably lower than the single cell equivalent values calculated from the 72-cell circuit data. These single cell equivalent values were calculated by applying equations 4.3

to 4.6 to approximate the output of a single cell within the 72-cell circuit. Since both the single cell and 72-cell tests were run at the same air and fuel flow rates, the burner temperature and emitted light intensity are assumed to be comparable.

Since cell current is proportional to light intensity, it was expected that the single cell and single cell equivalent values for I_{sc} would be approximately equal. This was shown not to be the case. Possible reasons for this include the single cell circuit being approximately 20mm further away from the emitter than the 72-cell circuit. This results in the emitted power intensity from the cylindrical emitter being reduced by 40%. Even when the proportional effect that illumination intensity has on current production was taken into account, the single cell results do not match the approximated single cell results from the 72-cell circuits.

Another source of error that could have had an effect on the single cell current production is the overshadowing condition encountered on the corners of the single cell. This error was introduced due to mismatch between the 12 mm diameter hole used to illuminate the test cell and the 10mm x 14mm single cell itself. Parasitic losses caused by overshadowing in photovoltaic systems are difficult to predict, as stated by Buresch [22], and can be appreciable depending on the configuration of the system and the type of photovoltaic cell used. Along with overshadowing error, the absorption of photons on the inner surface of the approximately 20mm deep viewing port through the cooling channels and optical enclosure was also unaccounted for. Due to the discrepancy between the I_{sc} values of the single cell and 72-cell circuits, a single cell mounted on the exterior of this enclosure cannot be used to accurately predict optical enclosure performance with full sized, 72-cell circuits installed.

4.6 Modified Burner Operation and Performance

In the tests following the discovery of poor burner performance, the optimum airflow for each firing rate was found using two indicators. The first indicator was CO production since excessive CO production is often an indication of inefficient combustion. If the combustion gas analyzer in the exhaust stream sampled relatively high levels of CO, the airflow was increased. Since increasing the airflow can lead to high excess air levels (which act as an energy sink in the combustion process) a second indicator was used to locate the maximum emitter temperature for any particular burner-firing rate. Since current output from these circuits is directly proportional to light intensity, I_{sc} output of the 72-cell circuits was used. These readings gave a relative measure of an increase or decrease in emitter temperature for a change in airflow.

Between these two parameters, optimum burner operating points were located at firing rates between 6kW and 9kW. CO level in the exhaust was a good indicator of burner performance, and measured between 18-26 ppm at all optimized firing rates. To ensure no hydrocarbons were escaping in the flue gas, gas samples were analyzed by a gas chromatograph (Hewlett Packard Series II, model 5890) utilizing a Poroplot Q, 30-meter column. At the optimized operating points no hydrocarbons were discovered in the exhaust gases, as can be seen in the outputs from the gas chromatograph, given in Appendix E.

Figure 4-10 shows a linear relationship between combustion air flow rate and burner firing rate resulting from using the two parameters described above to set the optimum airflow rates for operation between 6kW and 9kW. This linear relationship is useful since it decreased the guesswork and time needed to attain the proper airflow rates for optimized burner performance, and removed the requirement of constant flue gas monitoring.

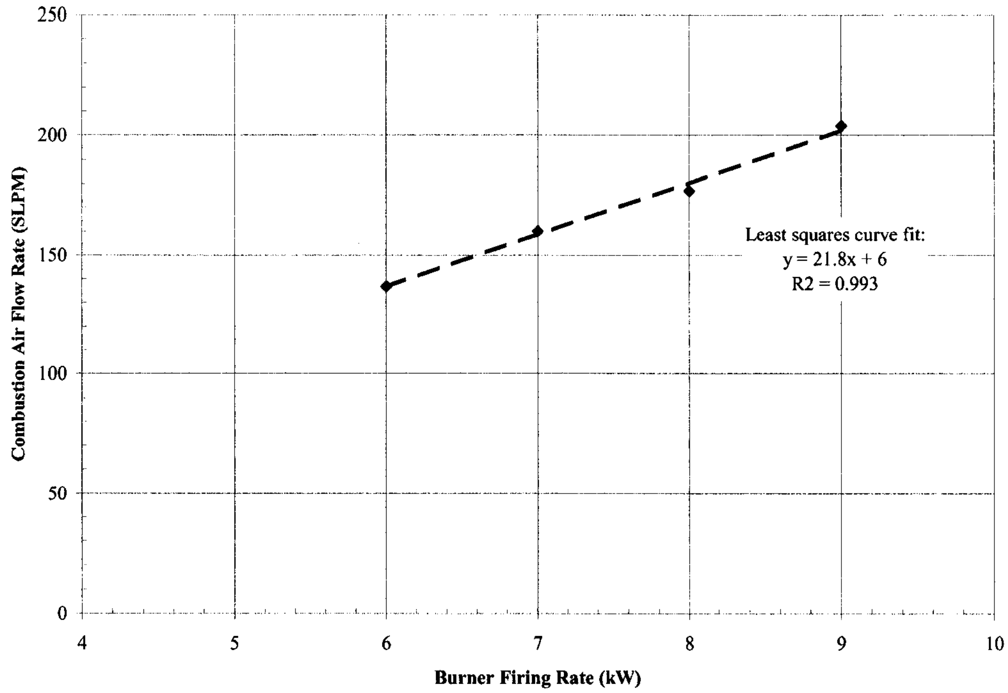

Figure 4-10: Relationship Between Combustion Air Flow Rate and Burner Firing Rate For Optimized Burner Performance

A linear relationship was also found to exist between exhaust gas temperature and burner firing rate, as shown in Fig. 4-11. This result details the decreased effectiveness of the burner's internal recuperator as firing rate is increased. This is also shown by the values for gross combustion efficiency, provided by the combustion analyzer, decreasing with increasing burner firing rate, as shown in Fig. 4-12. The gross combustion efficiency values provided by the combustion analyzer use the gross calorific value of the fuel and consider the latent heat of vaporization of the water vapour in the exhaust to be a loss. High exhaust temperatures and the decreasing combustion efficiency at higher firing rates are indications that a secondary recuperator would benefit this system.

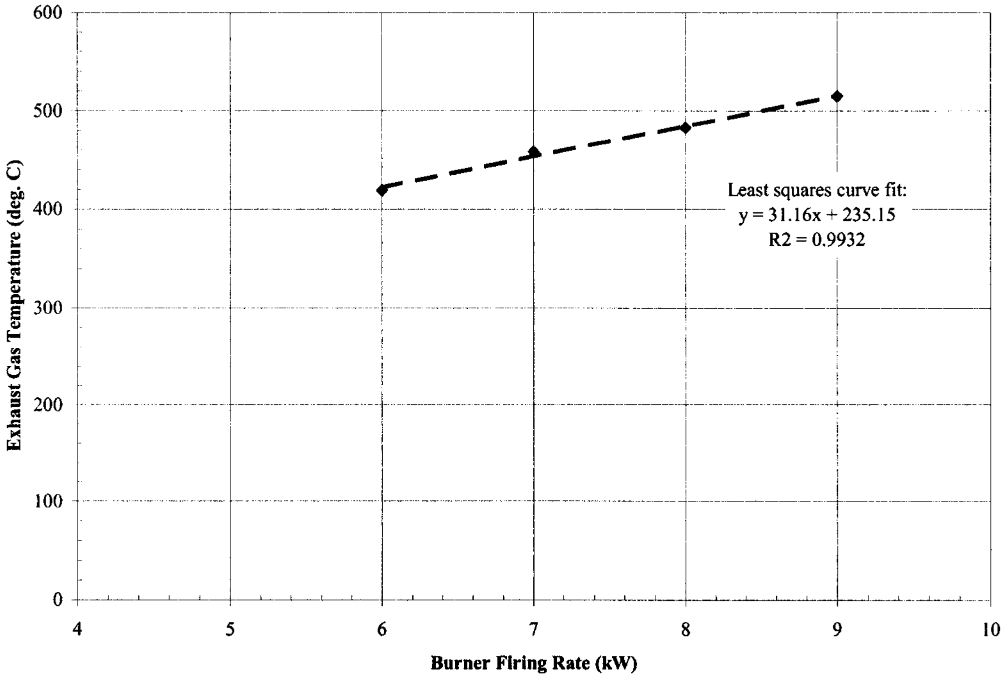

Figure 4-11: Exhaust Gas Temperature during Optimized Burner Combustion

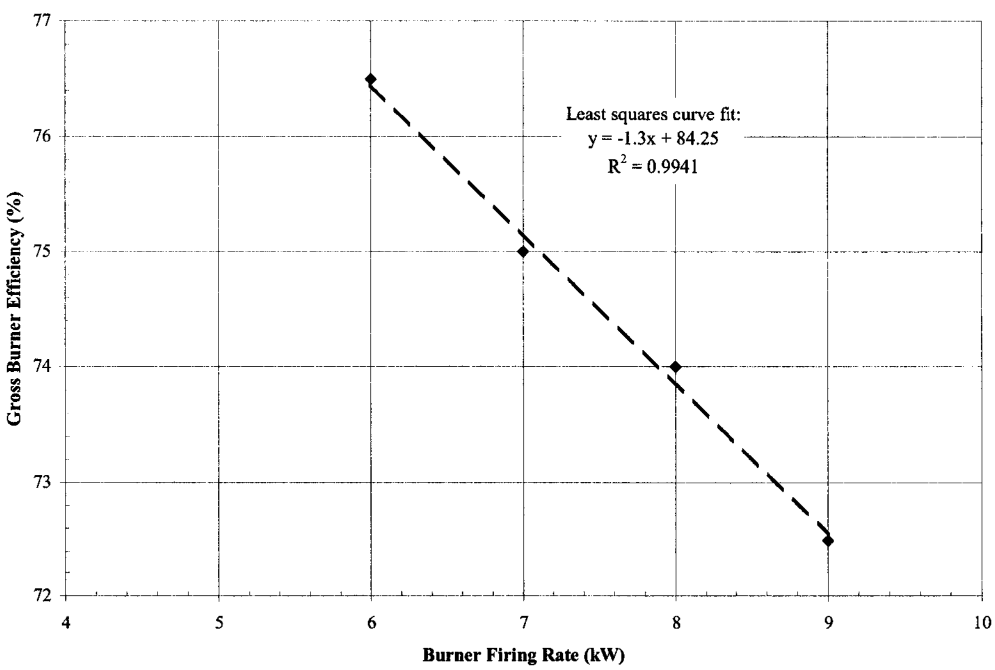

Figure 4-12: Gross Combustion Efficiency during Optimized Burner Operation

4.7 Full Size (72-Cell) Circuit Results

4.7.1 Voltage and Current Response of 72-Cell Circuits

Voltage and current measurements were gathered for all eight 72-cell circuits during optimized burner operation. A Chroma 63103 Load Module installed in a Chroma 6314 Mainframe (both manufactured by Chroma ATE Inc., Taipei Hsien, Taiwan) was used to measure the voltage and current output of the circuits. Loads of constant resistance were applied to the circuits, and the resulting voltage and current values observed. V_{oc} values were recorded in absence of a load placed across the cells, and I_{sc} readings were provided using a short circuit function built into the load module.

Figures 4-13 and 4-14 detail a current versus voltage (IV) curve and a power versus voltage curve respectively for a firing rate of 6kW. The shapes of these curves are typical for all tested firing rates (6kW to 9kW). The comparative performance of the circuits is also typical, with circuits 3 and 5 constantly performing below average, and circuit 2 constantly performing above average. Appendix F contains current versus voltage and power versus voltage curves for all eight circuits at burner firing rates from 7-9kW.

The response of circuit #1 to varied burner firing rates is exhibited in Fig 4-15 and Fig. 4-16. Circuit #1 was chosen to be representative for the eight circuits due to its average performance throughout testing. As can be seen, current and power production at any one voltage increase as burner firing-rate is increased, but the overall shape of the curves is maintained.

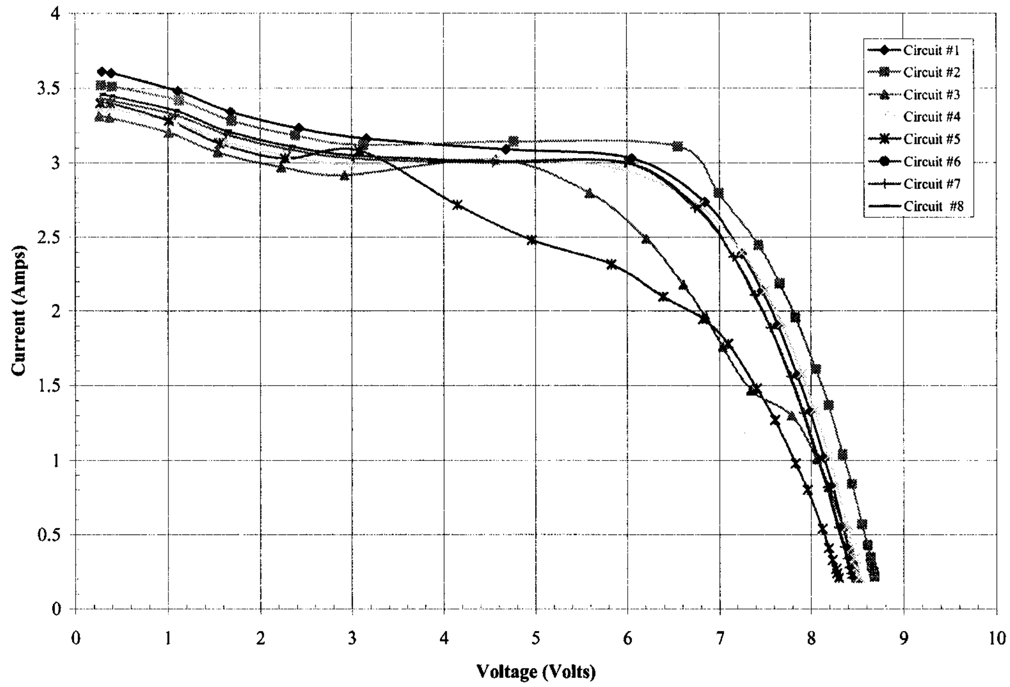

Figure 4-13: Typical Current versus Voltage Curve for 6kW Burner Operation

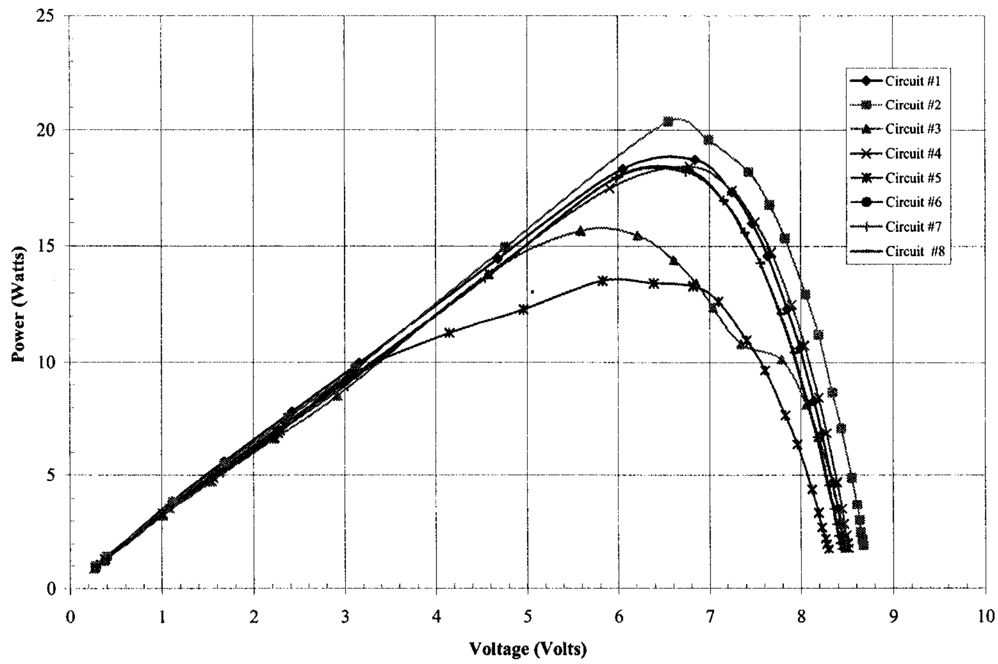

Figure 4-14: Typical Power versus Voltage Curve for 6kW Burner Operation

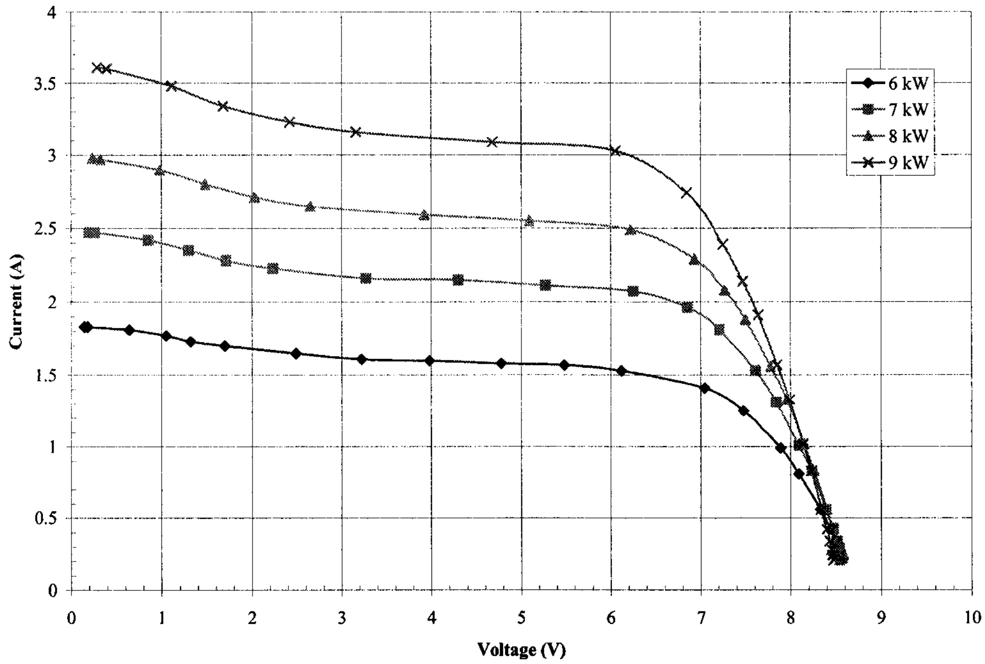

Figure 4-15: Current Response of Circuit #1 under Varied Burner Firing Rates

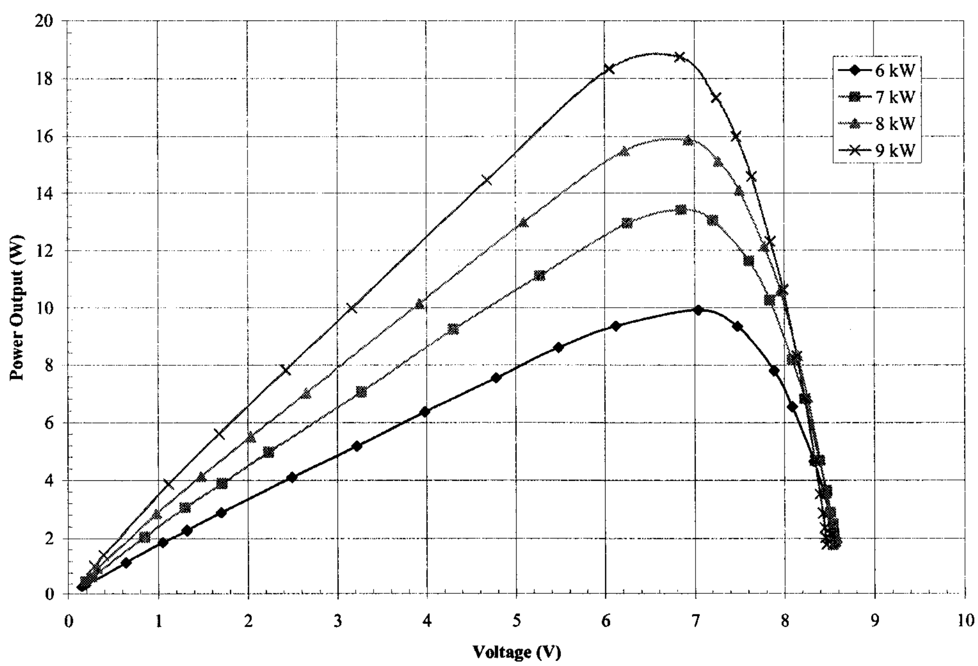

Figure 4-16: Power Response of Circuit #1 under Varied Burner Firing Rates

The maximum power point (P_{max}) for circuit #1 can be found for each firing rate from Fig. 4-16. The resulting values for V_{max} decrease slightly with increasing firing rate and vary between approximately 7.5V at 9kW to 7.0V at 6kW. By superimposing these results on the IV curve for circuit #1 (Fig. 4-15), the I_{max} values for are found to range from 2.9A at 9kW to 1.4A at 6kW.

The average circuit output at the maximum power point, (P_{avg}) was found at each firing rate. This was done by determining a voltage value on the power versus voltage curve that was representative of the average V_{max} value for all eight circuits. The individual circuit power outputs were then summed and averaged at this V_{max} value. A linearly increasing relationship between P_{avg} and burner firing rate was found, and is given in Fig. 4-17.

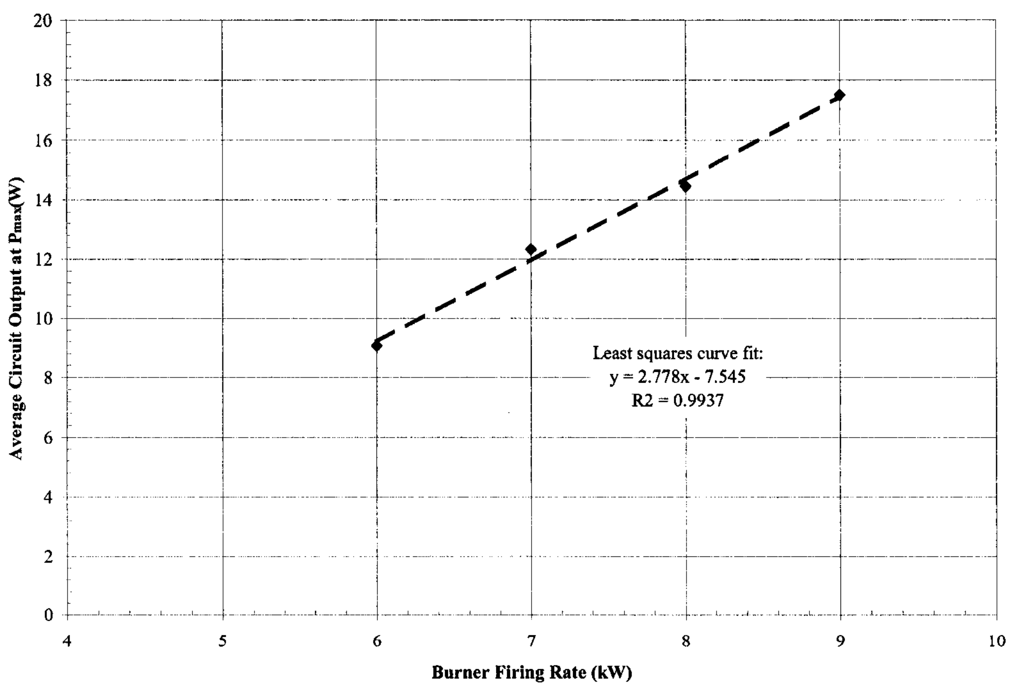

Figure: 4-17: Average Circuit Power Output at P_{max}

4.7.2 Fuel to Electric Conversion Efficiency

The fuel to electric conversion efficiency measures the ability of the system to generate electrical energy. This value incorporates the efficiency of the burner to convert fuel energy to heat, the efficiency of the emitter to convert heat into radiant energy, the efficiency of the spectral filtering components to reflect non-useable wavelengths, and the efficiency of the 72-cell GaSb circuits to convert the useable wavelengths into electricity.

The overall fuel to electric conversion efficiency of this system was defined as:

$$\eta_{fuel-electric} = \frac{P_{electric}}{P_{fuel}} \qquad (4.7)$$

where:

$P_{electric}$ = average optical enclosure power output at a particular firing rate

P_{fuel} = fuel energy rate

The average optical enclosure power output was calculated by multiplying the values for P_{avg} from Fig. 4-17 by eight to account for all eight circuits installed in the optical enclosure. The fuel energy rate was calculated using a lower heating value (LHV) of 46373 KJ/kg for propane at STP, and the mass flow measurements provided by the fuel mass flow controller.

As can be seen in Fig. 4-18, a linear relationship is found between electric conversion efficiency and burner firing rate. This is expected due to the linear increase in average circuit output with firing rate shown in Fig. 4-17.

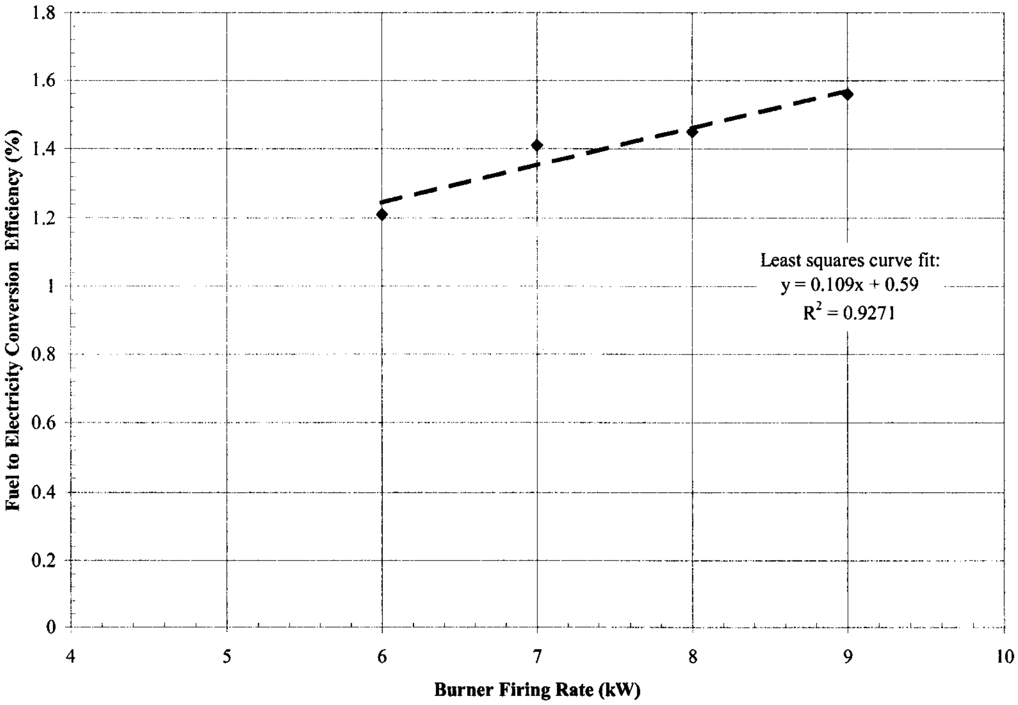

Figure 4-18: Variation of Fuel to Electric Conversion Efficiency with Burner Firing Rate

4.7.3 Array Efficiency of 72-cell GaSb Circuits

The array efficiency compares the amount of electrical energy generated by the eight circuits to the amount of heat energy removed by the optical enclosure cooling system. This is a useful measure of the performance of the spectral filtering components, as well as indicating how efficiently the circuits are converting the radiation reaching the cells to electricity. This efficiency value effectively neglects the inefficiencies introduced into this system by utilizing a burner that is nearly 3 times longer than the optical enclosure.

The array efficiency was calculated using the following formula:

$$\eta_{array} = \frac{P_{electric}}{P_{cool} + P_{electric}} \tag{4.8}$$

where:

$P_{electric}$ = average optical enclosure power output at a particular firing rate

P_{cool} = energy removal rate of optical enclosure cooling system

The value for P_{cool} was found by summing the individual energy removal rates for each cooling channel. The individual energy removal rates for the eight cooling channels were found using equation 4.9:

$$\dot{E}_{water\ out} = \dot{m} \cdot C_p \cdot \Delta T \tag{4.9}$$

where:

$\dot{m}$ = water mass flow rate (kg/s)

C_p = specific heat value for water at constant pressure

ΔT = water temperature difference from inlet to outlet

Water mass flow rates were obtained using a stopwatch and measuring the flow into a graduated container over a period of one minute. The average of the inlet and outlet water temperatures was used to determine the C_p value.

The relationship between array efficiency and burner firing rate is exhibited in Fig. 4-19. From this figure and the one previous, it can be seen that both the overall fuel to electric conversion efficiency and the array efficiency follow linear trends. It is also shown that the slope of array efficiency is over two times that of the fuel to electric conversion efficiency. This is a valid indication that design inefficiencies, including heat lost through the insulated portions of the burner, as well as losses within the burner itself, increase faster than circuit power output, as firing rate is increased.

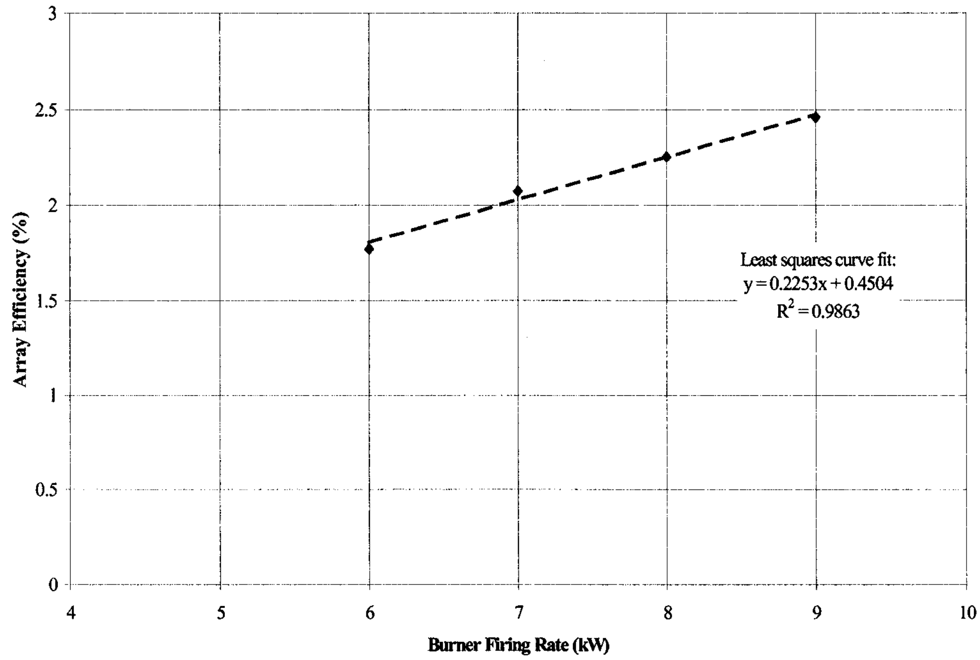

Figure 4-19: Relationship between Array Efficiency and Burner Firing Rate

The P_{avg} values given in Fig. 4-17 were also used to calculate the average power density (ρ_{power}) of the 72-cell GaSb circuits using equation 4.10.

$$\rho_{power} = \frac{P_{avg}}{A_{cell}} \qquad (4.10)$$

where:

A_{cell} = active area of one 72-cell GaSb circuit

The active area of each circuit was 135.02cm^2, resulting in average power densities from 0.07W/cm^2 at 6kW to 0.13W/cm^2 at 9kW. Maximum power density values for this system were obtained from circuit #2, which consistently outperformed all other circuits and achieved power densities ranging from 0.08W/cm^2 at 6kW to 0.15W/cm^2 at a firing rate of 9kW. These power density values are well below the value of 1.5W/cm^2 reported for a TPV system constructed by West and Connelly [6], and highlight the need for increased emitter temperatures. Possible methods to attain increased emitter temperatures in this system include improved spectral control and increased energy recuperation from the burner exhaust gases. The effect of the latter on emitter temperature is discussed in a recent paper by Qiu and Hayden [35]. It is also interesting to note that even these power densities are approximately 10 to 15 times higher than what exists in many solar energy systems.

The fill factor (FF) of photovoltaic cells, a commonly discussed value, is the ratio of the maximum power output to the product of V_{oc} and I_{sc}, as shown in equation 4.11:

$$FF = \frac{V_{\max} \cdot I_{\max}}{V_{oc} \cdot I_{sc}} \tag{4.11}$$

where:

$V_{\max}$ = voltage at maximum power point

$I_{\max}$ = current at maximum power point

V_{oc} = open circuit voltage

I_{sc} = short circuit current

As mentioned earlier in this paper, the fill factor is a measure of the imperfections present in a PV system in the form of shunt and series resistances. Table 4-4 displays values calculated using experimental data and equation 4.11, and averaged across all four firing rates. Fill factor values supplied by JX Crystals Inc. varied from 0.685 to 0.720 and were determined using their flash stand apparatus.

As can be seen, the values obtained in the prototype system are lower than those obtained by the flash stand apparatus at JX Crystals. This is expected since the flash stand is an idealized situation with a very bright (high temperature) emitter and virtually no circuit heating. Circuit heating, which was appreciable in this system, leads to shunt leakage in the cell and decreased efficiency. It can also be seen from the data in Table 4-4 that a correlation exists between poor circuit power production and depressed fill factor values, confirming the ability of fill factor to accentuate inefficiencies in the PV circuit. Circuits 3 and 5, which consistently performed below average, have correspondingly low values for fill factor. Circuit 8 which had performance that varied, depending on firing rate, from average to below average also has a depressed fill factor.

Table 4-4. Average Calculated Fill Factor Values for the 72-Cell Circuits

Circuit Number	Average Fill Factor Value
1	0.618
2	0.655
3	0.562
4	0.637
5	0.508
7	0.635
8	0.557

4.8 System Energy Balance

In order to provide an indication of energy losses within the system, and a comparison of the relative size of these values, an overall mapping of energy flow through the system was performed. The two main losses in this system were flue gas losses and cooling water losses. The combustion gas analyzer measured energy lost through the flue gas, and cooling water energy was calculated using the change in temperature and the flow rate of the cooling water in equation 4.9.These losses are listed in Table 4-5, along with the relative percentage of the input energy they represent.

Table 4-5: TPV system losses

Firing Rate (kW)	Flue gas loss (kW)	Cooling water loss (kW)	Flue gas loss (%)	Cooling water loss (%)	Total accounted losses (%)
6	1.41	4.02	23.50	67.03	90.53
7	1.75	4.65	25.00	66.46	91.46
8	2.08	5.02	26.00	62.75	88.75
9	2.48	5.55	27.50	61.68	89.18

As can be seen from Table 4-5, the proportion of overall losses due to cooling water decreases with firing rate, while the percentage of overall losses due to exhaust gases increases with firing rate. These trends indicate two things about this system. The increase in flue gas losses with firing rate indicates that burner recuperation efficiency decreases with firing rate as discussed in section 4.6. The decrease in cooling water losses with firing rate can be explained by the shift in Plank's spectral distribution of emissive power with increasing temperature [23]. As burner firing rate and emitter temperature rise, the peak of this emissive power curve shifts towards shorter wavelengths, as given by Wien's displacement law:

$$\lambda_{\max} \cdot T = 2897.756 \ \mu m \cdot K \tag{4.12}$$

where:

$\lambda_{\max}$ = wavelength of maximum emissive power for a given temperature

T = emission temperature

As can be seen from equation 4.12, with the right hand side of the equation constant an increase in emission temperature results in λ_{max} decreasing, and therefore the maximum emissive power occurring at shorter wavelengths.

Since the spectral filtering components used in this system are more effective at controlling shorter emission wavelengths (from approximately 2-4μm), cooling water losses decrease as more energy is radiated in this waveband. This result highlights the need for increased long wavelength spectral control in this system.

It can be seen in Table 4-5 that the exhaust and cooling water losses account for between 88.75% and 91.46% of the total input energy, depending on firing rate. In an attempt to account for the remaining input energy, an evaluation of the energy lost through natural convective heat transfer on the hot outer surfaces of the system was performed.

Temperature measurements used in the natural convection analysis were obtained during a firing rate of 9kW using a non-contact thermocouple manufactured by Omega Inc.

(model OS-88000-K-1200) in conjunction with an Omega multi-meter (model HHM 16). Heat lost from the outer surfaces of the upper and lower insulated sections (detailed in Fig. 3-1), as well as from the upper surface of the table used to support the burner apparatus were calculated. The upper insulated section in Fig. 3-1, referred to as the upper burner enclosure in this analysis, was necessary due to the burner length being longer than required. The lower insulation piece in Fig. 3-1, or lower burner enclosure, insulated the burner tube end in order to prevent excessive energy losses. These two insulated areas, along with the supporting table, represent nearly all the hot surfaces present during system operation.

The result of this analysis is a calculated natural convection loss of approximately 630W at a firing rate of 9kW. This represents approximately 7% of the energy input rate, and when added to the exhaust and cooling water losses, accounts for 96% of the input energy. The details of the natural convection calculations are provided in Appendix G.

5. CONCLUSIONS AND SUMMARY

5.1 Review of Problem and Objectives

Grid independent power is desirable for industrial applications including secluded oil and gas well sites, telecommunications towers, off-shore platforms, and various military roles. Obtaining power from the electrical grid is generally not a valid option in these situations. Thermophotovoltaics could satisfy these needs by providing a power source capable of providing high-density power without the need for a storage device at any time of day, in any weather condition. Lack of moving parts in these systems should lead to quiet operation and low maintenance requirements.

Residential applications of this technology include backup or self-powered systems to decrease dependence on the sometimes-erratic power grid. Since in many situations the supply of gas is not affected by power outages, a central heating unit powered by thermophotovoltaics could continue to provide heat and possibly electrical power in the event of a power outage. Using thermophotovoltaics as a distributed power source for homes would also decrease line losses resulting from transporting electricity over long distances via the grid.

Thermophotovoltaic technology could also be applied to mitigate pollution problems caused by the widespread use of internal combustion engines for personal and commercial transport. In a role of reduced capacity, thermophotovoltaics could also be integrated into vehicles not as a locomotion source but to provide auxiliary power to recreational vehicles, refrigeration units and other power-intensive systems.

In order to investigate the feasibility of incorporating thermophotovoltaic technology into commercial applications, an increased knowledge base concerning system design, and TPV component interaction was needed. The goal of this study was to design, construct and test a prototype TPV unit in order to gain the experience that is needed for TPV technology to be successfully introduced into the commercial marketplace.

5.2 Conclusions / Summary of Experimental Results

A prototype thermophotovoltaic unit has been designed, constructed and tested at the Alberta Research Council in Edmonton, Alberta. The major findings of this research include system dependence on emitter temperature and cooling load data during single GaSb cell testing, burner performance characterization and optimization, as well as performance data from 72-cell GaSb circuits that led to calculations of array efficiency and overall system efficiency.

The first step in this investigation used single cell GaSb units in order to minimize the risk of damaging the full size, 72-cell GaSb circuits. Short circuit current production was found to have a power-type dependence on emitter temperature, highlighting the requirement of increased emitter temperatures to enhance system efficiency. The maximum cooling load during single cell tests was $6.34kW_{th}$, resulting in cooling water exit temperatures between 21°C and 35°C, depending on water flow rate.

The investigation of burner performance through the use of a combustion gas analyzer provided unexpected results. In order to achieve efficient burner operation, airflow rates 30-35% higher than expected were required. Flow rates lower than this resulted in excessive CO production and a high probability of hydrocarbons escaping in the exhaust. The increased airflow requirement of the burner may be due to a portion of the combustion air, used as cooling air for some internal burner components, not being efficiently mixed with the fuel before combustion.

Data from the 72-cell circuits were gathered at burner firing rates ranging from 6kW to 9kW. Average circuit output was found to increase linearly from 9.1W to 17.5W as the firing rate was increased from 6kW to 9kW. This resulted in power densities ranging from $0.07W/cm^2$ at 6kW to $0.13W/cm^2$ at 9kW. Fuel to electric conversion efficiency also followed a linear curve from 1.2% at 6kW to 1.5% at 9kW. Similarly, array efficiency increased linearly from 1.8% at 6kW to 2.5% at 9kW.

5.3 Sensitivity Analysis

By varying different system parameters during testing, a picture of system sensitivity to different variables was formed. System performance was most sensitive to emitter temperature, and a power-type correlation resulted in a nearly 400% increase in I_{sc} output for an emitter temperature increase from 800°C to 1000°C. System performance was also shown to be quite sensitive to the load applied to the GaSb circuits, with power production increasing 10 to 20 times (depending on firing rate) as the load was varied from 0.05Ω to 5Ω. Although from this analysis load may seem to have a bigger effect on cell performance than temperature, temperature is considered to be a more vital parameter since emitter temperatures below 800°C result in virtually no current production in the cells.

Spectral filtering is judged to be the parameter with the third highest system sensitivity. Removing both the quartz and nine layer dielectric filters from the single cell test case resulted in an 88% reduction in I_{sc} output. Removal of individual spectral filtering components during single cell operation resulted in I_{sc} reductions of 76% and 33% for the dielectric filters and quartz respectively.

Performance of the prototype TPV system was shown to be least sensitive to burner efficiency, integrated recuperator performance and firing rate. This was exhibited by the gross burner efficiency decreasing by only 4% as firing rate was varied from 6kW to 9kW. Exhaust temperatures increased by 100°C over this firing range.

5.4 Recommendations for Future Work

Recommendations and points of contention have been highlighted throughout this paper, and are gathered in this section to provide an overall view of the necessary steps needed to bring this technology closer to the commercial marketplace.

5.4.1 Burner Improvements

The operation of the radiant tube burner manufactured by WS Thermal Process Technology Inc. needs to be further investigated. This research would potentially pave the way for burner modifications that would increase system efficiency. These modifications would include reducing the length of the burner to reduce the input energy requirements as well as the overall system dimensions. Shortening the burner should also reduce the differential pressure requirements on the combustion air and allow the use of a smaller, more efficient combustion air blower. Burner modifications in order to reduce emitter temperature gradients are also necessary to increase system performance. This might be accomplished by the insertion of an alumina plug into the end of the outer burner tube, as mentioned in section 4.3.1.

Another method that may be used to decrease heat transfer to the end of the outer burner tube and minimize the emitter temperature gradient would be to redesign the inner burner tube. By narrowing this inner cylinder as it approaches the end of the outer tube, the surface area radiating outward toward the outer cylinder would decrease, decreasing heat transferred to the outer cylinder. Narrowing the inner cylinder would also increase the gap between the inner and outer cylinders, further decreasing heat transfer by reducing the local gas velocity and therefore the local convective heat transfer coefficient.

Increased recuperation is also required for this unit, as evidenced by the exhaust gases leaving the system at temperatures ranging from 420-520°C. This represents approximately 25% of the energy input to the system. At these relatively low temperatures a material such as stainless steel could be used to fabricate the recuperator, at a significant cost savings over ceramic components. This would be one of the easiest ways to increase the performance of this system, and is highlighted by Qui and Hayden [35] as an important step to higher emitter temperatures.

5.4.2 Spectral Control

Enhancing spectral control results in increased thermophotovoltaic system efficiency by increasing emitter temperatures and placing a larger portion of the emitted energy within wavelengths useable by the TPV cells. Reducing off-band emission also improves the efficiency of the TPV cells by decreasing cell temperatures. Spectral control could be enhanced in this system through the use of more sophisticated filtering techniques as well as utilizing selective or matched emitters.

Components with enhanced spectral control ability include more complicated dielectric filters employing additional layers in order to broaden the range of wavelengths reflected back to the emitter. Spectral filters using sub-micron elements similar to those patented by EDTEK may also have a beneficial effect on system efficiency.

The use of selective or matched emitters reduces the difficulty of controlling or recycling non-useable wavelengths by decreasing these emissions altogether. Materials such as tungsten, and Ni or Co-doped MgO hold promise for decreasing off-band emissions and increasing emitter temperatures. Further research on incorporating these materials into this prototype is warranted.

5.4.3 System Modeling

Detailed modeling of the optical enclosure of this unit would provide an increased understanding of geometrical and spectral filtering effects on system efficiency. By validating the model with results from this paper, different optical enclosure configurations could be simulated and their efficiency predicted without having physically test each modification. Such a design tool would be pivotal to the introduction of thermophotovoltaics to the commercial marketplace.

In the interim until a model is constructed and validated, design calculations similar to those outlined in Appendix A can be used to advance and improve upon the prototype design detailed in this work by incorporating the changes recommended in Section 5.4.

REFERENCES

1. "Thousands of homes still in the dark after Canadian ice storm" cnews, Feb. 2, 1998: n. pag. On-line. Internet. 7 Nov. 2003. Available: http://www.canoe.ca/CNEWSIceStorm/feb2_rnd.html.
2. Botelho G. "Power returns to most areas hit by blackout" CNN.com International Aug. 16, 2003: n. pag. On-line. Internet. 7 Nov. 2003. Available: http://edition.cnn.com/2003/US/08/15/power.outage/index.html.
3. Licciulli A., et al., "The challenge of high-performance selective emitters for thermophotovoltaic applications" Semiconductor Science and Technology **18** (2003):S174-S183.
4. Baldasaro P., et al. "Thermodynamic analysis of thermophotovoltaic efficiency and power density tradeoffs" Journal of Applied Physics 89.6 (2001): 3319-27.
5. Coutts, T. J., "Overview of thermophotovoltaic generation of electricity" Solar Energy Materials and Solar Cells **66** (2001): 443-452.
6. West, E.M.; Connelly, W.R., "Integrated development and testing of multi-kilowatt TPV generator systems" AIP Conference Proceedings Title: AIP Conf. Proc. (USA) no.460 p.446-56.
7. Fraas, L., Avery, J., Malfa, E., Wuenning, J. G., Kovacik, G., Astle, C., 2002, "Thermophotovoltaics for Combined Heat and Power Using Low NOx Gas Fired Radiant Tube Burners" Fifth Conference on Thermophotovoltaic Generation of Electricity, September 15-19, 2002, Rome, Italy.
8. Fraas, L. M., Huang, H.X., 2003, "Thermophotovoltaic furnace-generator for the home using low bandgap GaSb cells" Semicond. Sci. Technol. **18** pp S247-S253.
9. Morrison O. et al. "Use of a Thermophotovoltaic Generator in a Hybrid Electric Vehicle" Thermophotovoltaic Generation of Electricity: Fourth NREL Conference Denver, CO, 1998. Woodbury, New York: AIP Conference Proceedings 460, pp. 488-96.
10. Schock A., Or C., Kumar V. "Small Radioisotope Thermophotovoltaic (RTPV) Generators" The Second NREL Conference on Thermophotovoltaic Generation of Electricity, Colorado Springs, CO, 1995. Woodbury, New York: AIP Conference Proceedings 358.

11. Broman L. et al. "Electricity from Wood Powder Report on a TPV Generator in Progress" The Second NREL Conference on Thermophotovoltaic Generation of Electricity, Colorado Springs, CO, 1995. Woodbury, New York: AIP Conference Proceedings 358.

12. Coutts, T.J., "Thermophotovoltaic Principals, Potential, and Problems"; 1st NREL Conference on Future Generation PV Technologies, Denver, CO. AIP Conference Proceedings 404; Ed By R.D.McConnell p.220, 1997.

13. Kolm, H., H., 1956 "Solar-battery power source" Quarterly Progress Report, Solid State Research, Group 35 (Lexington, MA:MIT Lincoln Laboratory) p.13.

14. Broman L. 1995, "Thermophotovoltaics bibliography" Prog. Photovolt., Res. Appl. **3** 65-74.

15. Chen K. C., Osborn D., et al, 1999, "Small Efficient Power Supply" U.S. Army Research Office, Contract No. DAAG55-97-C-003.

16. Guazzoni G. 1972 "High temperature spectral emittance of oxides of erbium samarium, neodymium and ytterbium" Appl. Spectrosc. **26** 60-5.

17. Würfel P., Ruppel W., 1980, "Upper limit of thermophotovoltaic solar energy conversion" IEEE Trans. Electron Devices **27** pp 190-5.

18. Demichelis F., Minetti-Mezzetti E., 1979, "A solar thermophotovoltaic converter" Solar Cells **1** 395-403.

19. Nelson R. E., "A Brief history of thermophotovoltaic development" Semicond. Sci. Technol. **18** (2003) S141-S143.

20. Iles P., "Photovoltaic Principals Used in Thermophotovoltaic Generators" The First NREL Conference on Thermophotovoltaic Genèration of Electricity, Copper Mountain, CO, 1994. New York: AIP Conference Proceedings 321. pp. 67-79.

21. Fraas L., et al. "TPV Generators Using The Radiant Tube Burner Configuration" JX Crystals Inc. (2001) , On-line. Internet. Available: http://www.jxcrystals.com/tech_articles.htm.

22. Buresch, Matthew. Photovoltaic Energy Systems. New York: McGraw-Hill, 1983.

23. Siegel R., Howell J.R., Thermal Radiation Heat Transfer 3rd Ed., Philadelphia, Pa,: Taylor and Francis Ltd, 1992.

24. DeBellis, C.L., Scotto, M.V., Scoles, S.W., Fraas, L., "Conceptual Design of 500W Portable Thermophotovoltaic Power Supply Using JP-8 Fuel" Thermophotovoltaic Generation of Electricity Third NREL Conference, Colorado Springs, CO, 1997. Woodbury, New York: AIP Conference Proceedings 401 pp.355-67.

25. Ferguson L., Fraas L., "Matched Infrared Emitters for Use with GaSb Cells" Thermophotovoltaic Generation of Electricity Third NREL Conference, Colorado Springs, CO, 1997. Woodbury, New York: AIP Conference Proceedings 401 pp.169-170.

26. Crowley C. J., Elkouh N. A., Magari P. J., "Thermal Spray Approach for TPV Emitters" Thermophotovoltaic Generation of Electricity: Fourth NREL Conference Denver, CO, 1998. Woodbury, New York: AIP Conference Proceedings 460 pp.197-213.

27. Ferber J., Aschaber J., et al. "Microstructured Tungsten as Selective Emitters in Thermophotovoltaic Systems" 16th European Photovoltaic Solar Energy Conference and Exhibition, Glasgow 2000.

28. Fraas L. M., 1999, "Small Efficient Thermophotovoltaic Power Supply Using Infrared-Sensitive Gallium Antimonide Cells" Army STTR Phase II Final Report, U.S. Army Research Office, Contract No. DAAG55-97-C-0002.

29. Ferguson, L.G. and Dogan, F., "A highly efficient NiO-Doped matched emitter for thermophotovoltaic energy conversion", Journal of Materials Science and Engineering **B83** (2001) p.38.

30. Les J., et al. "Interference Filters for Thermophotovoltaic Applications" Mathematical Problems in Industry, Delaware, June, 1999.

31. Butcher T., Krishna C., Horne W., Morgan M., Sundaram V. 1999 Proc. Ccombustion Canada '99 Conf. (May, 1999).

32. Durisch W. et al. "Interfacing a Small Thermophotovoltaic Generator to the Grid" Thermophotovoltaic Generation of Electricity: Fourth NREL Conference Denver, CO, 1998. Woodbury, New York: AIP Conference Proceedings 460 pp.403-14.

33. Horne W.E., Morgan M.D., Sundaram V.S., "IR Filters for TPV Convertor Modules" The Second NREL Conference on Thermophotovoltaic Generation of

Electricity, Colarado Springs, CO, 1995. Woodbury, New York: AIP Conference Proceedings 358 pp 35-51.

34. Pierce D.E., Guazzoni G., "High Temperature Optical Properties of Thermophotovoltaic Emitter Components" Thermophotovoltaic Generation of Electricity: Fourth NREL Conference Denver, CO, 1998. Woodbury, New York: AIP Conference Proceedings 460. pp.177-90.

35. Qui K., Hayden A.C.S., "Electric power generation in home furnaces using thermophotovoltaic cells" Combustion Canada '03 Conference, Vancouver, BC, 2003.

36. Wuenning J. A., Wuenning J. G. " Ceramic burner and radiant tubes for high-temperature processes" Tile Brick Int. **12** (1996) pp 438-41.

37. IR Transmission Chart, Optical Properties. GE Quartz Worldwide. On-line. Internet. 24 Oct. 2003. Available: http://www.gequartz.com/en/optical.htm

38. Fraas L.M., et al. "Low cost High Power GaSb Photovoltaic Cells" Thermophotovoltaic Generation of Electricity Third NREL Conference, Colorado Springs, CO, 1997. Woodbury, New York: AIP Conference Proceedings 401.

Appendix A

Preliminary Design Calculations

APPROXIMATE SPECTRAL POWER ANALYSIS

ASSUMED EMITTER TEMPERATURE → 1100°C (1373K)

TOTAL BLACKBODY POWER $= E_b = \sigma T^4$

$= (5.67 \times 10^{-8}\ W/m^2k^4)\ (1373K)^4$

$= 20.15 \times 10^4\ W/m^2$

$= 20.15\ W/cm^2$

Now, find the distribution of this total energy in 3 bands:

- $\lambda < 1.8\ \mu m$ -cell useable energy

- $1.8\mu m < \lambda < 3.6\mu m$ - energy to be recycled by mid-wavelength filters at an efficiency of 90%

- $\lambda > 3.6\mu m$ - long wavelength radiation, to be partially filtered by two layers of type 214 quartz

Using Blackbody Function table (pg 971, Thermal Radiation Heat Transfer, Siegel R., Howell J.R., Philadelphia Pa., Taylor and Francis Ltd.):

for $\lambda < 1.8\mu m$ → $\lambda T = (1.8\mu m)(1373K) = 2471\mu mK$.

$\therefore F_{o-2471\mu mk} = 0.155162$

$\therefore E_{b_{\lambda<1.8\mu m}} = (20.15W/cm^2)(0.155162) = 3.127W/cm^2$

for $1.8\mu m < \lambda < 3.6\mu m$: → $\lambda T = (3.6\mu m)(1373K)$

$\lambda T = 4943\mu mK$.

$\therefore F_{o-4943\mu mK} = 0.6264628$

$\therefore F_{2471\mu mK - 4943\mu mK} = 0.6264628 - 0.155162 = 0.4713.$

$E_{b_{1.8\mu m<\lambda<3.6\mu m}} = (20.15\ W/cm^2)(0.4713) = 9.50\ W/cm^2$

Now, if the spectral control in this waveband is assumed to be 90%, this leaves 10% or 0.95 w/cm^2 as the uncontrolled, or waste energy contribution from this interval.

for $\lambda > 3.6\mu m$:

The remaining energy is found by:

$20.15\ W/cm^2 - 3.127\ W/cm^2 - 9.50\ W/cm^2 = 7.53\ W/cm^2$

Now, if it is assumed that two layers of type 214 quartz are used to suppress losses in this waveband, and as heat shields reduce transmission by $\frac{1}{N+1}$ (page 374 Siegel and Howell) where N = number of layers $\therefore$ transmitted energy is $(7.53W/cm^2)\ (7.53W/cm^2)(1/3) = 2.51W/cm^2$

$$\therefore \text{Spectral Efficiency} = \frac{\text{transmitted useable energy}}{\text{total transmitted energy}}$$

$$= \frac{3.127W/cm^2}{3.127W/cm^2 + 0.95W/cm^2 + 2.51W/cm^2}$$

$$\text{spectral efficiency} = 0.475 \cdot 100 = 47.5\%$$

$$\text{for an emmitter temp} = 1373K$$

If a combustion efficiency of 75% is assumed, as well as a GaSb circuit efficiency of 10%, an overall fuel-electric conversion efficiency can be approximated:

Fuel-Electric Conversion Efficiency = (0.75)(0.10)(0.475)

Fuel Electric Conversion Efficiency = $0.036 \cdot 100 = 3.6\%$

for an emitter temp = 1373K

ASSUME EMITTER TEMPERATURE = 1000°C (1273K)

TOTAL BLACKBODY POWER $= E_b = \sigma T^4$

$= (5.67 \times 10^{-8} W/m^2K^4)(1273K)$

$E_{b1000°C} = 148900.7 W/m^2 = 14.89 W/cm^2$

Now, using similar steps as in the last case,

<u>for λ<1.8μm:</u> $\rightarrow \lambda T = 2291 \mu mK$

$F_{0-2291\mu mK} = 0.1182696$

$E_{b_{\lambda<1.8\mu m}} = (0.1182696)(14.89 W/cm^2) = 1.76 W/cm^2$

<u>for 1.8μm < λ < 3.6μm</u> $\rightarrow \lambda T = 4582.8 \mu mK$

$F_{2291\mu mK - 4582.8\mu mK} = 0.45845136$

$E_{b_{1.8\mu m<\lambda<3.6\mu m}} = 6.826 W/cm^2$

Now, assuming 90% of this energy is recycled by spectral filtering, this leaves <u>$0.6826^{W}/cm^2$</u> as the waste energy contribution from this waveband for $\lambda > 3.6\mu m$:

$$= 2.10 W/cm^2$$

$$\text{Predicted Spectral Efficiency} = \frac{\text{transmitted useable energy}}{\text{total transmitted energy}}$$

$$= \frac{1.76 W/cm^2}{1.76 W/cm^2 + 0.6826 W/cm^2 + 2.10 W/cm^2}$$

$$\text{Predicted Spectral Efficiency} = 0.387 \cdot 100 = 38.7\%$$

@1000°C emitter temp

$$E_{b_{\lambda > 3.6\mu m}} = 14.89 W/cm^2 - 1.76 W/cm^2 - 6.826 W/cm^2 = 6.304 W/cm^2$$

assume 2 layers of type 214 quartz are used, reducing

the transmitted energy to $(1/3)(6.304 W/cm^2) = 2.10 W/cm^2$

$$\text{Predicted Fuel-Electric Conversion Efficiency} = \underbrace{(0.75)}_{\text{Combustion efficiency}}\ \underbrace{(0.10)}_{\text{Circuit efficiency}}\ (0.387)$$

$$\text{Predicted Fuel-Electric Conversion Efficiency} = 0.029 \cdot 100$$

$$= 2.9\%$$

@ 1000°C emitter temp

Appendix B

Quartz Filter Drawing

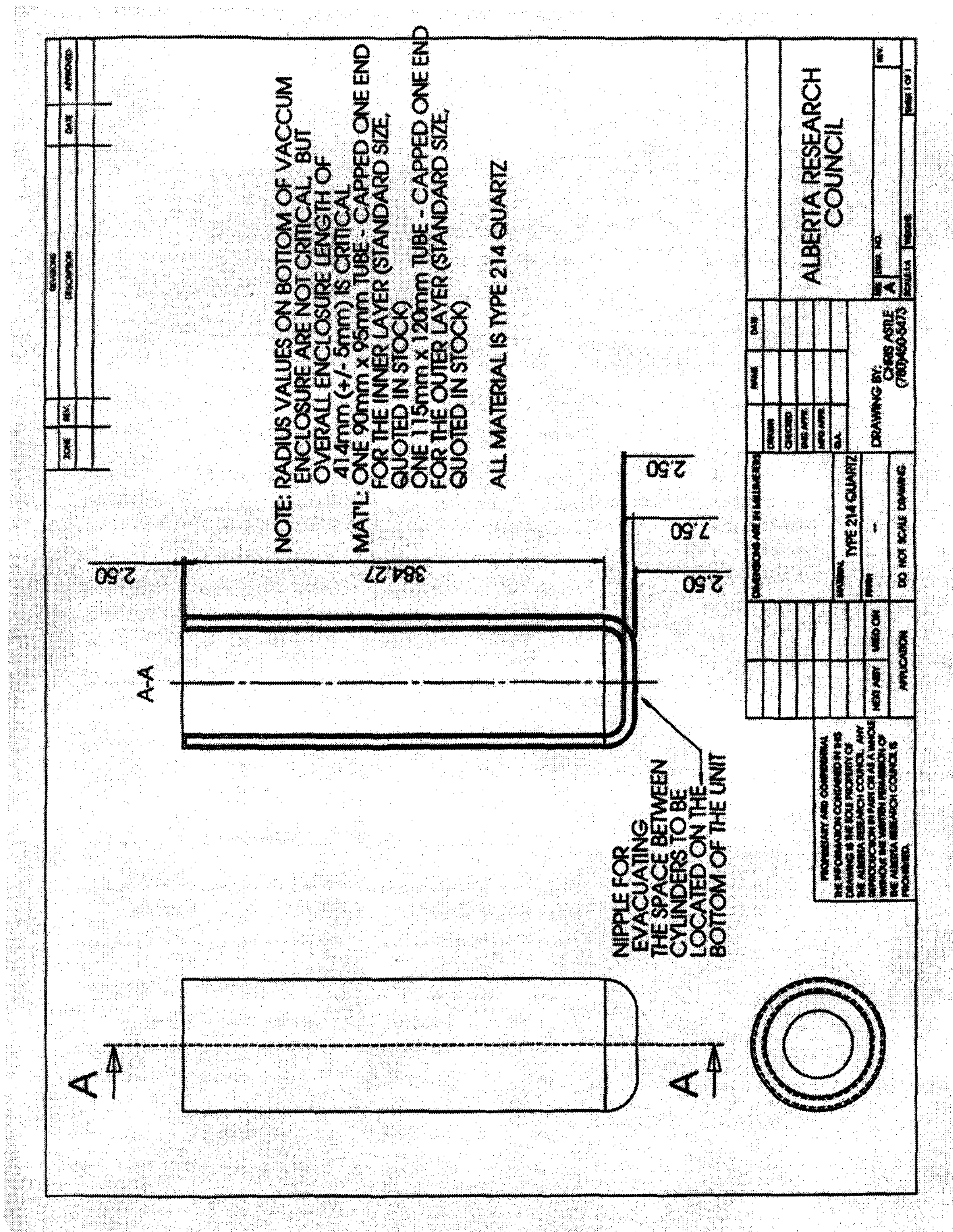
NOTE: RADIUS VALUES ON BOTTOM OF VACCUM ENCLOSURE ARE NOT CRITICAL, BUT OVERALL ENCLOSURE LENGTH OF 414mm (+/- 5mm) IS CRITICAL
MAT'L: ONE 90mm x 95mm TUBE - CAPPED ONE END FOR THE INNER LAYER (STANDARD SIZE, QUOTED IN STOCK)
ONE 115mm x 120mm TUBE - CAPPED ONE END FOR THE OUTER LAYER (STANDARD SIZE, QUOTED IN STOCK)
ALL MATERIAL IS TYPE 214 QUARTZ
NIPPLE FOR EVACUATING THE SPACE BETWEEN CYLINDERS TO BE LOCATED ON THE BOTTOM OF THE UNIT
A-A
A
A
2.50
384.27
2.50
7.50
2.50
DIMENSIONS ARE IN MILLIMETERS
TYPE 214 QUARTZ
DO NOT SCALE DRAWING
DRAWING BY: CHRIS ASTLE (780)450-5473
ALBERTA RESEARCH COUNCIL

Appendix C

GaSb Cell Detail Drawings

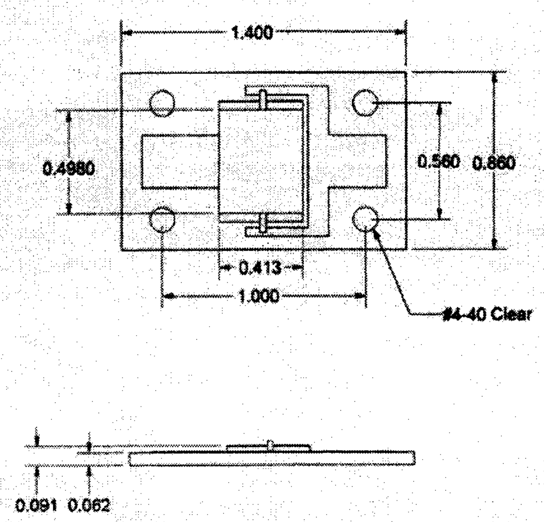

Single GaSb Test Cell Schematic (dimensions in inches)

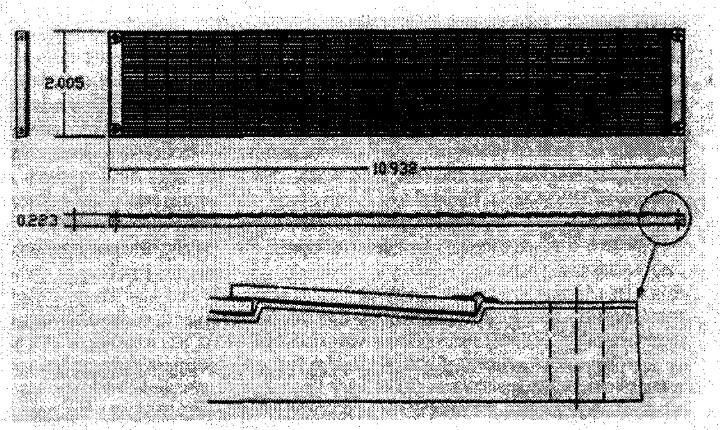

72 Cell GaSb Circuit Schematic (dimensions in inches)

Appendix D

72-Cell GaSb Circuit Specification Curves

JX Crystals' shipment to Alberta Research Council on 4/1/02
(PO# 30988 – two 72 cell GaSb circuits)
JXC contact: Lewis Fraas, 425-392-5237

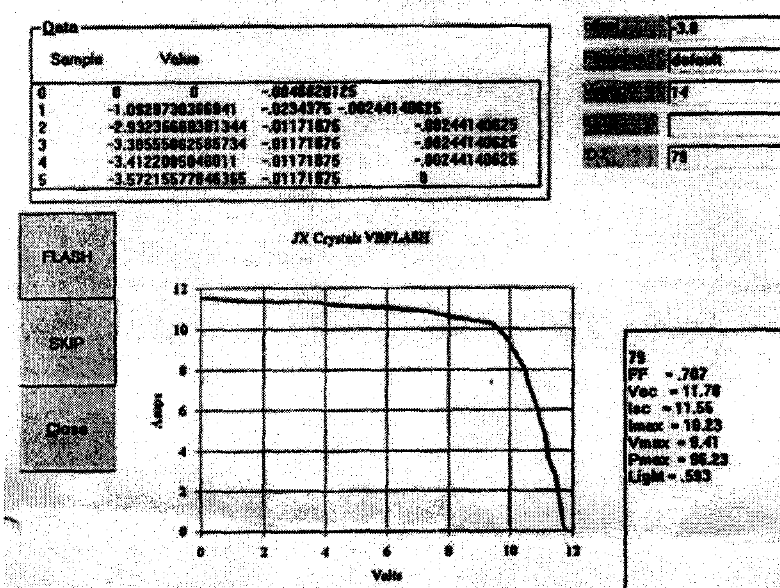

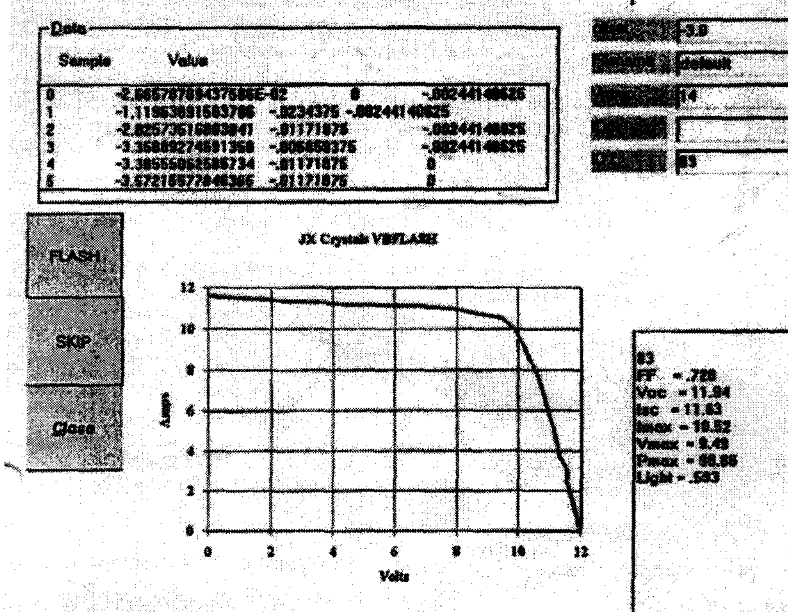

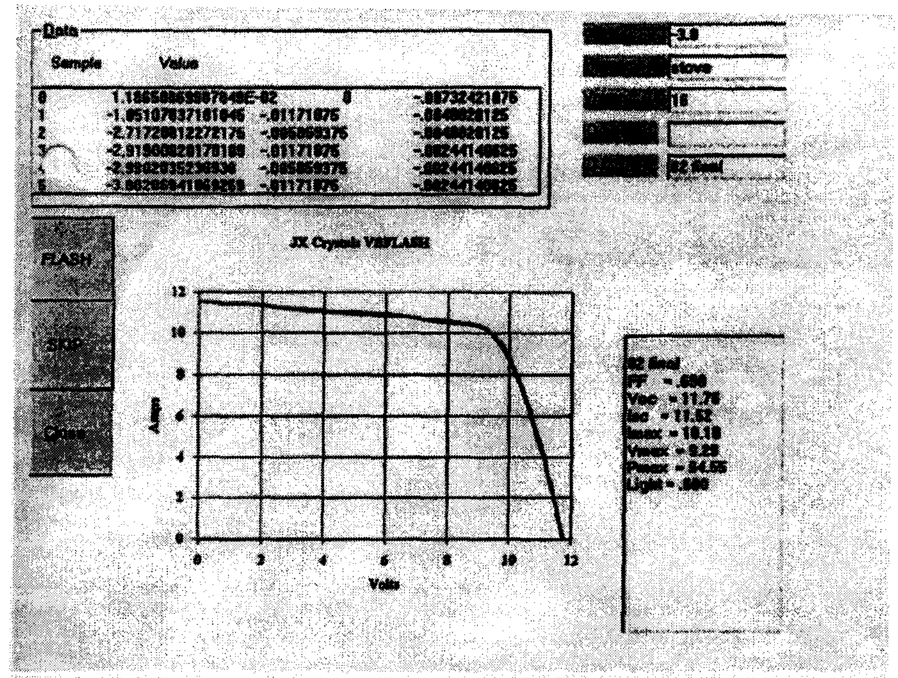

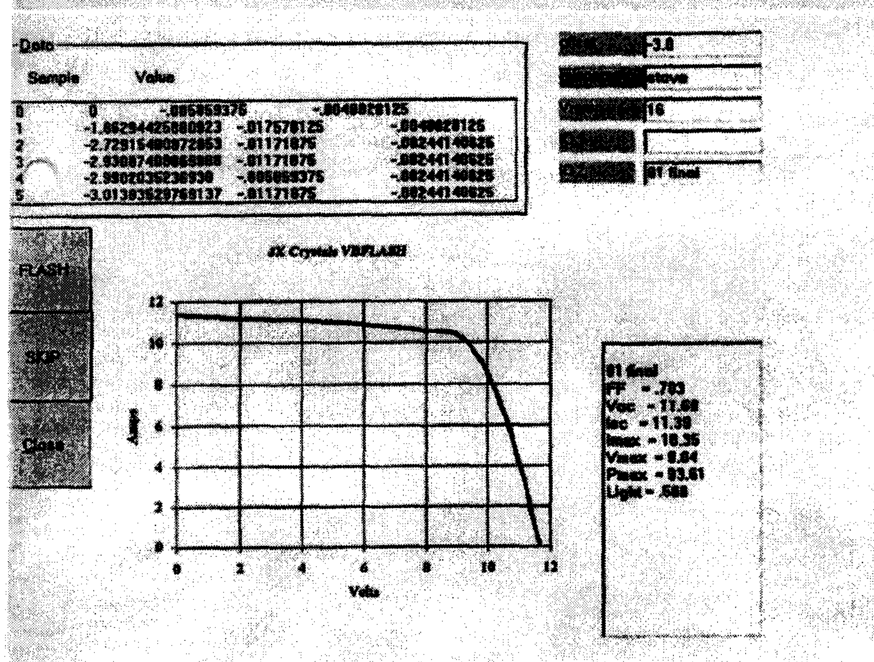

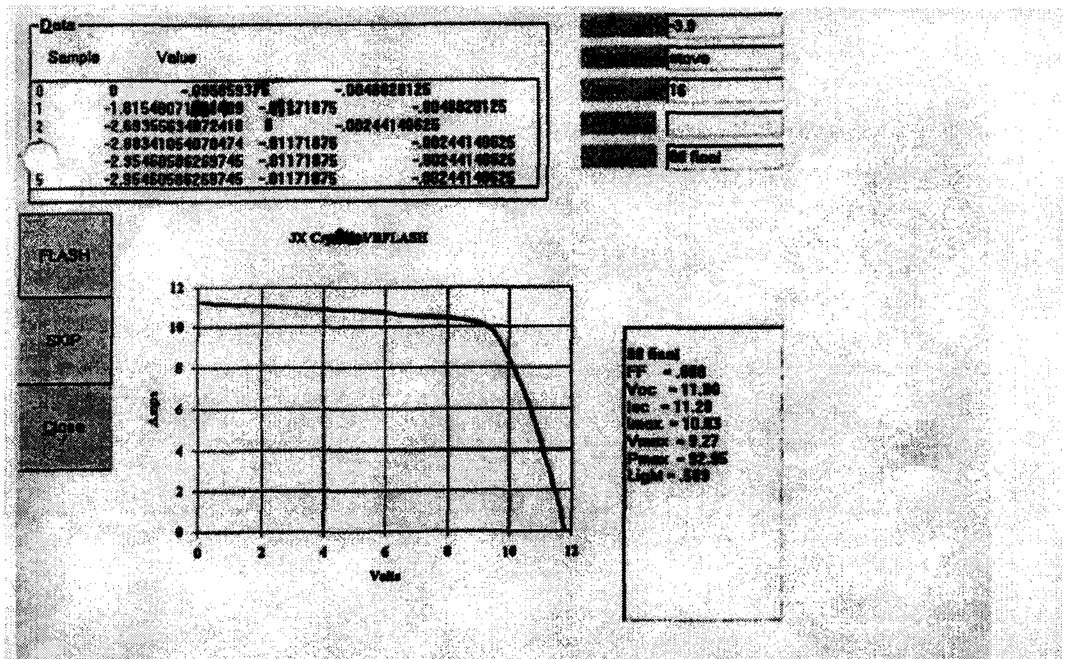
Data
Sample
Value
FLASH
SKIP
Close
Amps
Volts
FF = .808
Voc = 11.90
Isc = 11.29
Vmax = 9.27

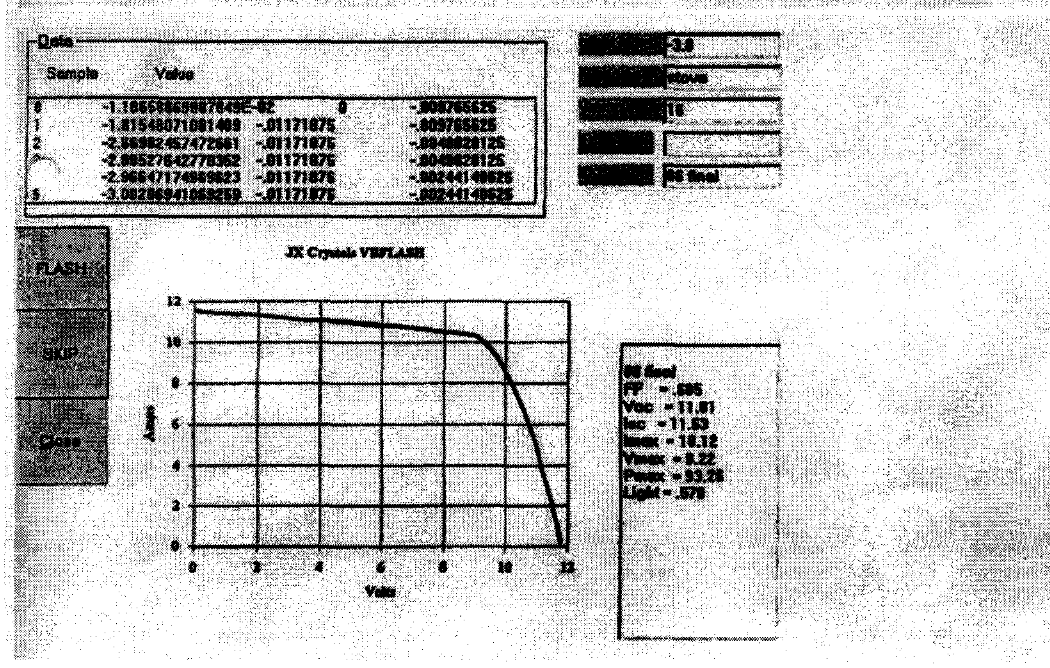
Data
Sample
Value
FLASH
SKIP
Close
JX Crystals VBFLASH
Amps
Volts
FF = .805
Voc = 11.81
Isc = 11.53
Imax = 10.12
Vmax = 9.22
Pmax = 93.28

Appendix E

Gas Chromatograph Output Curves

File : o:\unrefi~1\ezchrom\natgas~1\chris\run2.ezc
Method : c:\ezchrom\methods\butane.met
Acquired : Oct 30, 2003 15:55:35
Printed : Oct 30, 2003 16:08:17
File Desc. : Second sample from chris

→ 6Kw

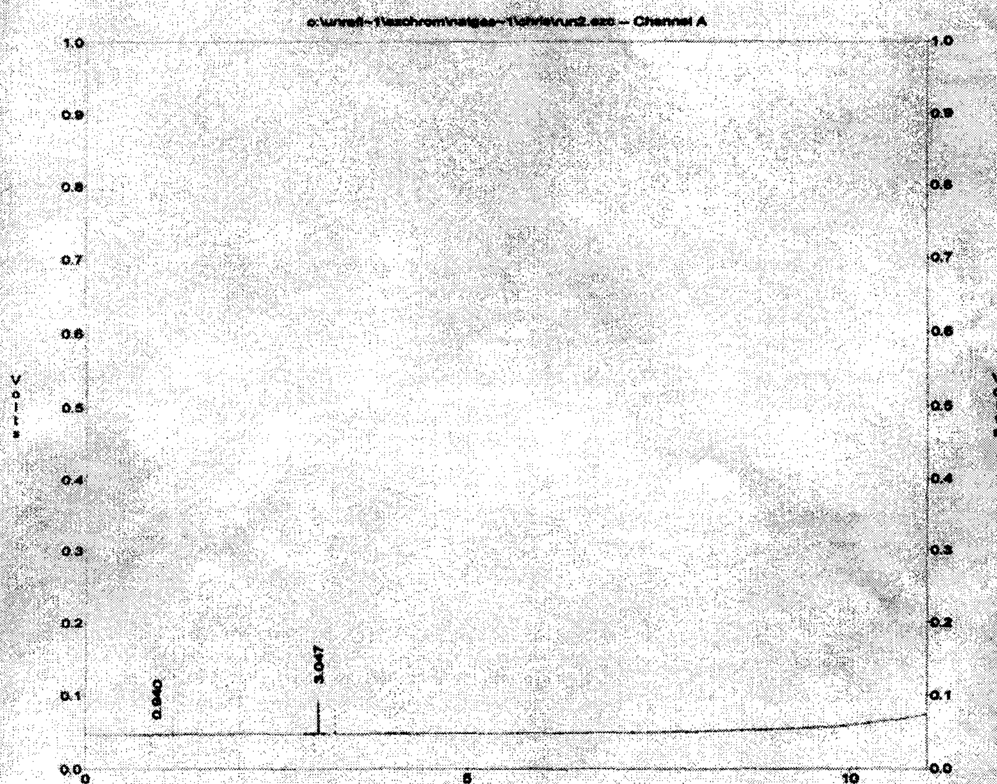

Channel A Results

Peak Numb	Peak Name	RT	Wt %
--	Methane	1.200	0.0
--	Ethane	4.200	0.0
--	Propane	6.000	0.0
--	Butane	8.000	0.0

```
File          : o:\unrefi~1\ezchrom\natgas~1\chris\run7kw.ezc
Method        : c:\ezchrom\methods\butane.met
Acquired      : Oct 30, 2003  16:13:04
Printed       : Oct 30, 2003  16:27:34
File Desc.    : Run #3
                7 KW
```

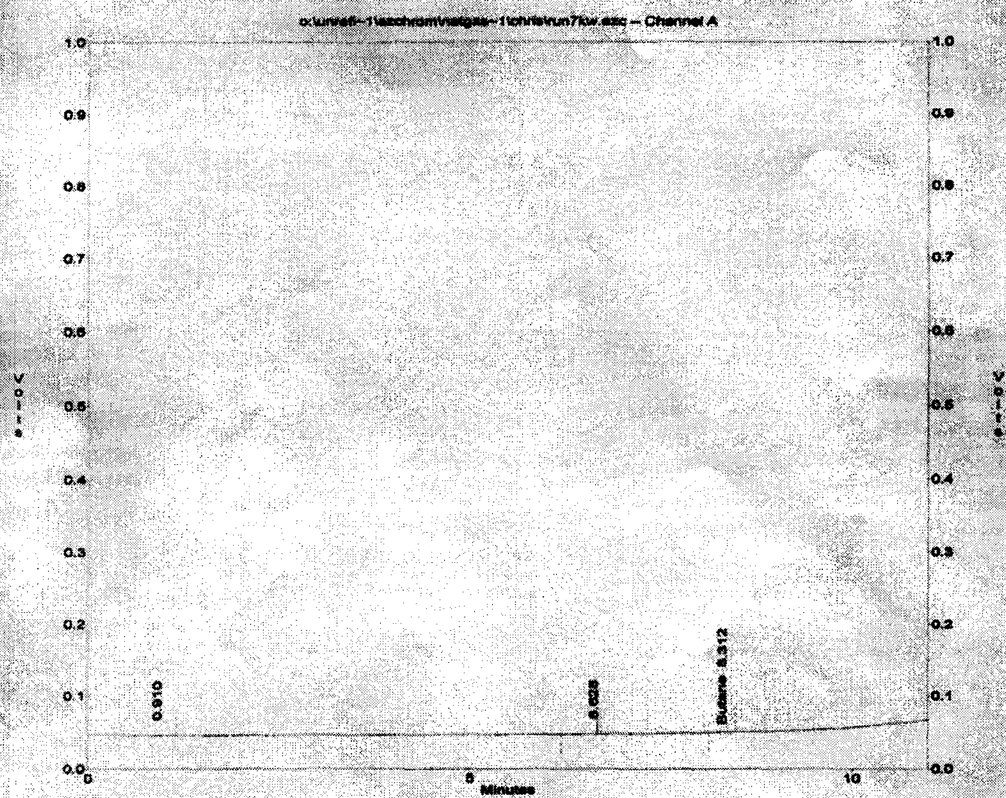

Channel A Results

Peak Numb	Peak Name	RT	Wt %
--	Methane	1.200	0.0
--	Ethane	4.200	0.0
--	Propane	6.000	0.0
3	Butane	8.312	99.0

```
File       : o:\unrefi~1\ezchrom\natgas~1\chris\run1a.ezc
Method     : c:\ezchrom\methods\butane.met
Acquired   : Oct 30, 2003  15:35:48
Printed    : Oct 30, 2003  16:08:33
File Desc. : First Sample from Chris
             Second Injection
```

→9kW

50μl injected

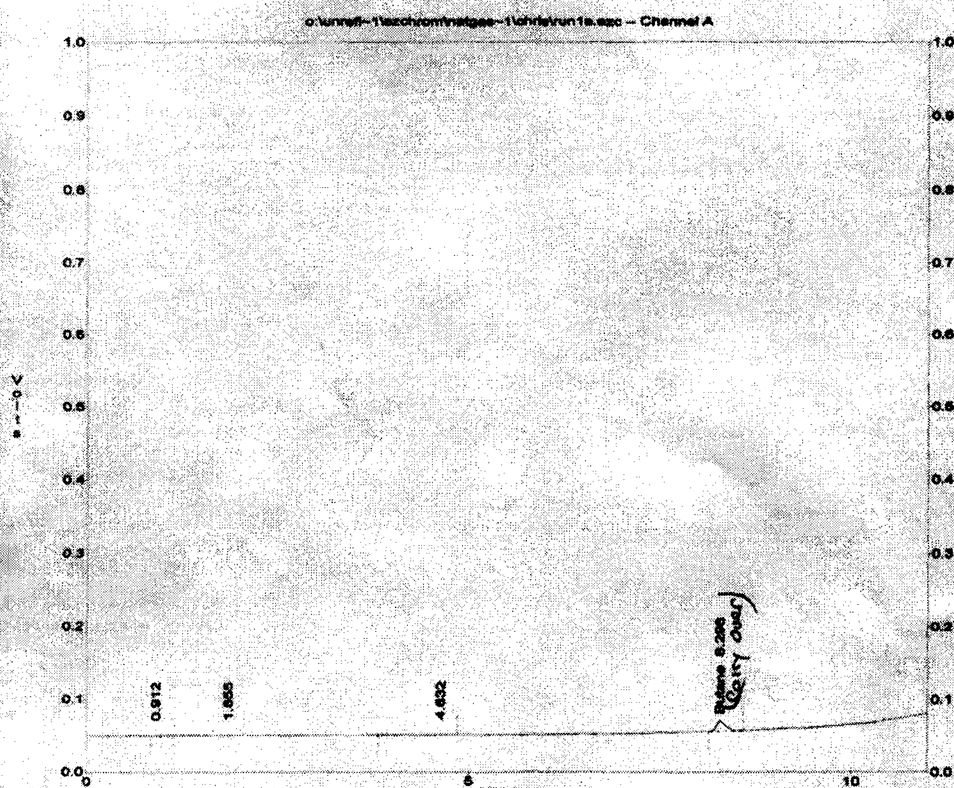

Channel A Results

Peak Numb	Peak Name	RT	Wt %
--	Methane	1.200	0.0
--	Ethane	4.200	0.0
--	Propane	6.000	0.0
4	Butane	8.298	97.8

Appendix F

72-Cell GaSb Circuit Performance Curves

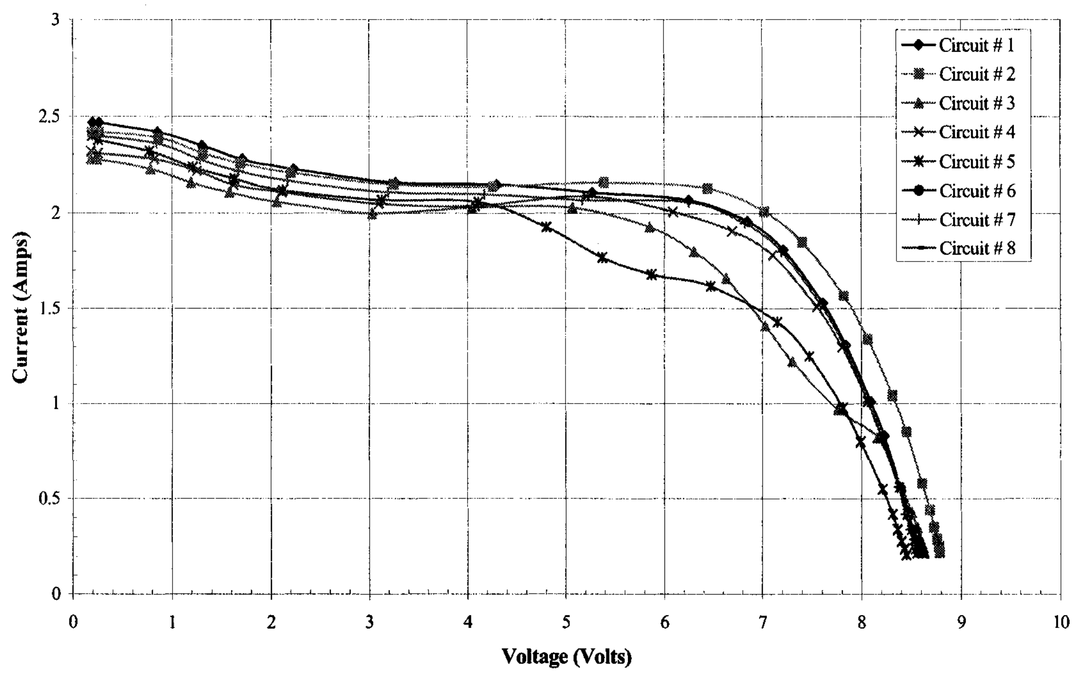

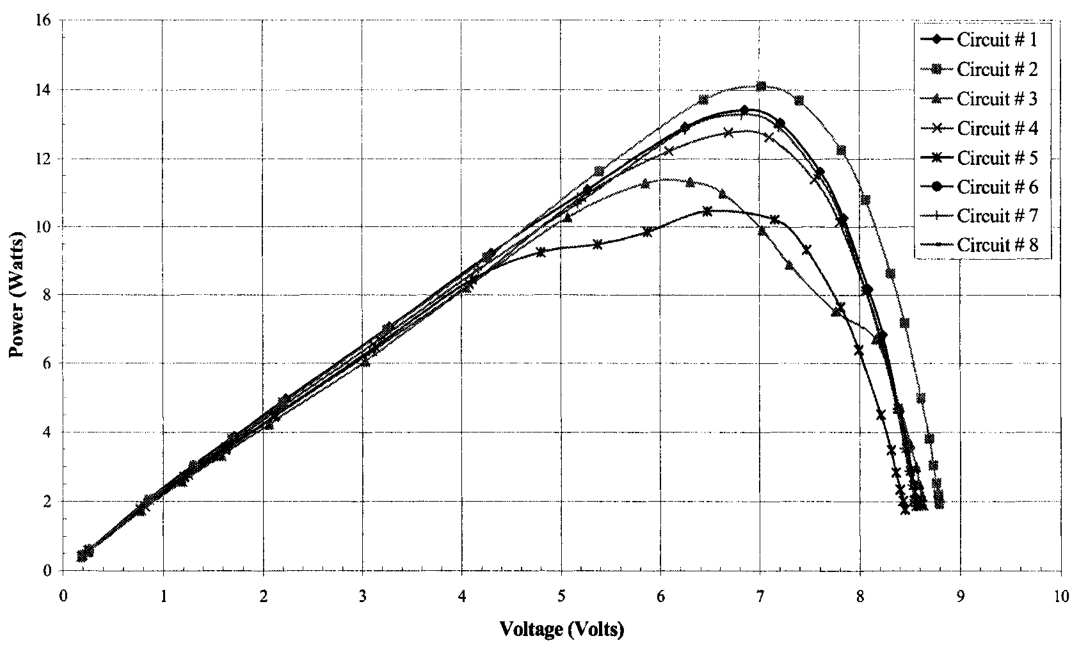

Circuit Performance at a Burner Firing Rate of 7kW

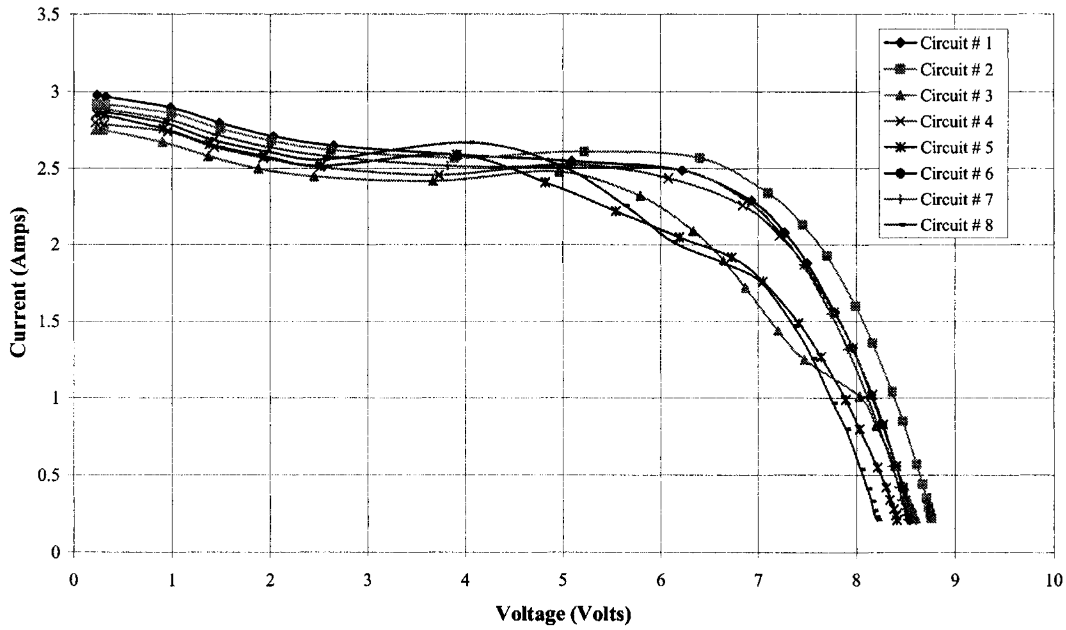

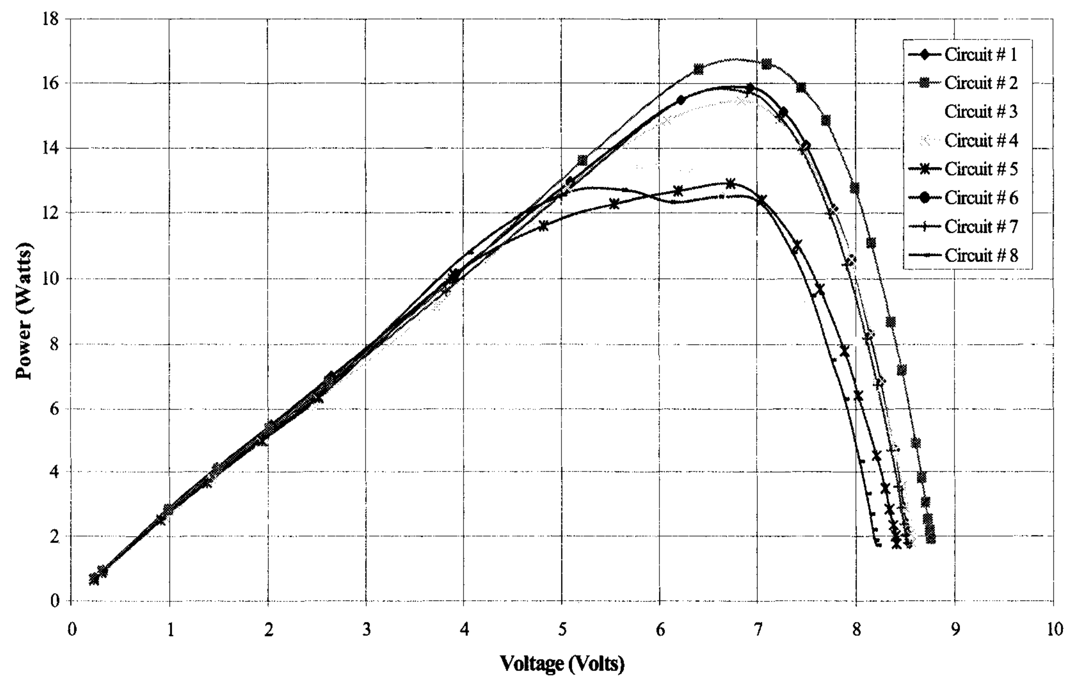

Circuit Performance at a Burner Firing Rate of 8kW

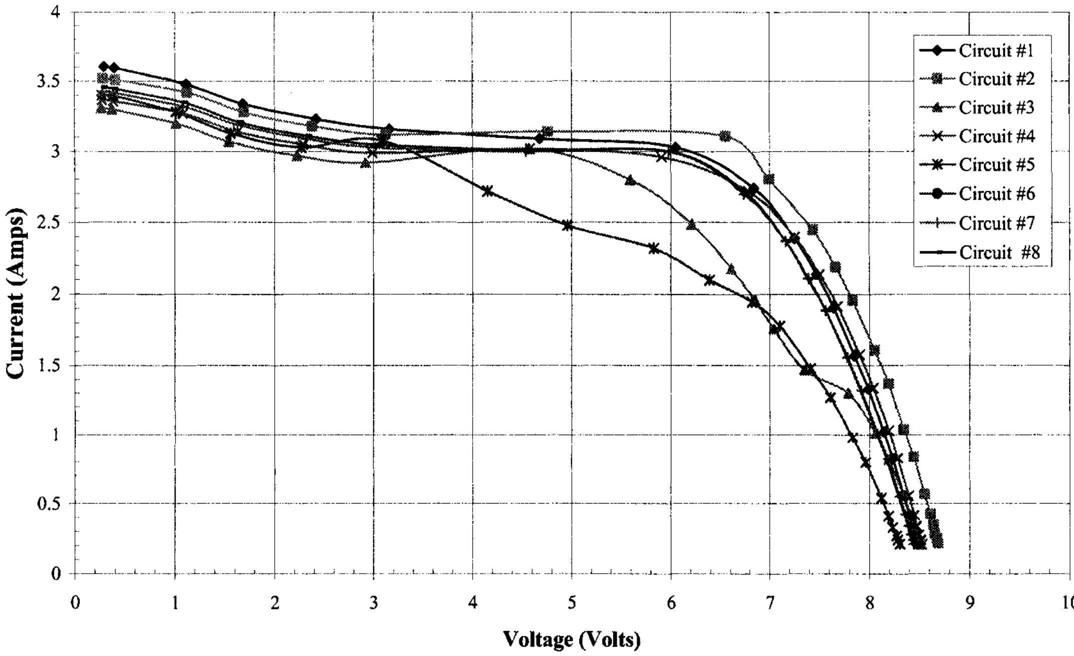

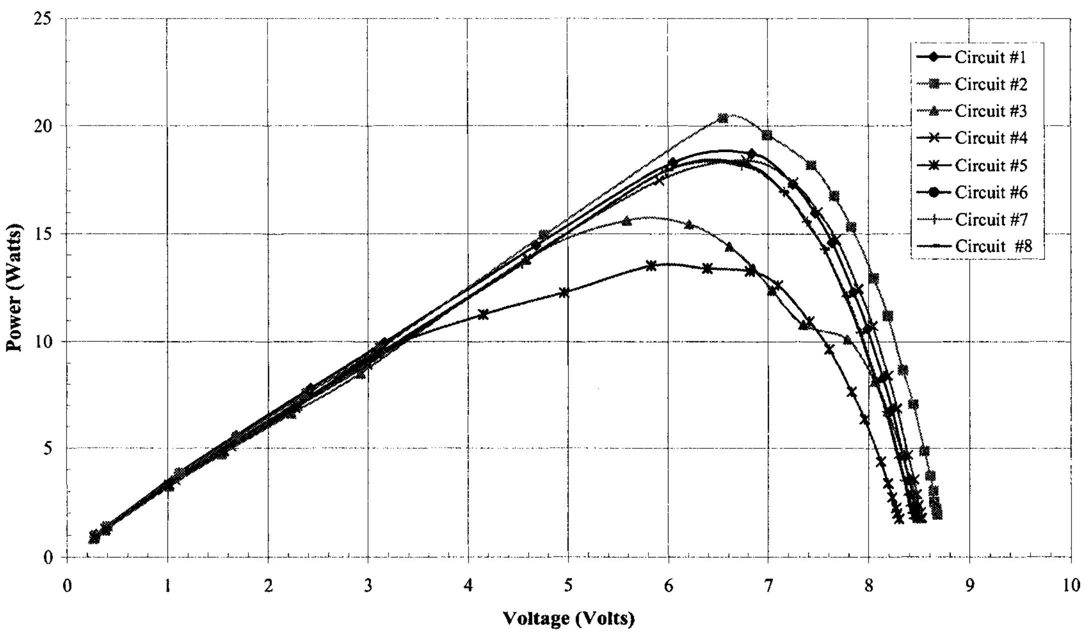

Circuit Performance at a Burner Firing Rate of 9kW

Appendix G

Calculation of Natural Convection Energy Loss

Surface Temperature Measurements

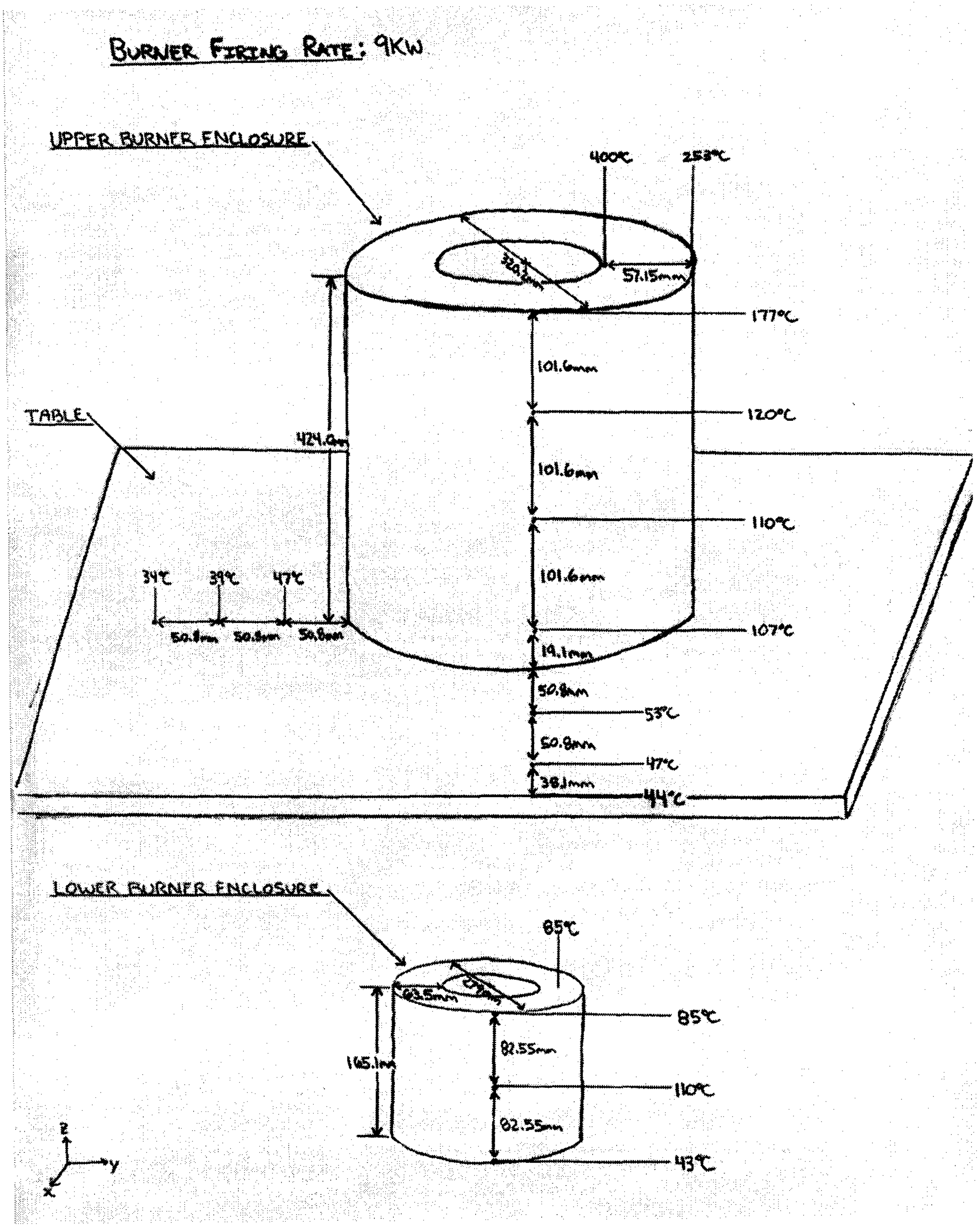

UPPER BURNER ENCLOSURE - HORIZONTAL SURFACE:

Starting with the convection heat transfer rate formula $q = hA\,(T_\infty - T_s)$

Where:

h = convection heat transfer coefficient

A = surface area

T_∞ = surrounding temperature

T_s = surface temperature

The convection heat transfer coefficient (h) for natural convection situations is found via the relationship for Nusselt number:

$$Nu = \frac{hL}{k}$$

for this case:

$$Ra_L + Gr_L \; Pr = \frac{g\beta(T_s - T_\infty)L^3}{\nu^2} \cdot Pr$$

the film temperature (T_f) is used to determine property values:

$$T_f = \frac{T_s + T_\infty}{2}$$

In this case T_s will be taken as the average of the measured values

$$T_s = \frac{400°C + 253°C}{2} = 326.5°C = 599.65K \approx 600K$$

$$\therefore\ T_f = \frac{326.5°C + 25°C}{2} = 175.75°C = 448.9K \approx 450K$$

$\therefore$ for air @ 450K:

$$\beta = \frac{1}{T} \text{ (using ideal gas assumption)}$$

$$\beta = \frac{1}{449}K$$

$$v_{@450K} = 32.39 \times 10^{-6} m^2/s \qquad k = 37.3 \times 10^{-3} w/mk$$

$$Pr_{450K} = 0.686$$

Also, for horizontal plates, the characteristic length L is often defined by:

$$L = \frac{A_s}{P} = \frac{\text{plate surface area}}{\text{perimeter}} = \frac{[\pi(160.1mm)^2 - \pi(102.95mm)^2]}{\pi(320.2mm)}$$

$$L = 46.95mm = 0.4695m$$

$$\therefore Ra_L = \frac{g\beta(T_s - T_\infty)L^3}{v^2} \cdot Pr = \frac{(9.81 m/s^2)(\frac{1}{449K})(600K - 298K)(0.4695m)^3}{(32.39 \times 10^{-6} m^2/s)^2} \cdot 0.686$$

$$Ra_L = 4.465 \times 10^8$$

For a Reynolds number in this range, eqn (9.31), pg 462 Incropera & DeWitt applies:

$$\overline{Nu_L} = 0.15\ Ra_L^{1/3}$$

$$\therefore \overline{Nu_L} = \frac{hL}{k} = 0.15(4.465 \times 10^8)^{1/3}$$

$$\therefore h = \frac{k}{0.4695m} \cdot 0.15(4.465 \times 10^8)^{1/3}$$

$$\therefore h = \frac{37.3 \times 10^{-3}\ W/mK}{0.4695m} \cdot 0.15(2.03 \times 10^9)^{1/3}$$

$$h = 15.08\ W/m^2K$$

$\therefore$ to find the rate of energy loss through the horizontal surface of the upper burner enclosure:

$$q = hA\,(T_s - T_\infty) = (15.08\ W/m^2K)\,[\pi\,(0.1601\ m)^2 - \pi\,(0.10295m)^2]\,(327°C - 25°C)$$

$$\boxed{q = 215W \text{ - horizontal surface of upper burner enclosure}}$$

UPPER BURNER ENCLOSURE - VERTICAL SURFACE

Flat plate correlations can be used in this situation if

$$\frac{D}{L} \geq \frac{35}{Gr_L^{1/4}}$$

where $Gr_L = \dfrac{g\beta(T_s - T_\infty)L^3}{\nu^2}$

where T_s is the average of the measured values

$$T_s = \frac{120°C + 110°C + 107°C}{3} = 112.3°C = 385K$$

L = height of cylinder = 0.424m

Properties for air are evaluated at the film temperature (T_f):

$$T_f = \frac{T_s + T_\infty}{2} = \frac{385k + 298K}{2} = 342K$$

$$\therefore \beta_{air@342K} = \frac{1}{342K}$$

$$v_{air@342K} = 20.12 x 10^{-6} m^2/s$$

$$Gr_L = \frac{(9.81 m/s^2)(\frac{1}{342K})(385 - 298)(0.424m)^3}{(20.12 x 10^{-6} m^2/s)^2}$$

$$\therefore \frac{D}{L} = \frac{0.3202m}{0.424m} = 0.7552 > \frac{35}{(4.699 x 10^8)^{1/4}} = 0.238$$

$\therefore$ Flat plate correlations can be used in this case.

Now, check Rayleigh number to determine if laminar or turbulent flow exists on this surface:

$$Ra = \frac{g\beta(T_s - T_\infty)L^3}{v\alpha} = \frac{(9.81 m/s^2)(\frac{1}{342K})(385 - 298)(0.424 m)^3}{(20.12 x 10^{-6} m^2/s)(28.716 x 10^{-6} m^2/s)}$$

$Ra = 3.29 \times 10^8 < 10^9$ $\therefore$ flow can be assumed to be laminar

$\therefore$ eqn (9.27) Incropera & DeWitt can be used:

$$\overline{Nu_L} = 0.68 + \frac{0.670 Ra_L^{1/4}}{[1 + (0.492/Pr)^{9/16}]^{4/9}} \quad \text{for} Ra_L \leq 10^9$$

$$\therefore \overline{Nu_L} = 0.68 + \frac{(0.670)(3.29 \times 10^8)^{1/4}}{\left[1 + \left(\frac{0.492}{0.701}\right)^{9/16}\right]^{4/9}} = 47.036$$

$$\therefore \bar{h} = \frac{k}{L}\overline{Nu_L} = \frac{28.716 \times 10^{-3} W/mK}{0.424m} \cdot 47.036$$

$$\bar{h} = 3.19 W/m^2K$$

$$\therefore q = (3.19 W/m^2K)(\pi)(0.3202m)(0.424m)(385K - 298K)$$

q = 118W - vertical surface of upper burner enclosure

TABLE - HORIZONTAL SURFACE

All measured valves are averaged to give: $T_s = 44°C = 317K$.

The area considered will be an annulus of outer radius = 312.5mm and inner radius = 160.1mm

$\therefore A_s = \pi(0.3125m)^2 \cdot \pi(0.1601m)^2$

$A_s = 0.2263m^2$

Similar to the previous horizontal analysis:

$$Ra_L = \frac{g\beta(T_s - T_\infty)L^3}{\nu^2} \cdot Pr$$

Properties are evaluated of the film temperature

$$T_f = \frac{T_s + T_\infty}{2} = \frac{44°C + 25°C}{2} = 34.5°C = 308K$$

$$\nu_{air@300k} = 16.69 \times 10^{-6} m^2/s$$

$$Pr_{air@300k} = 0.706$$

$$L = \frac{A_s}{P} = \frac{0.2263 m^2}{\pi(2)(0.3125 m)} = 0.1153 m$$

$$\therefore Ra_L = \frac{(9.81 m/s^2)\left(\frac{1}{308K}\right)(317K - 298K)(0.1153)^3}{(16.69 \times 10^{-6} m^2/s)^2} \cdot 0.706$$

$$Ra_L = 2.35 \times 10^6$$

∴ using eqn (9.30) from Incropera and DeWitt:

$$\overline{Nu_L} = 0.54\ Ra_L^{1/4}$$

$$\therefore \overline{Nu_L} = 0.54(2.35 \times 10^6)^{1/4}$$

$$\overline{Nu_L} = 21.14$$

$$\text{now, } \bar{h} = \frac{k}{L}\overline{Nu_L}$$

$$\bar{h} = \frac{26.89 \times 10^{-3} W/mK}{0.1153 m} \cdot 21.14 = 4.93 W/m^2K$$

$\therefore q = hA(T_s - T_\infty) = (4.93\ W/m^2K)(0.2263 m^2)(317K - 298K)$

$\boxed{q = 21W \text{ - horizontal table surface}}$

LOWER BURNER ENCLOSURE - HORIZONTAL SURFACE

- measured T_s value = 85°C = 358K.

- annulus with outer radius = 0.1395m
  - inner radius = 0.076m

$$- \text{ area } A_s = \pi(0.1395\text{m})^2 - \pi(0.076\text{m})^2$$

$$A_s = 4.3\text{x}10^{-2}\text{m}^2$$

$$- L = \frac{A_s}{P} = \frac{4.3\text{x}10^{-2}\text{m}^2}{\pi(0.279\text{m})} = 4.905\text{x}10^{-2}\text{m}$$

$$\therefore Ra_L = \frac{g\beta(T_s - T_\infty)L^3}{\nu^2} \cdot Pr$$

$$\text{with } T_f = \frac{358\text{K} + 298\text{K}}{2} = 328\text{K}$$

$$\therefore \nu_{air328k} = 18.71\text{x}10^{-6}\text{m}^2/\text{s}$$

$$\beta_{air@328k} = \frac{1}{328\text{K}}$$

$$Pr_{air@328k} = 0.703$$

$$Ra_L = \frac{(9.81\text{m/s}^2)\left(\frac{1}{328\text{K}}\right)(358\text{K} - 298\text{K})(4.905\text{x}10^{-2}\text{m})^3}{(18.71\text{x}10^{-6}\text{m}^2/\text{s})^2} \cdot 0.703$$

$$Ra_L = 4.25\text{x}10^5$$

∴ using eqn (9.30) from Incropera & DeWitt:

$$\overline{Nu_L} = 0.54\ Ra_L^{1/4} = 0.54(4.25\times10^5)^{1/4} = 13.79$$

$$\therefore \bar{h} = \frac{k}{L}\cdot\overline{Nu_L}$$

$$\bar{h} = \frac{28.372\times10^{-3}\,\text{W/mK}}{4.905\times10^{-2}}\cdot 13.79$$

$$\bar{h} = 7.98\,\text{W/m}^2\text{K}$$

$\therefore q = hA_s(T_s - T_\infty) = (7.98\ \text{W/m}^2\text{K})(4.30 \times 10^{-2}\text{m}^2)(358\text{K} - 298\text{K})$

$\boxed{q = 21\text{W} \text{ - horizontal surface, lower burner enclosure.}}$

LOWER BURNER ENCLOSURE - VERTICAL SURFACE

Check if flat plate formulas can be employed

i.e. does $\frac{D}{L} \geq \frac{35}{Gr_L^{1/4}}$ apply?

$$Gr_L = \frac{g\beta(T_s - T_\infty)L^3}{\nu^2}$$

T_s = average of measured valves = 79°C ≈352K ≈ 350K

L = height of cylinder = 0.165m

$$T_f = \frac{T_s + T_\infty}{2} = \frac{350 + 298\text{K}}{2} = 324\text{K}.$$

$$\nu_{air@324K} = 18.30\text{x}10^{-6}\,m^2/s$$

$$\beta_{air@324K} = \frac{1}{324K}$$

$$\therefore\ Gr_L = \frac{(981\,m/s^2)\left(\frac{1}{324K}\right)(350K - 298K)(0.165m)^3}{(18.30\text{x}10^{-6}\,m^2/s)^2}$$

$$Gr_L = 2.112\text{x}10^7$$

now

$$\frac{D}{L} = \frac{0.279m}{0.1651\,m} = 1.69 > \frac{35}{Gr_L^{1/4}} = \frac{35}{(2.11\text{x}10^7)^{1/4}} = 0.516$$

$\therefore$ flat plate formulas applied

$$\text{now,}\ Ra_L = \frac{g\beta(T_s - T_\infty)L^3}{\nu\alpha} = \frac{(9.31m/s^2)\left(\frac{1}{324K}\right)(350K - 298K)(0.1651m)^3}{(18.3\text{x}10^{-6}m^2/s)(26.05\text{x}10^{-6}m^2/s)}$$

$Ra_L = 1.49 \text{ x } 10^7 < 10^9$ $\therefore$ not turbulent

$\therefore$ Eqn (9.27) Incropera & DeWitt is used

$$\overline{Nu_L} = 0.68 = \frac{0.670\,Ra_L^{1/4}}{[1 + (0.492/Pr)^{9/16}]^{4/9}} = 0.68 + \frac{(0.670)(1.49 \times 10^7)^{1/4}}{\left[1 + \left(\frac{0.492}{0.703}\right)^{9/16}\right]^{4/9}}$$

$$\overline{Nu_L} = 32.57$$

$$\therefore \bar{h} = \frac{k}{L}\overline{Nu_L} = \frac{28.076 \times 10^{-7} W/mk}{(0.1651m)} \cdot 32.57$$

$$\bar{h} = 5.54 W/m^2k$$

$q = hA_s (T_s - T_\infty) = (5.54\ W/mk)\ (\pi)\ (0.279m)\ (350K - 298K)$

$\boxed{q = 253W}$ - LOWER BURNER ENCLOSURE, VERTICAL PIECE

<u>TOTAL CALCULATED LOSS DUE TO NATURAL CONVECTION @ 9KW FIRING RATE:</u>

$$q_{TOTAL} = q_{UPPER\ HORIZONTAL} + q_{UPPER\ VERTICAL} + q_{TABLE} + q_{LOWER\ HORIZONTAL} + q_{LOWER\ VERTICAL}$$
$$q_{TOTAL} = 215W + 118W + 21W + 21W + 253W$$

$$\boxed{q_{TOTAL} = 628W}$$